



Calhoun: The NPS Institutional Archive
DSpace Repository

Theses and Dissertations

1. Thesis and Dissertation Collection, all items

2002-09

A comparative analysis of radiation effects on silicon, gallium arsenide, and GaInP₂/GaAs/Ge triple junction solar cells using a 30 MeV electron linear accelerator

Woods, Michael D.

Monterey California. Naval Postgraduate School

<http://hdl.handle.net/10945/2894>

Downloaded from NPS Archive: Calhoun



Calhoun is a project of the Dudley Knox Library at NPS, furthering the precepts and goals of open government and government transparency. All information contained herein has been approved for release by the NPS Public Affairs Officer.

Dudley Knox Library / Naval Postgraduate School
411 Dyer Road / 1 University Circle
Monterey, California USA 93943

<http://www.nps.edu/library>

NAVAL POSTGRADUATE SCHOOL
Monterey, California



THESIS

**A COMPARATIVE ANALYSIS OF RADIATION EFFECTS
ON SILICON, GALLIUM ARSENIDE, AND TRIPLE
JUNCTION SOLAR CELLS USING A 30 MeV ELECTRON
LINEAR ACCELERATOR**

by

Michael D. Woods
September 2002

Thesis Advisor:
Second Reader:

Sherif Michael
Ron J. Pieper

Approved for public release; distribution is unlimited.

THIS PAGE INTENTIONALLY LEFT BLANK

REPORT DOCUMENTATION PAGE			Form Approved OMB No. 0704-0188
Public reporting burden for this collection of information is estimated to average 1 hour per response, including the time for reviewing instruction, searching existing data sources, gathering and maintaining the data needed, and completing and reviewing the collection of information. Send comments regarding this burden estimate or any other aspect of this collection of information, including suggestions for reducing this burden, to Washington headquarters Services, Directorate for Information Operations and Reports, 1215 Jefferson Davis Highway, Suite 1204, Arlington, VA 22202-4302, and to the Office of Management and Budget, Paperwork Reduction Project (0704-0188) Washington DC 20503.			
1. AGENCY USE ONLY (Leave blank)	2. REPORT DATE September 2002	3. REPORT TYPE AND DATES COVERED Master's Thesis	
4. TITLE AND SUBTITLE: A comparative analysis of radiation effects on Silicon, Gallium Arsenide and GaInP ₂ /GaAs/Ge Triple Junction Solar Cells Using a 30 MeV electron Linear Accelerator			5. FUNDING NUMBERS
6. AUTHOR(S) Woods, Michael D.			
7. PERFORMING ORGANIZATION NAME(S) AND ADDRESS(ES) Naval Postgraduate School Monterey, CA 93943-5000			8. PERFORMING ORGANIZATION REPORT NUMBER
9. SPONSORING /MONITORING AGENCY NAME(S) AND ADDRESS(ES) N/A			10. SPONSORING/MONITORING AGENCY REPORT NUMBER
11. SUPPLEMENTARY NOTES The views expressed in this thesis are those of the author and do not reflect the official policy or position of the Department of Defense or the U.S. Government.			
12a. DISTRIBUTION / AVAILABILITY STATEMENT Approved for public release; distribution is unlimited			12b. DISTRIBUTION CODE
13. ABSTRACT (maximum 200 words) Many improvements have been made in the design and manufacture of high efficiency solar cells. The need to understand the behavior of these new types of solar cells is crucial to the procurement of future space systems, both commercial and military. This thesis studies the results of irradiating three commonly used solar cells with 30 MeV electrons using the Naval Postgraduate School Linear Accelerator. A comparison of the performance characteristics of the three cells is made using commonly accepted parameters and notes the differences in failure mode. Additionally, the affect of current annealing is investigated.			
14. SUBJECT TERMS Solar cells, triple junction, multi junction, GaAs, Si, GaInP ₂ /GaAs/Ge			15. NUMBER OF PAGES 109
			16. PRICE CODE
17. SECURITY CLASSIFICATION OF REPORT Unclassified	18. SECURITY CLASSIFICATION OF THIS PAGE Unclassified	19. SECURITY CLASSIFICATION OF ABSTRACT Unclassified	20. LIMITATION OF ABSTRACT UL

THIS PAGE INTENTIONALLY LEFT BLANK

Approved for public release; distribution is unlimited

**A COMPARATIVE ANALYSIS OF RADIATION EFFECTS ON SILICON,
GALLIUM ARSENIDE AND GaInP₂/GaAs/Ge TRIPLE JUNCTION SOLAR
CELLS USING A 30 MeV ELECTRON LINEAR ACCELERATOR.**

Michael D. Woods
Lieutenant, United States Navy
B.S. University of Washington, 1996

Submitted in partial fulfillment of the
requirements for the degree of

MASTER OF SCIENCE IN SPACE SYSTEMS OPERATIONS

from the

**NAVAL POSTGRADUATE SCHOOL
September 2002**

Author:

Michael D. Woods

Approved by:

Sherif Michael
Thesis Advisor

Ron J. Pieper
Second Reader

Rudy Panholzer
Chairman, Space Systems Academic Group

THIS PAGE INTENTIONALLY LEFT BLANK

ABSTRACT

Many improvements have been made in the design and manufacture of high efficiency solar cells. The need to understand the behavior of these new types of solar cells is crucial to the procurement of future space systems, both commercial and military. This thesis studies the results of irradiating three commonly used solar cells with 30 MeV electrons using the Naval Postgraduate School Linear Accelerator. A comparison of the performance characteristics of the three cells is made using commonly accepted parameters and notes the differences in trends and failure modes. Additionally, the affect of current annealing is investigated.

THIS PAGE INTENTIONALLY LEFT BLANK

TABLE OF CONTENTS

I.	INTRODUCTION.....	1
II.	SPACE RADIATION AND ITS EFFECTS	5
	A. INTRODUCTION.....	5
	B. TYPES AND SOURCES OF RADIATION.....	5
	1. Cosmic Rays.....	6
	2. The Solar Plasma and the Solar Wind	6
	3. Van Allen Belts	7
	1. Wave (Photon) Effects	10
	<i>a. Photoelectric Effect.....</i>	<i>10</i>
	<i>b. Compton's Scattering.....</i>	<i>11</i>
	<i>c. Pair Production</i>	<i>12</i>
	2. Charged Particle effects:	13
	<i>a. Inelastic Collisions with Bound Atomic Electrons</i>	<i>13</i>
	<i>b. Elastic Collisions with Atomic Nuclei</i>	<i>13</i>
	<i>c. Inelastic Collisions with Atomic Nuclei</i>	<i>14</i>
	D. DAMAGE MECHANISMS.....	14
	1. Ionization.....	14
	2. Atomic displacement	15
III.	SEMICONDUCTOR THEORY	17
	A. PROPERTIES	17
	B. INTRINSIC AND EXTRINSIC MATERIAL.....	18
	C. BAND GAP ENERGY	20
	D. CARRIER TRANSPORT.....	22
	E. THE P-N JUNCTION.....	23
	1. Creation of the P-N Junction.....	23
	2. P-N junction behavior	24
	3. Charge Carrier Lifetime.....	28
IV.	SOLAR CELLS.....	31
	A. SOLAR ENERGY	31
	B. BASIC OPERATION	32
	C. PARAMETERS.....	34
	D. RADIATION EFFECTS ON OUTPUT PARAMETERS.....	36
	1. Open Circuit Voltage V_{oc}.....	36
	2. Short Circuit Current I_{sc}	36
	3. Maximum Power P_{max}.....	37
	E. MULTI-JUNCTION CELLS.....	37
	F. ANATOMY OF A MULTI JUNCTION SOLAR CELL	40
V.	THE NAVAL POSTGRADUATE SCHOOL LINEAR ACCELERATOR	43
	A. BASIC OPERATION	43
	B. BEAM FORMATION AND TRANSMISSION.....	44

C.	BEAM STEERING AND FOCUSING	45
D.	BEAM FLUENCE MEASUREMENT.....	47
E.	CALIBRATION PROCEDURE.....	48
VI.	EXPERIMENT.....	51
A.	INTRODUCTION.....	51
B.	RADIOLOGICAL SAFETY.....	51
C.	SOLAR SIMULATOR AND TEST EQUIPMENT.....	52
D.	PROCEDURE.....	56
E.	TEST RESULTS	58
VII.	CONCLUSIONS.....	61
	LIST OF REFERECES	69
	APPENDIX A	73
	INITIAL DISTRIBUTION LIST	93

LIST OF FIGURES

Figure 1.	The Solar Wind [From: Ref. 1 pg. 5.1].....	6
Figure 2.	The Magnetosphere [From: Ref. 1 pg. 5.5].....	7
Figure 3.	Trapped particles reflecting between two mirror points.	
	[From: Ref. 2 pg. 100].....	8
Figure 4.	The McIlwain Coordinate System. [From: Ref. 1 pg. 5.5]	9
Figure 5.	Charged particle distribution in the Magnetosphere.	
	[From: Ref. 26 pg. 20].....	10
Figure 6.	Photoelectric Effect. [From: Ref. 5 pg. 66].....	11
Figure 7.	Compton's Scattering [From: Ref. 4 pg. 116]	12
Figure 8.	Rutherford Scattering [From: Ref. 25 pg. 139].....	14
Figure 9.	Frenkel Pairs [From: Ref. 27 pg. 181]	16
Figure 10.	Diamond and Zincblende structure. [From: Ref. 10 pg. 10].....	18
Figure 11.	Intrinsic and extrinsic crystal structure [From: Ref: 3 pg. 8].....	20
Figure 12.	Energy band diagrams for intrinsic, n-type and p-type material.	
	[From: Ref. 29 pg. 10].....	22
Figure 13.	The p-n junction. [From: Ref. 3 pg. 14].....	24
Figure 14.	The p-n junction under reverse bias conditions.	
	[From Ref. 3 pg. 15].....	25
Figure 15.	The p-n junction in the breakdown region. [From: Ref. 3 pg. 16].....	25
Figure 16.	The p-n junction under forward bias conditions.	
	[From: Ref. 3 pg. 17].....	27
Figure 17.	Diode characteristic curve. [From: Ref. 16 pg. 33].....	27
Figure 18.	The capture process of an electron-hole pair at a radiation induced	
	recombination energy level. [From: Ref. 16 pg. 21].....	30
Figure 19.	Spectral Irradiance and 5800K Blackbody curves.	
	[From: Ref. 18 pg. 10].....	32
Figure 20.	The basic solar cell. [From: Ref. 3 pg. 15a].....	33
Figure 21.	Plot of carrier concentration versus cell depth for an	
	illuminated cell. [From: Ref. 1 pg. 1.2].....	34
Figure 22.	I-V curve with performance parameters. [From: Ref. 18 pg. 11]	35
Figure 23.	Notional depiction of multi-junction spectral utility.....	
	[After: Ref. 27 pg. 37].....	38
Figure 24.	Tunnel junction I-V curve (left) and the current components that make up	
	the I-V curve (right). [From: Ref. 16. pg. 53].....	40
Figure 25.	Cross-section of a triple junction cell. [From: ref 16 pg. 64].....	42
Figure 26.	The Naval Postgraduate School LINAC [From: Ref. 27 pg. 15].....	44
Figure 27.	Beam injection system and pre-buncher assembly.	
	[From Ref. 27 pg. 18].....	45
Figure 28.	Deflection system. [From: Ref. 26 pg. 21].....	46
Figure 29.	Quadrupole Magnets	46
Figure 30.	Secondary Emission Monitor and Cell Target Stand.....	47
Figure 31.	30 MeV Faraday Cup	48

Figure 32.	Beam path from SEM to the Faraday Cup.	49
Figure 33.	Top view of beam path. SEM at top, Faraday Cup at bottom.	50
Figure 34.	SS-1000 Solar simulator in operation.	52
Figure 35.	X-Y-Z focal plane adjustment settings on the SS-1000 solar simulator.	53
Figure 36.	Test block showing electrical contacts, cooling connections and thermocouple attachment.	55
Figure 37.	Capture of LABVIEW program used to obtain the I-V curves.	56
Figure 38.	Cell efficiency plot versus 30 MeV electron fluence for all three test cells.	61
Figure 39.	Short circuit current (Isc) plot versus 30 MeV electron fluence for all three test cells.	63
Figure 40.	Open circuit voltage (Voc) plot versus 30 MeV electron fluence for all three test cells.	64
Figure 41.	Composite diagrams of Pmax, Vmax and Imax for all three test cells.	65
Figure 42.	Current Performance Ratios of cell Si02.	67

LIST OF TABLES

Table 1.	Energy levels associated with the wave effects.	13
Table 2.	Effect of diode voltage on breakdown mechanism.	26
Table 3.	Lattice and Bandgap properties of the Spectrolab Triple-Junction cell materials	40
Table 4.	BOL data for test cells.....	57
Table 5.	Target Fluence / Voltage conversion.	57

THIS PAGE INTENTIONALLY LEFT BLANK

ACKNOWLEDGEMENTS

The completion of this thesis marks a significant milestone in my career. However, the success of such an event does not come about without the support of many key people. I thank my wonderful family for their support throughout my time here. I recognize that they too had to sacrifice many hours without Dad around for me to be able to accomplish my goal.

I would also like to thank Don Snyder and Steven Richards. They sacrificed valuable time and worked late into the night in order for me to complete the work using the Linear Accelerator. I greatly appreciate their monumental efforts.

Lastly, I would like to thank my advisor, Professor Sherif Michael. His guidance and patience were instrumental in this endeavor.

THIS PAGE INTENTIONALLY LEFT BLANK

I. INTRODUCTION

Today, the demand for space enabled products and services are greater than ever. Advances in technology have spurred major improvements in spacecraft capability since the days of Sputnik and Vanguard. This in turn has spurred the need to provide more power to feed the ever-growing requirements of today's satellites.

Bell labs first introduced photovoltaic (PV) devices in the 1950's. PV devices enable spacecraft to operate for extended periods by harnessing light energy and turning it into electrical power for the spacecraft. However, although the light energy is essentially free, the cost of conversion is high. Early PV devices had efficiency levels on the order of one to two percent. Even good silicon cells in the 1960's were only 10% efficient. As spacecraft power requirements rose through the years, solar cell designers have had to investigate ways to improve the efficiency of PV devices.

One of the problems facing PV device designers was the damage to the cells due to various forms of radiation exposure while on orbit. A good silicon cell design could yield roughly 15% efficiency, but after a few years (depending on the orbit), the efficiency could drop to as little as 8-10%. The need to understand the radiation environment and it's effect on the materials used in PV devices was crucial if power was not to be the limiting factor of space based capabilities.

Silicon solar cells were the dominant PV device until the 1980's when GaAs arrived on the scene. The properties of GaAs make it inherently radiation hardened (compared to Silicon), and the electrical characteristics promote better power conversion (approximately 17%). However, as good an advancement in design as GaAs was, it was obvious that further advancements would be needed in order to meet not only the power requirements, but the size, weight, and mission duration requirements of future space missions.

Recent PV designs take advantage of the fact that different materials with different bandgap energies can harness more of the Sun's energy spectrum and thus increase efficiency. These PV devices, called multi-junction cells, essentially stack material in decreasing order of bandgap energy, absorbing high frequency light in the top layers and allowing lower frequencies to filter below to be utilized by the next material. This has led to cell efficiencies as high as 30% in some applications.

Notable increases in the performance of multi-junction cells have come about by raising the number of effective layers and using more efficient material. One such cell is the Spectrolab GaInP₂/GaAs/Ge solar cell. Improvements in cell technology allow this PV device to boast an impressive 24% efficiency. Cells such as these are paving the way to lighter weight solar panels because the cells themselves have become thinner. Additionally, the higher efficiency means fewer cells are required to create the same amount of power.

There has been extensive research over the years on the effects of radiation on solar cells. However, as cell technology advances to keep up with the rapidly increasing power requirements, less is becoming known about the actual failure modes and damage mechanisms affecting solar cells currently being used.

This study provides the reader a comparative analysis of the effects of radiation on three different types of solar cells. Silicon and Gallium Arsenide are well established and much is known about them as "common knowledge" in the space industry. They provide familiarity and a well-established behavior, which is useful in comparing the behavior of the multi-junction cell to.

Additional research time is devoted to investigating the potential benefit of current annealing in these cells. This is accomplished by the measuring the I-V curves of the irradiated cells multiple times at each fluence level. This will allow a measurement of

the I-V curve after exposure to radiation followed by the annealing effect due to the short circuit current.

Chapter II of this thesis provides a background of the space radiation environment. A discussion of semi-conductor physics is provided in Chapter III. Chapter IV contains a discussion of basic solar cells. The radiation source used in this experiment, the Naval Postgraduate School LINAC, is discussed in chapter V. Chapter VI describes the experiment, including the procedure and the equipment. Finally, Chapter VII discusses the conclusions and recommendations.

THIS PAGE INTENTIONALLY LEFT BLANK

II. SPACE RADIATION AND ITS EFFECTS

A. INTRODUCTION

The space radiation environment is harsh and diverse. Its effects vary depending on parameters such as altitude and solar cycle. An understanding of the environment and its effects is essential to maximizing the lifetime of the spacecraft, more specifically the solar arrays.

There are many types of radiation having varying effects on spacecraft. Of these, there are two general categories of radiation: particles and electromagnetic waves (or photons). An understanding of the interactions and damage mechanisms of the various types is crucial to the design of spacecraft with long mission duration requirements.

The photon is used to describe the particle characteristics of an electromagnetic wave. They exist in discrete quanta of energy given by the equation $e = hv$, where e is the energy of the photon, h is Planck's constant and v is the frequency. High energy photons, such as gamma rays and x-rays are of a particular concern because of their interactions with materials used in solar cell fabrication.

Charged particles such as protons, electrons, alpha and beta particles, and other heavy ions are also a concern in space. These particles can interact kinetically and electro-statically with materials causing defects, which damage and degrade solar arrays.

B. TYPES AND SOURCES OF RADIATION

The radiation found in space can be categorized into three general types: Cosmic Rays, Solar Plasma, and radiation trapped in the earth's geo-magnetic field (also known as the Van-Allen belts). Depending on the orbital regime of the mission, the spacecraft will be exposed to some or all of these types. Solar cell design must incorporate an understanding of the potential sources in the operating regime of the spacecraft and the damage mechanisms caused by each.

1. Cosmic Rays

High energy particles of low density (approximately 4 particles per cm³) are dispersed somewhat isotropically throughout the galaxy. The primary component is energetic Hydrogen nuclei (protons) having energies ranging up to 10¹⁰ eV. Although the expected annual dose is a mere 1-2 Rad/year, the energies that these events occur at is sufficient to cause a phenomenon known as a Single Event Upset (SEU) [Ref. 2 pg. 213].

The SEU phenomenon is caused when a high energy particle or ray passes near a p-n junction. Due to the energy involved, currents proportional to the dose rate is generated at the junction. In electronic devices, SEU's cause events such as bit flips and latchups. The concern for solar cells is the introduction of interstitial defects, which will be discussed later in this chapter [Ref. 2 pg. 213].

2. The Solar Plasma and the Solar Wind

Solar plasma is a uniformly distributed mix of high energy electrons and protons originating from the sun. Due to the high temperature of the corona, solar protons and electrons gain enough velocity to escape the Sun's gravitational attraction. The solar wind that results emanates from the Sun omni-directionally and impacts the earth on the daylight side, streaming behind it in an elongated pattern. Figure 1 illustrates the pattern of the solar wind around the earth.

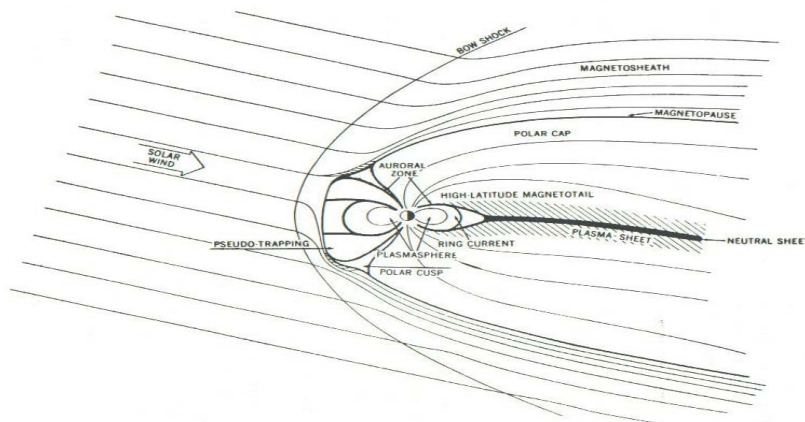


Figure 1. The Solar Wind. [From: Ref. 1 pg. 5.1]

The Earth's geomagnetic field (see Figure 2) acts as an obstacle to the solar wind. The plasma from the solar wind shapes what is known as the Magnetosphere, an area around the earth which is itself filled with plasma that originates from the Earth's upper atmosphere [Ref. 2 pg. 60].

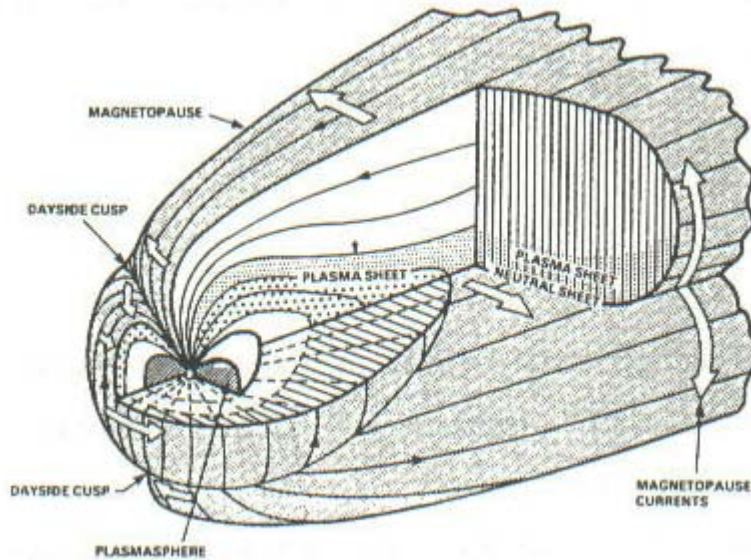


Figure 2. The Magnetosphere. [From: Ref. 1 pg. 5.5]

3. Van Allen Belts

Inside the Magnetosphere is a region known as the Plasmasphere, which contains many trapped protons, electrons and some heavy, low energy ions. The magnetic lines of force, interacting within this plasma create what are known as the Van Allen radiation belts. Although the Van Allen belts are not a source of radiation per se, the charged particles that reside within the belts do warrant an understanding due to the frequent traversals made by the spacecraft in that orbital regime.

As charged particles approach the Magnetosphere, they are altered in trajectory to follow the magnetic lines of force. Particles lacking sufficient energy to break free from that force become trapped and bounce between two reflection or “mirror” points (mirror

points occur at regions of maximum field strength in a given path). These trapped particles form what are known as the Van Allen belts (see Figure 3).

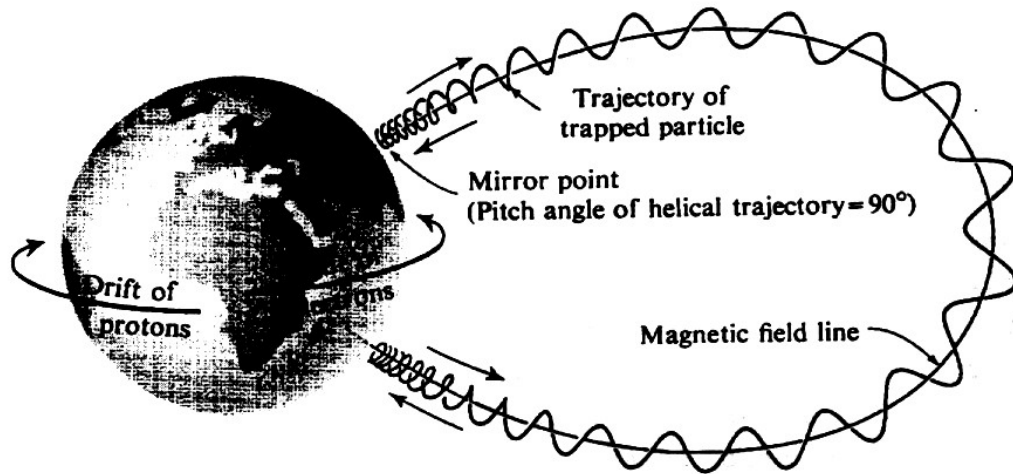


Figure 3. Trapped particles reflecting between two mirror points.
[From: Ref. 2 pg. 100]

In 1961, McIlwain introduced a coordinate system which utilizes the magnetic field B , and the adiabatic invariant I , to describe the physical situation of trapped charged particles [Ref. 2 pg. 104]. I is the length of the field line between the reflection points of the trapped particles. The parameter L is used here as a distance which is convertible to earth Radii by $R = L \cos^2 \Lambda$, where R is the earth's radius (6378 km), L is the McIlwain distance, and Λ is the magnetic latitude [Ref. 1 pg. 5-3]. Figure 4 shows the McIlwain coordinate system.

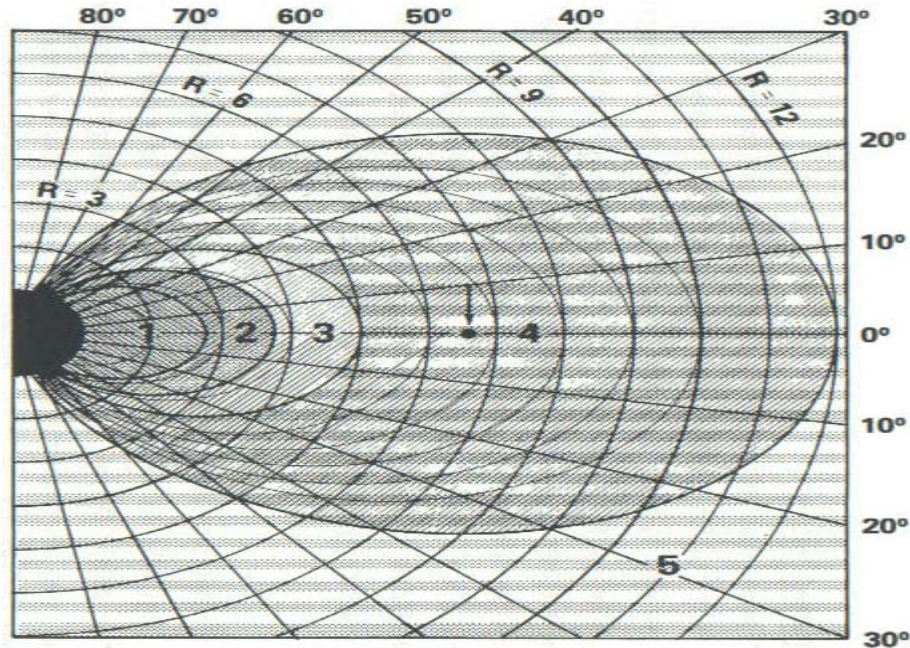


Figure 4. The McIlwain Coordinate System. [From: Ref. 1 pg. 5.5]

Particle distribution in the Plasmasphere varies depending on altitude. Intermediate energy protons exist within $L = 4$, peaking at approximately $2L$. The higher energy protons tend to migrate closer to the earth peaking at about $1.5 R_e$. Lower energy protons migrate and disperse all the way to geo-synchronous orbit. As L increases, the proton energy spectrum generally lowers [Ref. 1 pg. 5-6].

Electrons extend to the outer boundary of the Magnetosphere (approximately 8-10 R_e , depending upon solar conditions) but concentrate in two areas. The first, in a zone ranging between 1.2-2.8 L and peaks at about 1.4 L . The second or outer extends between 3-11 L and peaks anywhere between 4-5 L . The flux in these two regions is approximately $10^7 e/cm^2-s$ at energy levels on the order of 250 KeV. Figure 5 shows the distribution of charged particles in the Magnetosphere [Ref.1 pg. 5-6 to 5-7].

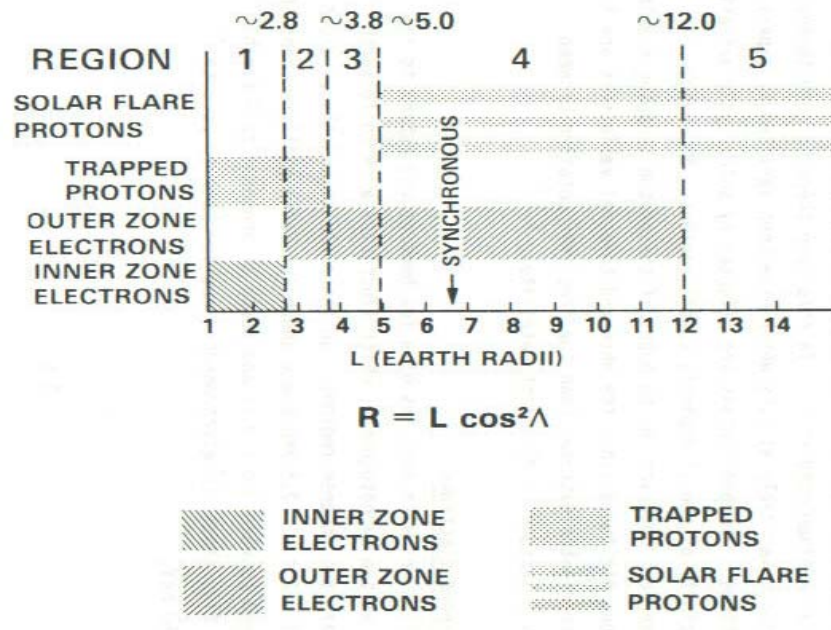


Figure 5. Charged particle distribution in the Magnetosphere. [From: Ref. 26 pg. 20]

C. INTERACTIONS

1. Wave (Photon) Effects

Photons, such as Gamma and X-rays, can interact with matter in three ways: the photoelectric effect, Compton's Scattering, and pair production.

a. Photoelectric Effect

Consider a light source of frequency f , incident upon a clean, smooth metal surface. Using Einstein's equation, the maximum energy that electrons have that are emitted from that surface is:

$$E = eV_0 = \frac{1}{2} mv^2 = hf - \Phi_0 \quad (2.1)$$

Where V_0 is the stopping potential, m is the electron mass, and Φ_0 is the work energy required to remove the electron from the surface of the metal. Analysis of

the above equation reveals that an incoming photon must have energy greater than the work function in order for photoelectric effect to occur. If this is not the case, the incident energy is simply converted to heat via kinetic energy transfer [Ref. 4 pg. 107-108] [Ref. 5 pg. 66]

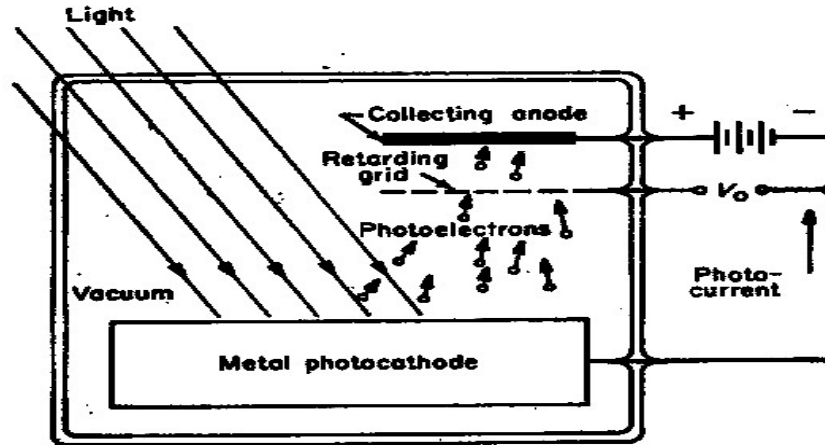


Figure 6. Photoelectric Effect. [From: Ref. 5 pg. 66]

b. Compton's Scattering

When a photon with energy $h\nu$ and momentum p collides with an electron, the photon scatters at an angle θ with respect to the initial trajectory. Part of the photon's energy is imparted to the electron that recoils and scatters at an angle ϕ with respect to the photons initial path [Ref. 5 pg. 115-116]. The collision results in an energy transfer which lowers the frequency of the photon by:

$$\lambda_1 - \lambda_2 = \frac{h}{mc} (1 - \cos\theta) \tag{2.2}$$

Where λ_1 and λ_2 represent the wavelengths of the photon before and after the collision. The change in electron energy is given as:

$$E - E_0 = (E_0^2 + p_e^2 c^2)^{1/2} - mc^2 \tag{2.3}$$

Figure 7 illustrates the effect of Compton's Scattering.

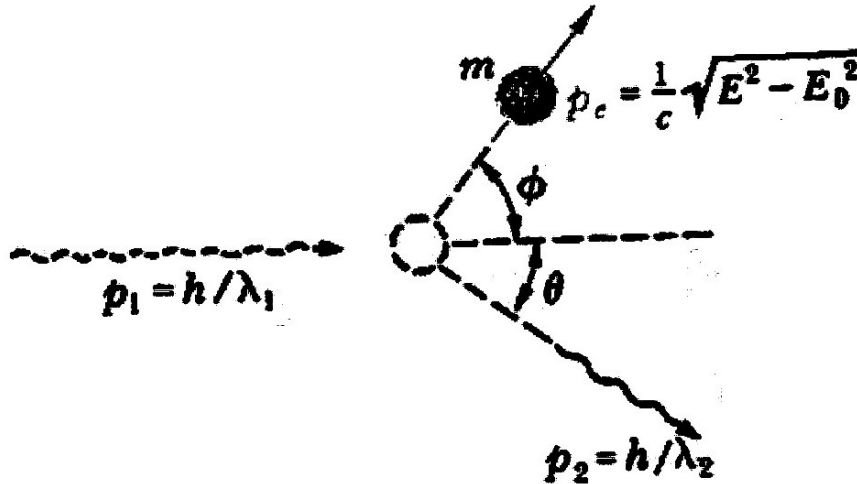


Figure 7. Compton's Scattering. [From: Ref. 4 pg. 116]

c. Pair Production

When high energy photons pass in close proximity to atomic nuclei, a recoil reaction results with the emission of either an electron-positron pair or a triplet (includes an additional electron) and the annihilation of the incident photon. The life of the positron is short, as it will soon find an electron to recombine with. This recombination creates at least two, sometimes three gamma rays (at least two in order to conserve momentum).

Determination of which of the three aforementioned effects will occur is a function of incident photon energy. Assuming a range of photon energies incident on a piece of silicon, the following distribution from Table 1 holds true: [Ref. 6 pg. 922]

< 50 keV	Photoelectric effect
50 keV – 20 MeV	Compton's Scattering
> 20 MeV	Pair production

Table 1. Energy levels associated with the wave effects.

2. Charged Particle effects:

The effect that charged particles have on matter is somewhat different than those caused by photons described above. There are three general types of material interactions caused by charged particles. They are: Inelastic collisions with bound atomic electrons and both elastic and inelastic collisions with atomic nuclei [Ref. 1 pg. 3-1].

a. Inelastic Collisions with Bound Atomic Electrons

Energetic charged particles that interact with a material have a higher likelihood of interacting with an electron in the orbit of an atom than just the nucleus of the atom itself. As the charged particle moves through the material, it undergoes collisions with these electrons, transferring kinetic energy and leaving the electrons in an excited or possibly a free state. The end state of the electron is determined by factors such as the energy of the incident particle, the collision vector and the orbit of the electron. Excited electrons will return to their normal state after emission of a photon equivalent to the amount of energy lost in going back to the stable state. Ionized (free) electrons will eventually combine with a positively charged ion.

b. Elastic Collisions with Atomic Nuclei

Coulombic reactions caused by energetic charged particles interacting with atomic nuclei can cause Rutherford Scattering (see Figure 8). Provided that the incident particle does not have sufficient energy to penetrate the nucleus, the nucleus will scatter particles at an angle θ from the incident vector. Depending on the energy of the incident particle as well as the mass and bonding strength of the nucleus, a displacement (or a series of displacements) may result.

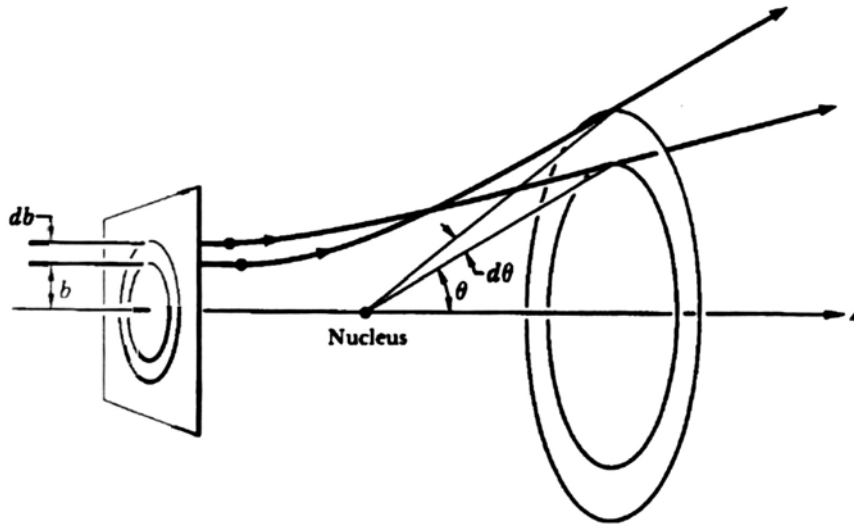


Figure 8. Rutherford Scattering. [From: Ref. 25 pg. 139]

c. Inelastic Collisions with Atomic Nuclei

Charged particles having sufficient energy and trajectory to overcome the repulsive electrostatic force of the nucleus can collide directly with it, leaving it in an excited state. The excited nucleus thus emits energetic nucleons and recoils, displacing it from its lattice site.

D. DAMAGE MECHANISMS

The discussion of the above interactions is necessary to understand their characteristics and to further categorize their effects. There are two categories of damage that concerns the degradation of solar arrays: Ionization and displacement damage.

1. Ionization

Ionization involves the removal of an electron from an atom or molecule in a given material. A measure of the intensity of ionizing radiation is the roentgen. The radiation intensity required to produce a charge of 2.58×10^{-4} coulomb/kg of air is one roentgen [Ref. 2 pg. 197].

Absorbed dose is defined as the absorbed energy per unit mass in a given material. The generally accepted unit of measure is the rad. One rad is equivalent to 100 ergs/gm or 0.01 joules/kg. By utilizing absorbed dose, radiation exposures of different types can be used to understand the overall effect on the material of interest due to protons, electrons and gamma rays [Ref. 2 pg. 197].

Solar arrays undergo various ionization related effects when exposed to a radiation source. One important effect is the darkening of array coverglasses. If an ionizing event excites an electron to the conduction band, it becomes trapped in an impurity atom and can remain stable indefinitely [Ref. 7].

Ionizations in pure silicon cause electrons of the valence band to excite to the conduction band, thus creating electron-hole pairs. These high energy particles require roughly three times the energy of an optical photon to create an equivalent pair. This means more heat losses in the material and lower efficiency.

2. Atomic Displacement

High energy protons and electrons lose much of their energy through collisions with atomic electrons. For a given material, the stopping distance is a function of incident particle energy (for energies ranging between 0.1-10 MeV). However, the dominant mechanism for solar cell degradation is the displacement of the target material within the lattice structure itself [Ref. 8 pg. 40].

Interstitials are semi-stable defects that are formed after the chain reaction of atomic collisions caused by high energy particles. Essentially they are defects in the lattice structure, which affect the valence electrons in the region. Vacancies are the voids left after an atom is moved from its lattice site. In general, these defects create additional energy states in the energy gap and lower the overall charge carrier lifetime by phenomena such as Frenkel Pairs (Figure 9) and recombination centers [Ref. 9 pg. 157].

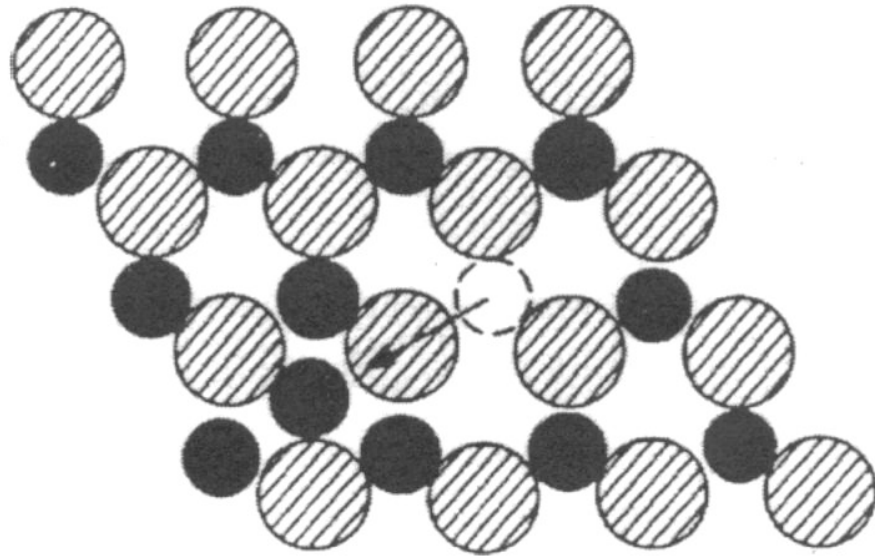


Figure 9. Frenkel Pairs. [From: Ref. 27 pg. 181]

III. SEMICONDUCTOR THEORY

In order to discuss the effects of radiation on solar cells, an understanding of semiconductor physics is required. Included is a background discussion of intrinsic and extrinsic material properties, p-n junctions, and basic diode characteristics.

A. PROPERTIES

A semiconductor is a material having physical and electrical properties that lie between those of metals and dielectrics. The atomic structure of a semiconductor is such that it will attempt to fill its outermost shell in order to reach a stable energy state. This is accomplished through ionic and covalent bonding with neighboring atoms.

Most atoms are electrically neutral, however some atoms will sacrifice one or more valence electrons in order to gain stability. When this occurs, the electrostatic attraction between the cation (positively charged ion) and anion (negatively charged ion) create an ionic bond. This kind of bonding typically occurs in atoms that are on opposite ends of the periodic table. Metals tend to lose electrons and non-metals tend to gain them.

Semiconductors made of a single element or of materials with similar electronegativities tend to create covalent bonds. Covalent bonding is the sharing of one or more electrons between atoms in order to fill their outermost shells. Materials such as silicon, which is neither metal nor a non-metal, share electrons with neighboring atoms to satisfy the valence electron populations of the bonded atoms. Although both parties share the electrons, the stability is increased and the atoms form a crystal lattice to allow a central atom to share with four neighboring atoms.

Group III-V materials such as InP have ionic bonds, but due to the small difference in electronegativity they are weaker than those of metals and non-metals [Ref. 10 pg. 10]. Typically, Group III-V compounds form a structure known as a Zincblende as shown in Figure 10.

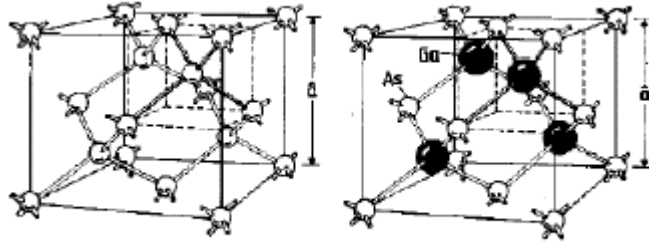


Figure 10. Diamond and Zincblende structure. [From: Ref. 10 pg. 10]

B. INTRINSIC AND EXTRINSIC MATERIAL

When a semiconductor contains no impurities, it is considered intrinsic [Ref. 1 pg. 1-7]. The primary charge carriers are supplied due to thermal excitation of the valence electrons to the conduction band. The electron hole pair concentration in intrinsic silicon is given as [Ref. 3 pg. 13]:

$$\begin{aligned}
 n_o p_o &= n_i^2 = 3.62 \times 10^{31} T^3 e^{(-E_g/kT)} \\
 &= 2.2 \times 10^{20} \text{ cm}^{-6} @ T = 300 \text{ K}
 \end{aligned}
 \tag{3.1}$$

Where

n_o = the equilibrium concentrations of conduction electrons / cm^3

P_o = the equilibrium concentration of holes

n_i = the intrinsic carrier concentration

E_G = bandgap energy (1.11 eV in Si @ 300 K)

T = temperature (Kelvin)

k = Boltzman constant (8.6171×10^{-5} eV / K)

If impurities from columns III and V of the periodic table are present in the semiconductor, thermal ionizations provide donor carriers to the surrounding material in the lattice. Column III elements thermally ionize by accepting ionized electrons from the valence band, resulting in a negatively charged acceptor impurity and a hole in the valence band. When elements from column V ionize, the result is an electron in the conduction band and a positively charged donor in the lattice. The energies required to cause these ionizations is on the order of 0.05 eV. This implies that ionization of the impurity donors is reached at approximately 300 K. Therefore it is assumed that the column III and V impurities are completely ionized at room temperature [Ref 1 pg. 1-7].

Doping is the process by which impurities are added to an intrinsic semiconductor. A significant quantity of electrons or holes are added by doping the material, causing it to have an equilibrium charge concentration of electrons or holes which greatly exceeds that of intrinsic material. In p-type material, excess holes are added by doping intrinsic material with a column III element. Conversely, adding elements from column V creates n-type material. Material doped in such a manner is referred to as extrinsic. The relationship of thermal equilibrium applies to extrinsic material as well as intrinsic. Therefore, the product of the conduction electron and hole population must equal a constant [Ref. 3 pg. 14].

Although the number of dopant atoms added to a given material is small, the percent change is significant. Consider intrinsic silicon, which has a charge carrier concentration of one electron per 10^{12} Si atoms. If a dopant material is added such that one electron per 10^7 atoms is added, that is an increase in charge carrier concentration of 10^5 [Ref. 3 pg. 8]. A notional depiction of the crystal structures of intrinsic and extrinsic material is given in Figure 11.

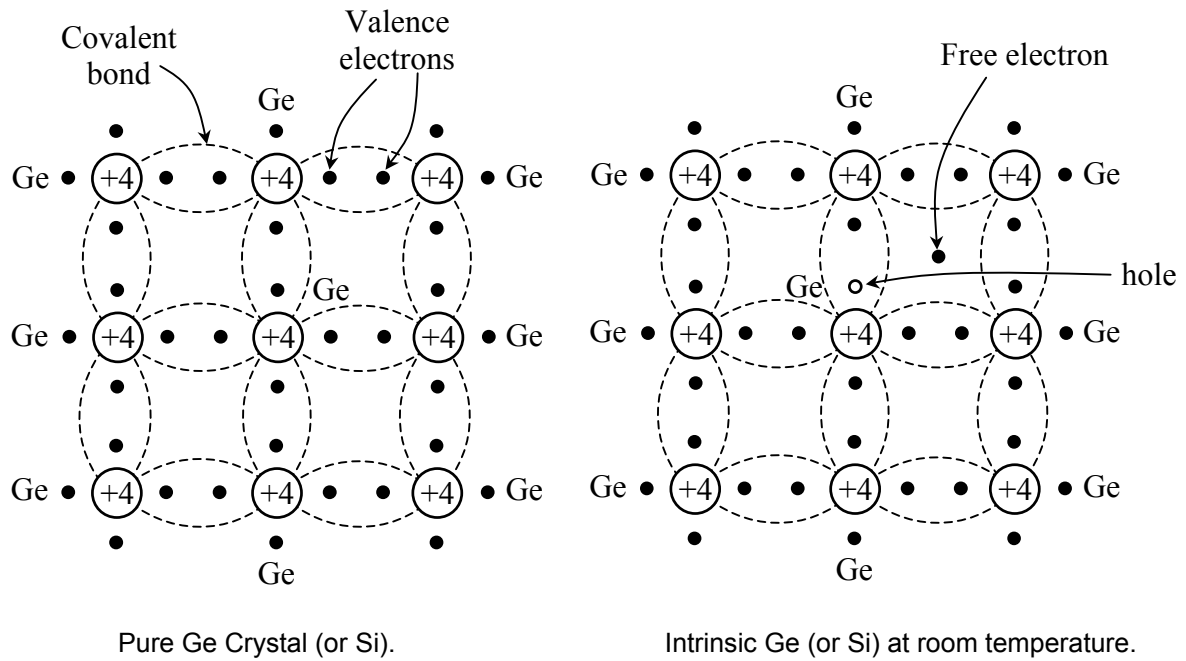


Figure 11. Intrinsic and extrinsic crystal structure. [From: Ref: 3 pg. 8]

C. BAND GAP ENERGY

In 1913, Bohr developed the quantum model of the atom. Although the Bohr model has been replaced as more accurate models have been developed, it does provide a basic understanding into atomic structure.

There are four assumptions to Bohr's model: 1) The atom is held together by Coulombic forces; 2) electrons have elliptical orbits; 3) electron angular momentum exists in discrete quantum values; and 4) electrons emit and absorb energy in discrete quanta between energy levels [Ref. 2 pg. 5].

The energy of the electron must have sufficient kinetic energy to overcome the coulombic force that binds it to the atom. That coulombic force varies inversely with the electron radius. If the atomic number Z defines the number of protons in the nucleus, then the coulombic force of attraction can be found by [Ref. 2 pg. 7]:

$$U = q_1 q_2 / 4\pi\epsilon_0 r = -Ze^2 / 4\pi\epsilon_0 r \quad (3.2)$$

The kinetic energy required to overcome the coulombic force is:

$$T = \frac{1}{2} mv^2 = \frac{1}{2} Ze^2 / 4\pi\epsilon_0 r \quad (3.3)$$

$E = U + T$ where E is the energy, U is the coulombic energy and T is the kinetic energy.

Then the total energy is given as

$$E = U+T = -1/2 Ze^2 / 4\pi\epsilon_0 r \quad (3.4)$$

Therefore, if we know the radius of the orbit, the energy of the electron is well defined [Ref. 2 pg. 8].

In a crystalline structure, the electron energy is more complex because the atoms in neighboring lattice sites affect it. However, the electrons still occupy discrete and predictable energy states. For electrons in the outer shell of a semiconductor, there are two states. Valence level electrons in the ground state are considered to be in the valence band, while excited electrons are in the conduction band [Ref 11 pg. 813].

This concept of band gap energy plays a key role in fundamental solar cell operation and design. Because electrons have quantized energy levels determined by their orbit and surrounding atoms in the lattice, materials and dopants are carefully managed to take advantage of the full spectrum. Energy band diagrams like the one in Figure 12 show the two states of the electron and the region between known as the band gap.

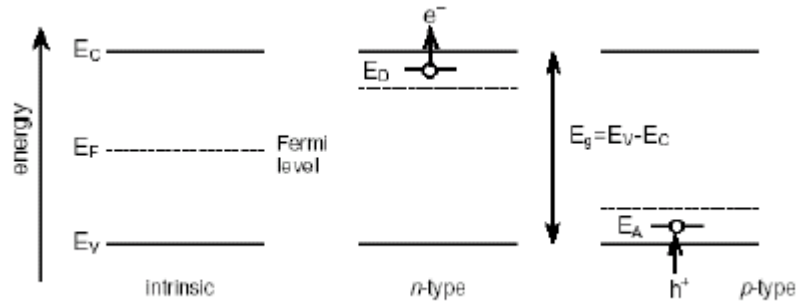


Figure 12. Energy band diagrams for intrinsic, n-type and p-type material.
[From: Ref. 29 pg. 10]

D. CARRIER TRANSPORT

Two means of carrier transport or “current” occur in semiconductors. Charged carriers drift in the material driven by the changes in electric field. In n-type material, the drift current is described by [Ref. 12 pg. 15-17]:

$$\mathbf{J}_n = q \mathbf{n} \mu_n \mathbf{E} \quad (3.5)$$

Such that:

- J_n = electron density (amperes / cm²)
- q = electron charge (coulomb)
- n = electron concentration (cm⁻³)
- μ_n = electron mobility (cm²/volt sec)
- E = electric field (volts/cm)

The other mechanism of charge transport in a semiconductor is diffusion. Diffusion current is created due to charged carrier concentration gradients. For holes, the current is given by the following:

$$\mathbf{J}_p = -q \mathbf{D}_p \mathbf{dp/dx} \quad (3.6)$$

Where:

- J_p = hole current density (A/cm²)
- D_p = hole diffusion constant (cm²/sec)
- dp/dx = hole concentration gradient

An expression for the carrier transport can be obtained by adding the drift and diffusion currents. For the case of holes, the expression is given as:

$$\mathbf{J}_p = q (p \mu_p \mathbf{E} - D_p dp/dx) \quad (3.7)$$

E. THE P-N JUNCTION

1. Creation of the P-N Junction

Discussion to this point has focused on semiconductor materials and their properties. However, there is little practical application without a means to realize the potential from the production of the charge carriers. Like a battery, a potential must exist in order to have a current flow. For a solar cell, the p-n junction is the mechanism by which this is achieved.

As the name implies, the p-n junction is formed by joining p-type material which has excess holes with n-type material which has excess electrons. When this union is made, a transient exchange of the excess carriers takes place due to the large charge carrier concentration gradient on both sides of the junction. The electrons migrate from the n-material to the p-side and combine with the excess holes. As this diffusion progresses an electric field develops which creates a drift current that opposes the diffusion current [Ref. 13 pg. 138-139].

As the excess electrons leave the n-region, they leave behind positively charged dopant ions. Likewise the holes in the p-region are depleted and leave negatively charged dopant ions. Eventually, an equilibrium condition is formed such that there is a depleted n-region that has a positive charge and a p-region that has a negative charge, and the net drift and diffusion current is zero. This region as a whole is known as the depletion region Figure 13 depicts the p-n junction.

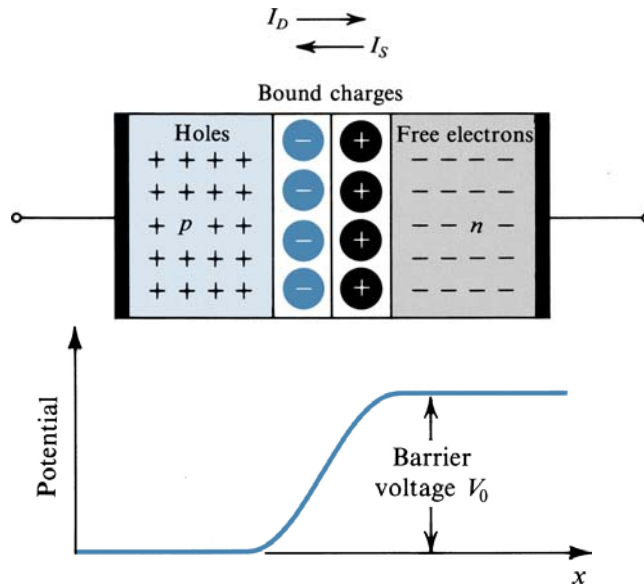


Figure 13. The p-n junction. [From: Ref. 3 pg. 14]

2. P-N Junction Behavior

The p-n junction is the fundamental component of solid-state devices, including solar cells. The diode is merely a p-n junction with terminals attached. Behavior of the p-n junction varies depending on the conditions of bias placed upon it. First a look at the diode under reverse bias conditions as in Figure 14.

Under reverse bias conditions a current is flowing from n to p. Let this current I , be less than the drift current I_s . As electrons flow from n to p, positive ions are formed in the n region widening the n-side depletion zone. A similar event occurs in the p-side of the depletion region. This raises the potential difference at the barrier and results in a lower diffusion current I_d . An equilibrium will be reached when the diffusion current lowers to the point where $I = I_s - I_d$. This results in a potential difference across the diode V_r [Ref. 3 pg. 15].

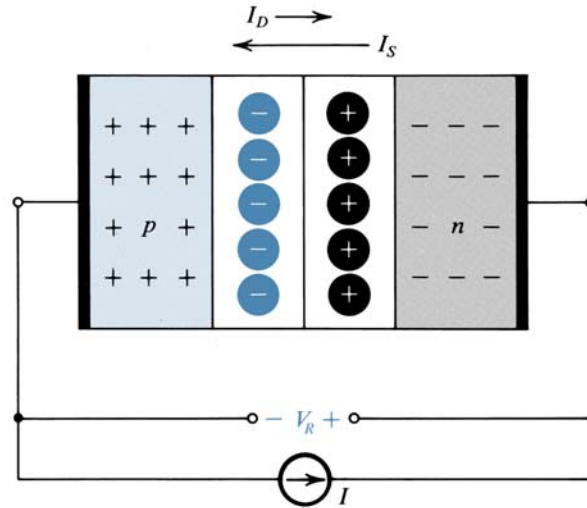


Figure 14. The p-n junction under reverse bias conditions. [From Ref. 3 pg. 15]

Let the current I increase such that $I > I_s$ as in Figure 15. The depletion region continues to widen. This occurs until the barrier voltage is so high that $I_d = 0$. When the barrier voltage increases to the diode breakdown voltage, an exponential increase (nearly instantaneous) in I occurs and the diode acts much like a short circuit. There are two types of breakdown that occur in diodes under reverse bias conditions: Zener and Avalanche [Ref. 3 pg. 16].

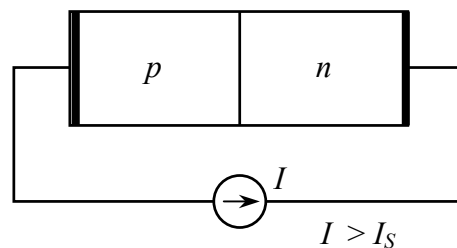


Figure 15. The p-n junction in the breakdown region. [From: Ref. 3 pg. 16]

Zener breakdown results from the increasing electric field in the depletion region. This electric field becomes strong enough to break the covalent bonds and results in the generation of electron-hole pairs. Carriers are generated in this fashion in large numbers until only the external circuit limits the current. While Zener breakdown is a field effect, Avalanche current is a kinetic energy phenomenon. The minority carriers that cross the depletion region gain significant kinetic energy as the field increases to drive them. This kinetic energy is transferred to other atoms through collisions. Depending upon the initial energy and angle of the collision, electron-hole pairs can be generated in the target atoms. These additional carriers gain energy and undergo the same process, thus increasing the current to short circuit conditions. The types of breakdown and the voltage ranges in which they occur are listed in Table 2.

Diode Voltage	Effect
$V_z < 5V$	Zener Effect
$5 < V_z < 7$	Zener or Avalanche
$V_z > 7$	Avalanche

Table 2. Effect of diode voltage on breakdown mechanism.

The diode behaves quite differently under forward bias conditions. Let a current I , flow from p to n as in Figure 16. This current adds to the existing majority carrier concentration on both sides of the junction, some of which combine with the charged ions left behind at the creation of the junction. This reduces the width of the depletion region and barrier voltage across the junction until $I_s - I_d = I$ at equilibrium. As holes are injected into the n-region, the minority carrier concentration is increased above the thermal equilibrium level. Because the junction potential is lowered, more electrons now have enough energy to overcome the potential hill and diffuse to the p side. The compliment is true for holes from p to n [Ref. 3 pg. 17].

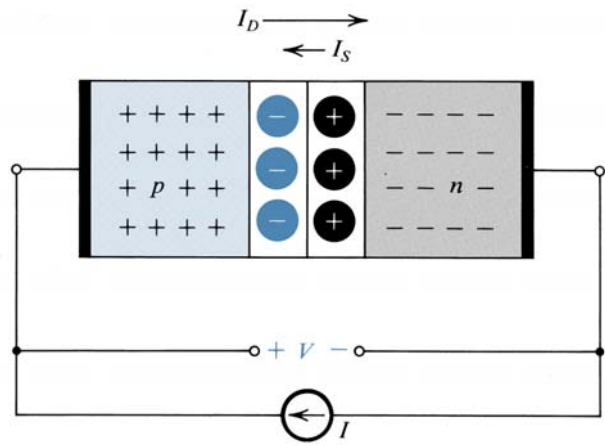


Figure 16. The p-n junction under forward bias conditions. [From: Ref. 3 pg. 17]

The behavior of diode current is shown graphically in Figure 17. Mathematically, it is written as:

$$I = |I_{gen}| (e^{qV/kT} - 1) \tag{3.8}$$

Where:

I_{gen} = generated current in the transition region

q = charge of the carrier

V = applied voltage

k = Boltzman's constant

T = temperature (K)

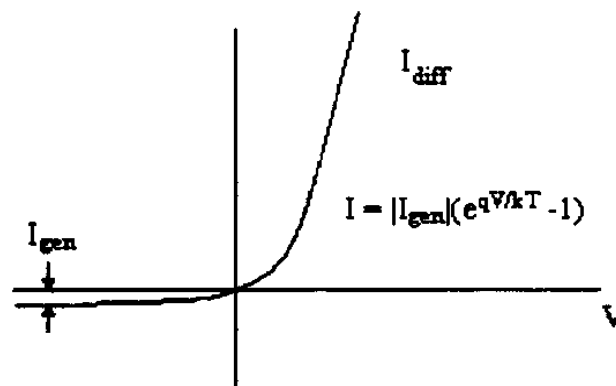


Figure 17. Diode characteristic curve. [From: Ref. 16 pg. 33]

3. Charge Carrier Lifetime

The notion of charge carrier lifetime is the following. Suppose that an event occurs such that an electron hole pair is produced. This pair causes the equilibrium balance of carriers to be upset, and with no load on the p-n junction, will eventually return to that equilibrium through a natural decay function. Under thermal equilibrium conditions, the generation and recombination rates are equal. For a normal diode, this is relatively uneventful. However for a solar cell, the fate of these carriers is directly related to the cells performance characteristics.

Unlike typical diodes, the solar cell uses incident light to create these carriers, which in turn drive a load attached to the cell. The problem is getting the particles to “live” long enough so that they can get to the terminals of the cell and produce a current in a load. The road to freedom for the pair is perilous and many of the carriers are lost to recombination processes along the way. Analysis of these processes and how to mitigate them is important in order to design solar cells that can meet the performance characteristics desired on today’s high powered spacecraft.

The charge carrier lifetime is defined as “the average time that carriers exist from generation to recombination” [Ref. 14 pg. 105]. Quantitatively, the carrier lifetimes for electrons and holes can be expressed as:

$$\tau_e = 1/\sigma_n N_t \quad \tau_p = 1/\sigma_p N_t \quad (3.9)$$

Where σ_n, σ_p are the absorption crosssections for electron and hole capture. The distinction between minority and majority carrier lifetimes is dependent upon whether n or p-type material is being referenced [Ref. 15 pg. 36-37].

Depending upon the material used, there are two different modes of recombination. Materials in which the electron-hole pair can recombine with a zero change in momentum are considered direct materials. Materials that require a change in the momentum of the electron in order to transition from the conduction to the valence

band are called indirect materials. Gallium Arsenide and Silicon are examples of direct and indirect materials respectively.

Recombinations occur by various means. First, an electron can simply transition from the conduction to the valence band, yielding a photon with an energy $h\nu$ equal to the change in energy state [Ref. 16 pg. 18-22]. This is the result seen when lasing or energizing an LED. Second, an electron may transfer its energy kinetically to another electron. This is known as Auger recombination. Third, an electron can give up its energy by emission of a phonon. A phonon is a mechanical vibration of the crystal lattice in discrete quanta.

Recombination events in indirect materials occur predominately at recombination centers created by impurities or radiation damage to lattice sites. The recombination site provides a conduit for the momentum change in indirect material. At equilibrium, these recombination centers or “traps” are filled, occupying an energy level between the conduction and valence bands. As electrons fall from this energy state E_r , to the valence band, they leave behind a hole, which then traps an electron from the conduction band. These transitions do not meet quanta criteria for generation of photons, rather they yield phonons to the lattice structure generating heat. Although the recombination center returns to its equilibrium state, the cost to the cell is the loss of an electron-hole pair, resulting in lower cell efficiency [Ref. 13 pg. 104-105]. Figure 18 illustrates the capture process.

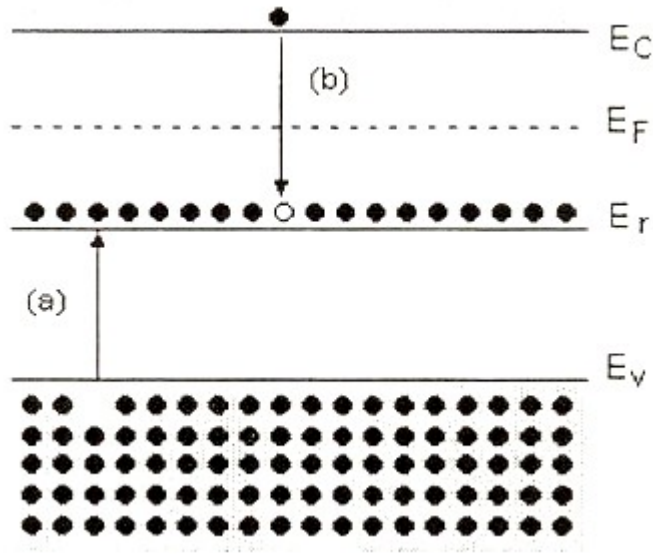


Figure 18. The capture process of an electron-hole pair at a radiation induced recombination energy level. [From: Ref. 16 pg. 21]

The minority carrier lifetime depends upon several factors. In direct bandgap material, minority carrier lifetime tends to be short: on the order of 10^{-9} to 10^{-7} sec. Intuitively, the zero momentum change makes the transition from the conduction to the valence band more probable. In indirect material, carrier lifetimes are longer: on the order of 10^{-7} to 10^{-3} sec. This is why silicon is such a popular choice for solar cell material. However, the introduction of impurities creates more “traps” resulting in the loss of electron-hole pairs. For this reason, the purity of indirect band-gap material must be strictly controlled to prevent creation of recombination centers [Ref. 17 pg. 58-59].

IV. SOLAR CELLS

Solar cells have become the primary source of power for earth orbiting spacecraft since their introduction by Bell labs in the early 1950's. Technological advances in materials and design have raised the operating efficiency of these devices from four percent to as high as thirty percent today. As spacecraft become larger, more complex, and longer lived, the solar cells have had to follow suit. However, some unique problems exist for the solar cell that can become a single limiting factor in the mission lifetime of the spacecraft, specifically the degradation of solar cells in the radiation environment. This chapter provides a brief overview of solar cell design and operating parameters to provide the reader with an understanding of the tools used to analyze solar cell performance.

A. SOLAR ENERGY

The sun generates energy by the fusion of Hydrogen into Helium at the rate approximately 6×10^{11} kg of Hydrogen/sec. The resulting temperature at the surface of the sun is approximately 5800 K [Ref. 2 pg. 55]. The energy that reaches the earth has a spectrum that resembles the diagram of Figure 19. This diagram depicts the spectrum of solar energy at the distance of one astronomical unit or AU (assuming no atmospheric interference) superimposed over a black body. The AU is the mean distance from the earth to the sun and is measured as 1.49598×10^8 km. Notice that the solar spectrum closely resembles that of a black body. The black body curve proves useful because power flux from a black body depends only upon the surface temperature. The total calculated power output of the sun is 3.86×10^{26} Watts. Of this, the power at 1 AU is 1370 W/m^2 .

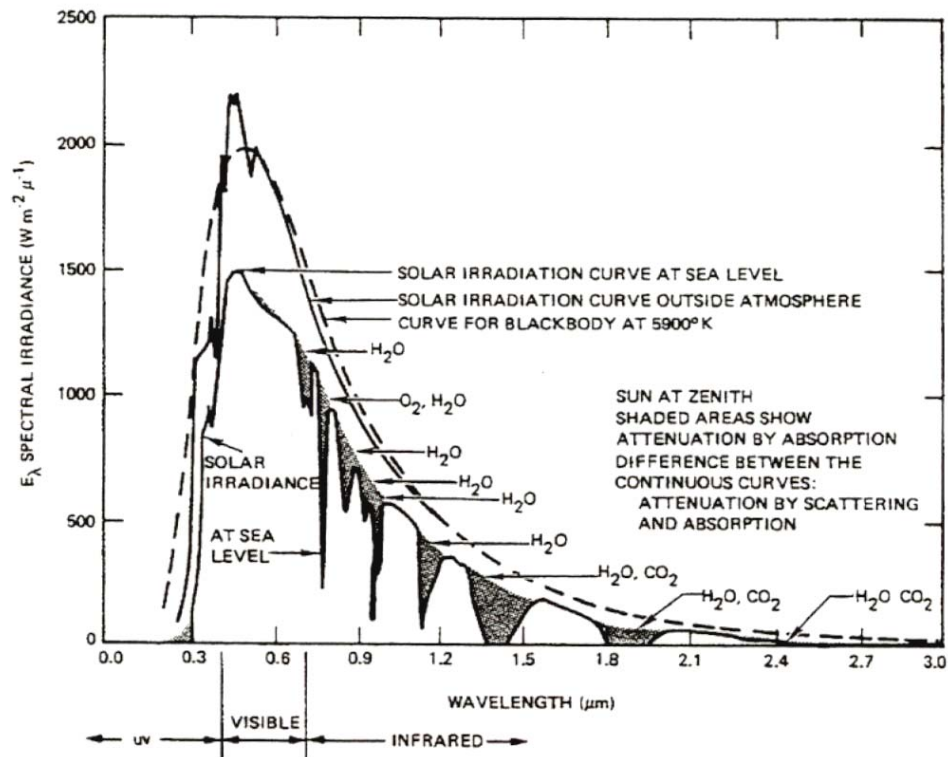


Figure 19. Spectral Irradiance and 5800K Blackbody curves. [From: Ref. 18 pg. 10]

B. BASIC OPERATION

Consider a thinly constructed p-n junction as discussed in the previous chapter. Allow a solar spectrum to fall incident on its surface. Due to the photonic effects described earlier in chapter one, numerous electron hole pairs are developed. The electric field created by the formation of the p-n junction helps to separate and collect the electrons and holes such that they can be used to drive current into a load. Recall that without the electric field, the electrons and holes would simply recombine as the semiconductor returns to thermal equilibrium [Ref. 1 pg. 1-1].

The solar cell p-n junction is very thin and flat with contacts on the front and back of the cell. This facilitates good light penetration as well as lessening the distance

necessary for minority carriers to travel before reaching the contacts of the cell. A grid is placed on the sunlit side of the cell to both allow the passage of light and to collect carriers for transport to the load. Figure 20 shows the basic anatomy of a solar cell.

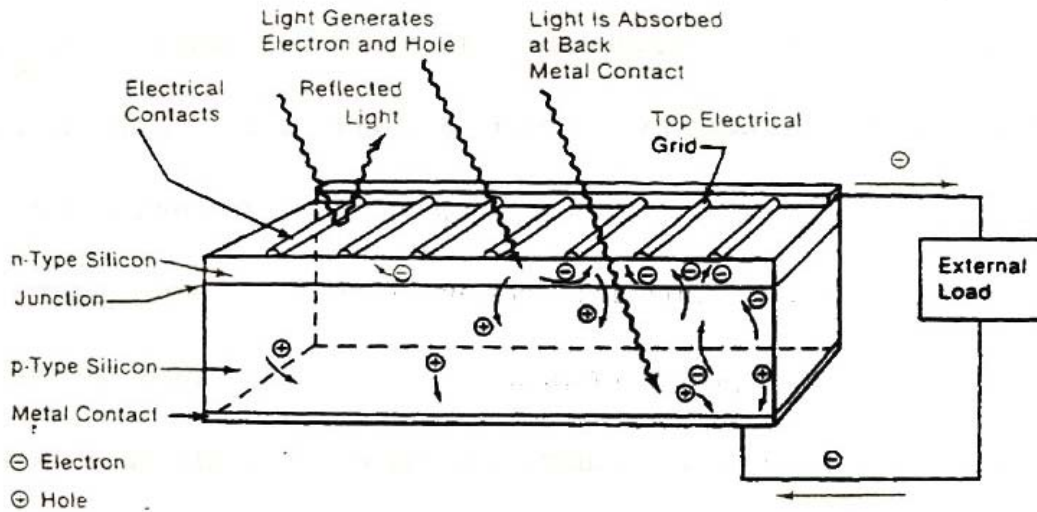


Figure 20. The basic solar cell. [From: Ref. 3 pg. 15a]

As mentioned before, the solar cell produces electron hole pairs due to the incident photon flux on its surface. The number of pairs produced depends upon the spectrum of incident light and the material of the solar cell. In silicon for example, blue spectrum light (0.35μ) will travel roughly 0.2 microns before being completely absorbed (99%). Light from the peak of the solar spectrum (0.46μ) travels 2 microns into the material. And light that we see as red (0.95μ) travels up to 200 microns before being absorbed [Ref. 1 pg. 1-1]

It can be seen then that the distribution of carriers generated is not uniform through the slice. Solar cell designs must take advantage of this in order to place contacts and junctions at the proper depths in order to prevent excessive recombination losses. Figure 21 illustrates the carrier production through the cell cross section.

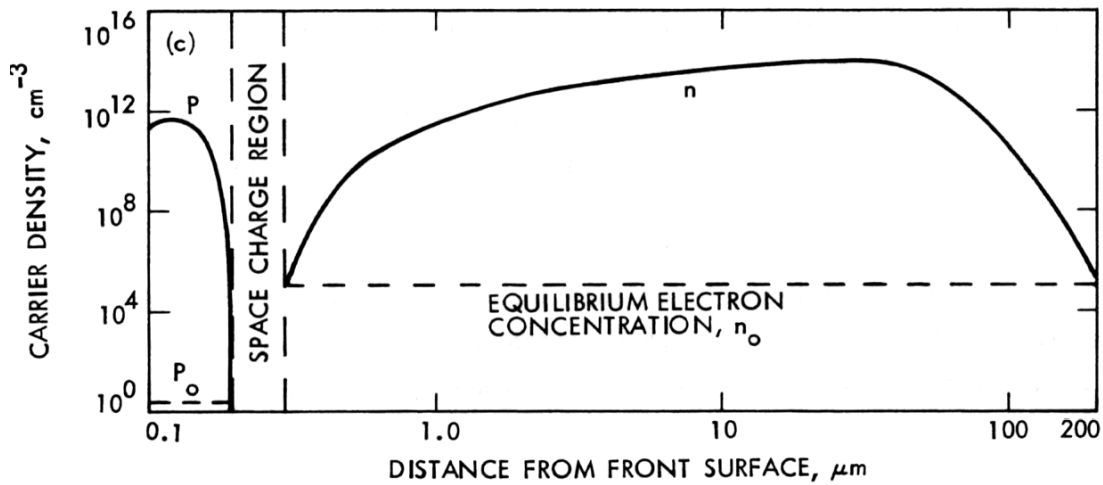


Figure 21. Plot of carrier concentration versus cell depth for an illuminated cell. [From: Ref. 1 pg. 1.2]

C. PARAMETERS

It would be difficult to look inside and probe around a solar cell to measure specific things such as electron hole pair production or electric field width and intensity. However, the cell behaves in a predictable and consistent manner such that one can deduce the cells performance by observing some well defined and common output parameters. There are three parameters that describe the solar cells operating performance: Open circuit voltage; short circuit current; and maximum power out [Ref. 18 pg. 10-12].

The open circuit voltage (V_{oc}) is the voltage generated by a single cell given a standard incident light source (typically AM0) under no load conditions. The short circuit current is the current passing through the cell under AM0 conditions with a zero ohm load. The maximum power point is the point such that the product of cell current and voltage is a maximum under AM0 conditions. These parameters are obtained by generating a current-voltage (I-V) curve as shown in Figure 22.

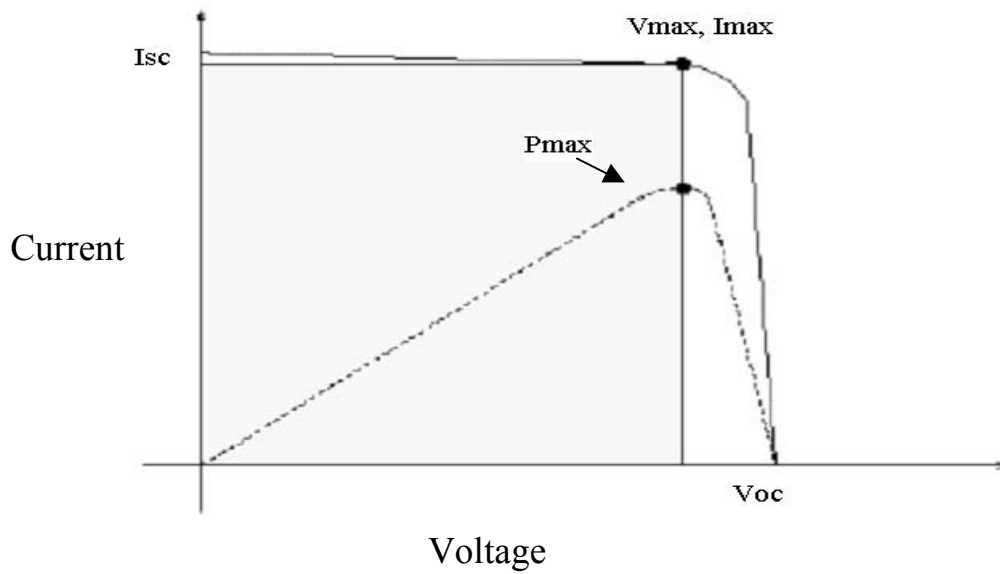


Figure 22. I-V curve with performance parameters. [From: Ref. 18 pg. 11]

From this I-V curve, a snapshot of the overall performance of the cell can be obtained. Additionally, other parameters that are artifacts of these performance parameters are the fill factor (FF) and cell efficiency (η). The fill factor is a measure of how much of a voltage drop occurs due to internal resistance as the current increases. Cells with a low fill factor have very rounded I-V curves and are an indication of significant losses in the cell design. The fill factor is the ratio of the max power P_{\max} to the product of V_{oc} and I_{sc} .

$$\mathbf{FF = 100 \times (P_{\max} / (V_{oc} \times I_{sc}))} \quad (4.1)$$

Cell efficiency measures the ratio of input power to the cell generated power. This is accomplished by comparing the max output power of the cell to the power flux density incident on the cell as follows:

$$\mathbf{\eta = (P_{in}/P_{out}) \times 100} \quad (4.2)$$

Where P_{in} is 1353 W/m^2 at AM0.

D. RADIATION EFFECTS ON OUTPUT PARAMETERS

The output parameters of solar cells mentioned above are used as a benchmark to determine the performance level of the cell. When these parameters begin to deviate from the norm in some manner, it is an indication of material degradation. Testing of solar cells under varied environments have yielded noticeable and repeatable trends in the data over time. The radiation environment is no exception.

In chapter one the effects of radiation were discussed with respect to damage to the lattice structure of semiconductors. Furthermore, the effect of that damage on carrier lifetime was earlier in this chapter. Going one step further, this section will discuss the effect of radiation damage to the output parameters and how it occurs.

1. Open Circuit Voltage V_{oc}

As previously mentioned, there is a noticeable decrease in minority carrier lifetime (τ) as a function of radiation dose. This in turn has a direct effect on V_{oc} . The radiation flux creates an increase in generation current in the depletion region of the junction. This increase in charge carriers in the depletion region lowers the number of fixed charge carriers as recombinations occur. The result is a lower electrostatic potential at the barrier.

Charge “traps” also lower V_{oc} . Recombination centers created by radiation damage can trap and release charges from the conduction band to an intermediate band associated with the trap. When a transitional energy is added to the trap, the trap can release the carrier back to the conduction band. As the number of these traps increases, the number of trapped charges increases, thus lowering the number of charge carriers in the cell at a given time. This lowers the current in the cell, resulting in a lower V_{oc} .

2. Short Circuit Current I_{sc}

The potential created by the p-n junction accelerates photo-generated minority carriers across the depletion region, adding to the cell current. Charge carrier lifetime

must be sufficient such that these carriers are not absorbed before being swept across the junction. Radiation induced defects create damage in the cell which create recombination centers and change the overall bandgap energy of the cell. This results in a lower carrier concentration and thus a lower I_{sc} .

3. Maximum Power P_{max}

The lower V_{oc} and I_{sc} in a radiation damaged cell dictate that P_{max} must also be lower. Recombination current outside the depletion region reduces the minority carrier concentration. This has the effect of lowering the short circuit current as well as the current for all potential values across the cell. The additional generation current inside the depletion region lowers the overall potential of the depletion region, thus lowering V_{oc} as well as the voltages for all currents [Ref. 12 pg. 47-50].

E. MULTI-JUNCTION CELLS

From the very beginning of the space program, spacecraft have grown in size and power requirements. Due to factors such as available space and launch costs, it is not feasible to simply put more and more solar cells on the vehicle. Solar cell technology has grown to meet the power requirements and weight budgets of spacecraft by delving into new materials and designs.

As discussed in chapter two, semiconductors have different bandgap energies and recombination characteristics. Previously, a discussion of silicon solar cells revealed that for a 200 micron slice, the high energy visible light (up to 0.95μ) is stopped within the first two microns of thickness. If materials of proper thickness and bandgap energies are stacked atop each other in the right order, the spectrum can be more effectively utilized (see Figure 23).

AM0 Solar Spectrum 1350 W/m²

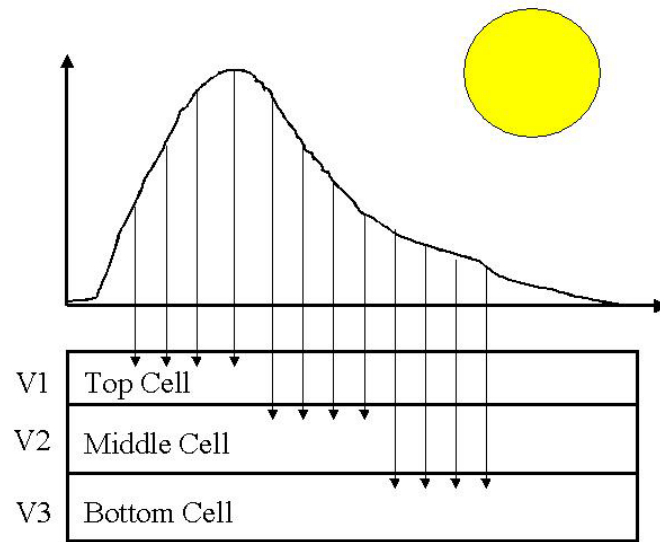


Figure 23. Notional depiction of multi-junction spectral utility. [After: Ref. 27 pg. 37]

Multi-junction solar cells utilize semiconductors with bandgap energies that span the AM0 spectrum. These cells consist of several p-n junctions stacked in the order of their respective bandgap energies. Large gap cells are placed at the top, while the lower gap cells are sequentially placed beneath. The large bandgap cells absorb the high frequency (Blue) light and allow the lower frequency light to pass through to the materials that more effectively utilize that part of the spectrum. Of the various designs of multi-junction cells, the monolithic multi-junction (or tandem) cell is the preferred design.

Just as different materials have varying band gap energies, they also have different current densities. The implication of this is that the layers cannot be connected in parallel. This adds a dimension of difficulty to creating the multi-junction cell. Ideally, all of the cells should stack neatly, yield identical currents and be joined in series so that the voltage of the cell is the sum of the individual cell layers.

Monolithic tandem cells are grown in layers with a single growth run connected by a highly doped p-n junction called a tunnel junction. A tunnel junction connects the different band gap layers in a series configuration. This facilitates a cell with a constant current in the layers and the voltages are additive.

The properties of a tunnel junction facilitate electro-optical coupling of the different layers, yet produce no carriers. Carrier production would be counter-productive to the cell as a whole. Because of the high doping levels, the potential barrier width is very thin, on the order of 100 angstroms.

The tunnel junction is a product of quantum physics and cannot exist in the classical sense. In the classical sense, the barrier formed by the electric field would be sufficient to prevent the particle from passing through. However, given a very thin potential barrier, there exists a level of uncertainty about the position of an electron near that barrier. For tunneling to occur, three conditions must exist: 1) there are occupied energy states on the same side from which the electron tunnels; 2) an unoccupied energy state on the opposite side exists; 3) the junction has a low potential barrier and sufficiently narrow width to allow a finite tunneling probability; and 4) momentum is conserved [Ref. 19 pg. 517-518].

When reverse biased, the current increases exponentially. However when forward biased, the current rises to a local maximum, drops to a local minimum, and then rises exponentially with increasing voltage. There are three current components in the tunnel junction that cause this characteristic output: Band to band tunneling, thermal current, and excess current. Figure 24 illustrates the I-V curve of a tunnel junction.

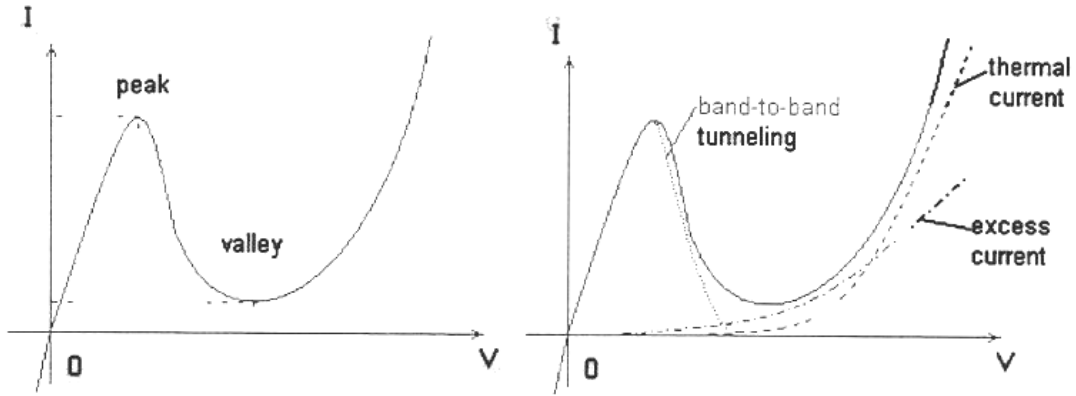


Figure 24. Tunnel junction I-V curve (left) and the current components that make up the I-V curve (right). [From: Ref. 16. pg. 53]

F. ANATOMY OF A MULTI JUNCTION SOLAR CELL

In the previous sections, the properties and characteristics of solar cell materials have been introduced. This section describes a typical multi-junction solar cell to provide the reader with an overall understanding of how the individual components function as a unit [Ref. 16 pg. 62-65]. As a reference, typical materials used are listed in Table 3.

Material	Lattice Constant	Bandgap
Ge	5.66	.66
GaAs	5.65	1.42
GaInP	5.65	1.9
AlGaAs	5.66	1.99
AlInP	5.66	2.23

Table 3. Lattice and Bandgap properties of the Spectrolab Triple-Junction cell materials.

As with most semiconductors, the material is grown in a bottom-up fashion. To start, a p-doped substrate is laid out on the back contact of the cell. This is used as a base to provide structural integrity to the device. In this case Germanium (Ge) is used because the crystal lattice is nearly identical in geometry to that of GaAs, yet stronger and cheaper to make. To finish this junction, the n-doped Ge layer is grown.

On top of this first diode, a window made of a material such as AlGaAs is grown. This allows a physical and electrical bond between the different materials. The window is very thin (approximately 25 nm) and does not contribute electron-hole pairs to the cell. The selected window material must have sufficiently large bandgap energy such that it does not interfere with the photons meant for the material below it. To provide a connection between the different active sections of the cell, a tunnel junction is grown atop the window.

Just above the tunnel junction, a back surface field (BSF) window is grown. The BSF provides an electric field near the bottom of the cell that essentially “pushes” minority carriers that would naturally migrate to the back surface, toward the junction. The result is a window that acts as a mirror for photo-generated carriers which aids in maximizing the efficiency of the cell [Ref. 1 pg. 1-34].

On the top of the BSF, the middle junction is grown from a material such as GaAs. By design, the bandgap energy of GaAs (1.42 eV) is higher than that of the materials below to allow unusable photons to filter through to the materials below, which can utilize them. A window of yet higher bandgap energy is grown on top of the GaAs layers, topped by another tunnel junction and window.

The top cell material is grown from GaInP and has the highest bandgap energy (1.9 eV) of the active materials in the cell. In perspective, all light with wavelengths greater than 650 nm can pass through this first junction. Most of the high-energy photons are utilized in this first layer.

The top of the cell consists of a window, topped by an anti-reflective coating (AR) and then finished by the cap and top contact. The AR coating is designed to reduce the reflection of light in the spectrum that the cell operates. For light having a wavelength range of $0.9\mu \leq \lambda \leq 0.4\mu$, approximately 98% of the incident light is absorbed [Ref. 20 pg. 203]. Topping the AR coating is the cap. This material draws carriers toward the surface contact and acts as a thermal barrier during the bonding process to prevent damage to the rest of the cell. Figure 25 shows a sketch of the constructed cell.

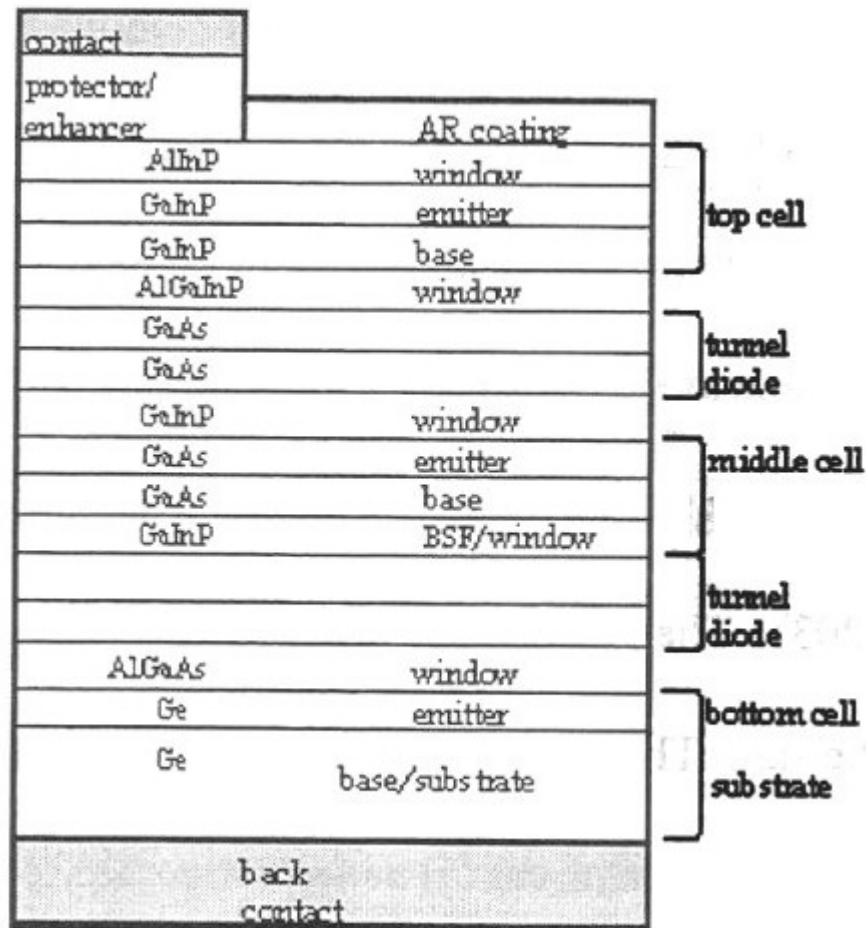


Figure 25. Cross-section of a triple junction cell. [From: Ref 16 pg. 64]

V. THE NAVAL POSTGRADUATE SCHOOL LINEAR ACCELERATOR

The Naval Postgraduate School (NPS) Linear Accelerator (LINAC) was used to provide the high-energy electron fluence required for this experiment. Built in 1965 based upon a design used at Stanford University, the NPS LINAC has been a key enabler for research in the field of space radiation effects as well as many other applications.

A. BASIC OPERATION

The purpose of the LINAC is to take relatively low energy electrons from an electron gun, accelerate them, and then focus them on a target of the users choosing at the appropriate energy and flux. The electron gun is a cathodic grid, which generates electron beam pulses at around 80 keV and then injects them into a waveguide. From there, three accelerator sections powered by 22 MW Klystron amplifiers accelerate the electrons. The number of Klystron amplifiers used controls electron energy. Each amplifier provides acceleration to the electrons that yields 30 MeV of energy. After the electrons are accelerated to the desired energy level, they are steered and collimated using two quadrupole magnets to form a beam on target between 4mm to 5 cm in diameter [Ref. 22 pg. 11-24] [Ref. 23 pg. 42-43]. Figure 26 depicts a basic layout of the LINAC.

NPS 100 MeV Linear Accelerator

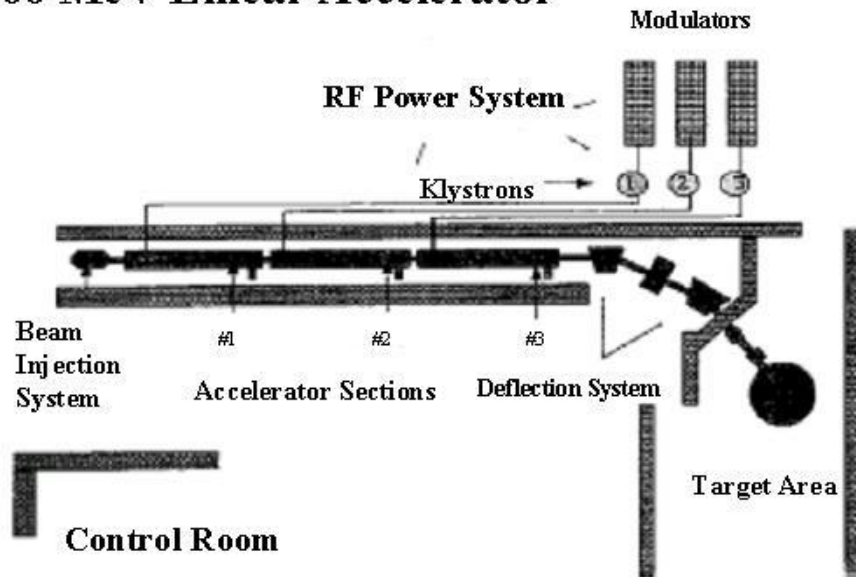


Figure 26. The Naval Postgraduate School LINAC. [From: Ref. 27 pg. 15]

B. BEAM FORMATION AND TRANSMISSION

As the name implies, the LINAC accelerates particles (electrons) in a straight line. The 80 keV electrons leave the gun as a series of pulses having a relatively uniform and steady peak amplitude and short rise and fall times. The traveling wave generated by the Klystron amplifiers is traveling down each accelerator section at the speed of light. Due to the differential velocity, some of the electrons can be lost. To maximize the electron beam, a means of concentrating the electrons in a suitable phase for travel down the wave is necessary. The pre-buncher assembly seen in Figure 27 accomplishes this. The pre-buncher delays electrons that arrive too early for the wave and “pushes” along those that are straggling, effectively minimizing the destructive interference of the two waves.

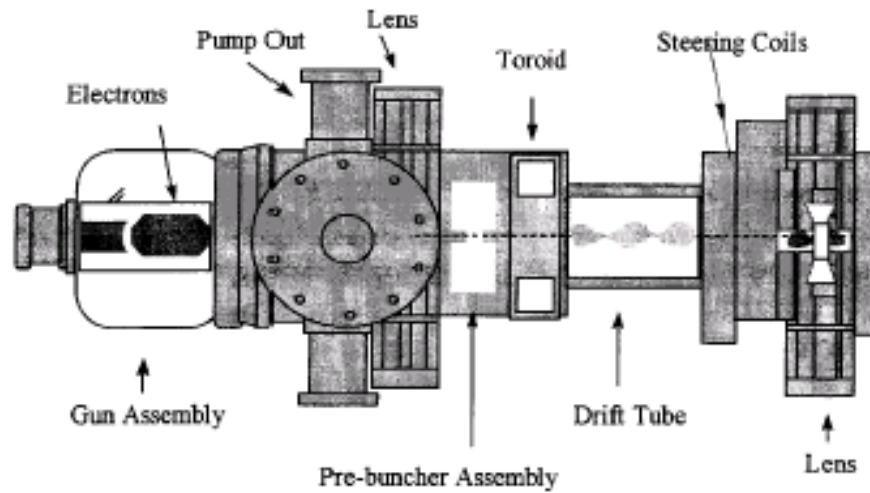


Figure 27. Beam injection system and pre-buncher assembly. [From Ref. 27 pg. 18]

C. BEAM STEERING AND FOCUSING

As the beam exits the LINAC, it passes through a deflection system consisting of a collimator, a series of steering magnets, and a spectral filter. First the beam passes through the collimator to reduce the divergence. It then passes through the first steering magnet and then the spectral filter. This allows the ability to select the desired energy electrons that were separated by the magnetic field of the first deflection magnet. After passing through the second deflection magnet, the beam is focused and placed on the desired target by the quadrapole magnets (see Figures 28 and 29).

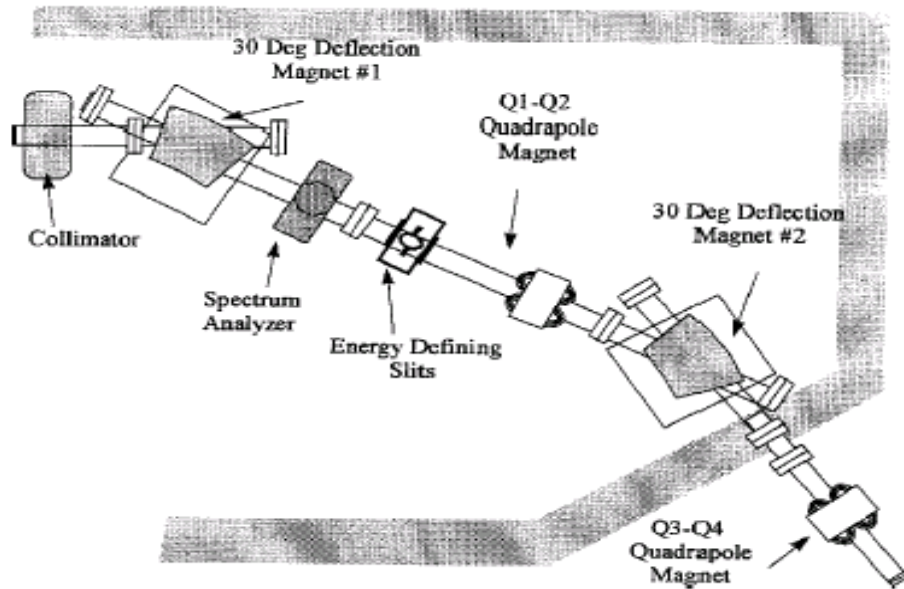


Figure 28. Deflection System. [From: Ref. 26 pg. 21]

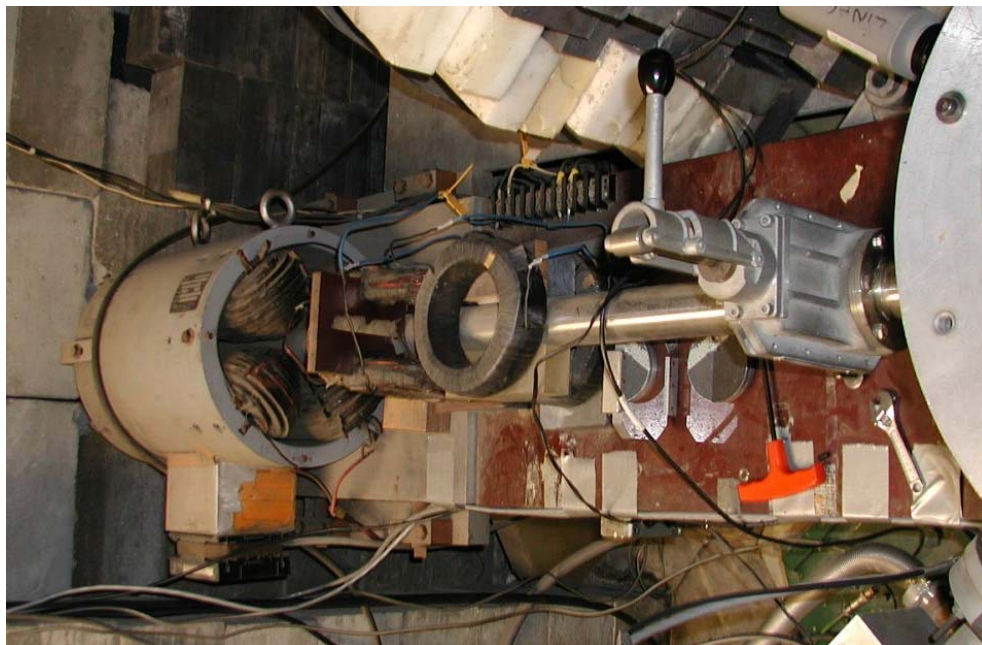


Figure 29. Quadrupole Magnets.

D. BEAM FLUENCE MEASUREMENT

As seen in Figure 30, the beam passes through a Secondary Emission Monitor (SEM) just prior to the target. The SEM measures the fluence of the beam passing through it by placing a charge on a capacitor connected in parallel with it. The voltage of the capacitor is measured by a fluttering reed voltmeter and the integrated charge is then converted to fluence. Since the fluence is proportional to the total number of electrons collected by the SEM, the fluence is then proportional to the charge on the capacitor. The charge of the capacitor is given as $Q = C V$, where Q is the total charge of the capacitor, C is the capacitance in Farads, and V is the capacitor voltage.

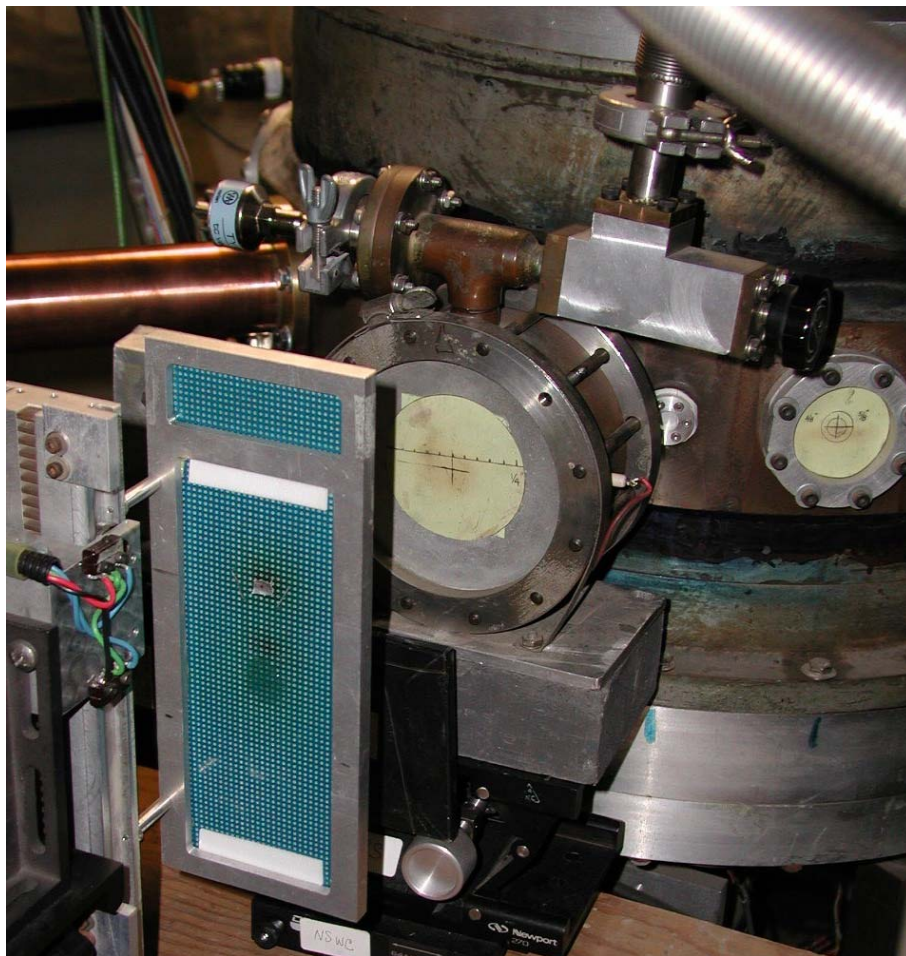


Figure 30. Secondary Emission Monitor and Cell Target Stand.

However, because the foils of the SEM are thin, the probability of electron interaction is relatively low. To effectively utilize the SEM as a tool to measure fluence, a measure of the efficiency of the SEM in interacting with the electron beam was established. In principal, this was simple. The efficiency of the SEM is simply the ratio of the SEM fluence to the total fluence. The only thing required was to accurately measure the beam fluence under the conditions needed for the experiment.

E. CALIBRATION PROCEDURE

A calibration procedure was derived by Don Snyder to accomplish this. The LINAC was operated at the desired energy of 30 MeV with the beam passing through the SEM and terminating into a device known as a Faraday Cup (Figure 31). The Faraday Cup is a device that is designed to stop electrons of the desired energy (different Faraday Cups are used for different energies), and like the SEM provides a charge transfer to a capacitor. Properly positioned, the Faraday Cup is assumed to be 100% efficient in stopping electrons.



Figure 31. 30 MeV Faraday Cup.

The SEM efficiency is then found by taking the ratio of the SEM voltage to the Faraday Cup voltage. Numerous runs are conducted to account for thermal variations and electrical transients. After several runs, the SEM efficiency was found to be approximately 7%. A short calibration run was conducted prior to irradiating the solar cells yielding the same result. Figures 32 and 33 show the arrangement for the experiment.



Figure 32. Beam path from SEM to the Faraday Cup.



Figure 33. Top view of beam path. SEM at top, Faraday Cup at bottom.

The desired units for describing the dose absorbed by solar cells in space is in terms of electrons/cm². Thus in order to take measurements at known radiation doses, a conversion was required to relate SEM voltage output to electrons passing through the target. The beam fluence Φ in units of electrons/cm² is found using the following relationship:

$$\Phi (\text{e}^-/\text{cm}^2) = C V / (0.07 q A) \quad (5.1)$$

Where:

C = Capacitance in Farads

V = Capacitor Voltage

q = electron charge (coulombs)

A = area of the beam (cm²)

VI. EXPERIMENT

A. INTRODUCTION

This experiment will provide the data necessary for a comparative analysis of radiation effects on three types of solar cells. The cells tested are Silicon, Gallium Arsenide, and Multi-Junction (GaInP₂/GaAs/Ge). To collect the data required for the analysis, electrical characteristics of the cells are measured before irradiation and after each decade of dose up to 10¹⁶ electrons/cm².

The fundamental building block of the data for this experiment is the I-V curve. These curves provide all of the parameters (either directly or indirectly) to determine the performance of the solar cell. The following discussion describes the equipment and method used to obtain the I-V curves used in this experiment.

B. RADIOLOGICAL SAFETY

Exposure to ionizing radiation is a serious matter and must be dealt with appropriately to prevent serious injury. The hazards posed by this experiment were greatly mitigated by following basic radiological handling principles such as ALARA (minimize exposure to levels As Low As Reasonably Achievable) and the concept of time/distance/shielding. A professional radiation technician supervised all runs conducted using the LINAC. During the runs, he made continuous radiation surveys to ensure that gamma and neutron radiation levels were well within safe limits. The effective use of shielding materials such as lead and poly blocks ensured that no streaming radiation sources emanated from the LINAC. Additionally, radiation surveys were conducted at the completion of each run around the test device and on the solar cells to ensure no radiation hazards were present. Free release of the cells for transport was allowed only after the cells showed no signs of activation. Pocket dosimeters and LiF film badges were worn by all personnel involved in the experiment to monitor any dose absorbed. At no time did

anyone working in or around the LINAC receive exposure to ionizing radiation above the established limits.

C. SOLAR SIMULATOR AND TEST EQUIPMENT

As discussed in Chapter III, the effects of solar cell degradation is determined by analysis of well known output parameters when placed under test. The equipment used to obtain these parameters for this experiment consists of a SS 1000 solar simulator, a programmable power supply, a thermostatically controlled cooling system, and a PC running LABVIEW software.

The SS-1000 solar simulator (Figure 34) at NPS had been recently modified with a 1500 watt Xenon bulb. This differs from the 1000-watt bulb in previous experiments. The spectral characteristics are nearly identical to the 1000-watt bulb, however the intensity and uniformity of the footprint is much improved.



Figure 34. SS-1000 Solar simulator in operation.

With proper calibration, the SS-1000 provides a very close approximation to the actual solar power intensity at AM0. To accomplish this, the beam uniformity and intensity are adjusted by means of three adjustments in the x-y-z axes of the mirror inside the simulator (see Figure 35).

To ensure a uniform intensity across the testing surface, a test cell attached to the programmable power supply is biased with 4V and allowed to pass current under short circuit conditions. By moving the cell and observing the current changes in the footprint of the lamp, the x and y adjusting screws were manipulated to obtain a homogeneous intensity level in the area that the cell was to be placed. Manipulation of the z-axis provided changes in intensity to provide the proper short circuit current as measured by the manufacturer. Once set, the x and y-axes were stable, however manipulation of the z-axis would be required periodically to account for fluctuations in lamp temperature and atmospheric changes. Additionally, because each type of cell has different spectral characteristics, the AM0 Isc was adjusted using the z-axis setting on a cell by cell basis to provide uniformity of the results with known data when available.



Figure 35. X-Y-Z focal plane adjustment settings on the SS-1000 solar simulator.

Because solar cells have a positive temperature coefficient, it is important to maintain cell temperature constant. A system is required to ensure constant temperature during each phase of the test as well as consistent for all of the phases. A dual bath cooling system with a thermocouple attached to the testing block was used for this purpose. The first bath provides a relatively large constant temperature sink used to take away the waste heat. Since this bath is large, it remains at a constant temperature for any transient that the test equipment can generate. The second bath has the fine temperature control that regulates flow of the water to maintain a temperature of 26 Celsius by thermocouple.

A brass test block specifically designed for experiments such as this was used to provide a stable platform, electrical connections, and temperature control. The block has spring-loaded fingers, which gently rest on top of the cell. These fingers and the block ground are electrically connected to the HP 6626A power supply. The connections are interchangeable to allow easy configuration change for p-n or n-p connection. A cooling tube passes through the block for the cooling system and the thermocouple is directly attached to the block. Additionally, a vacuum pump is connected to the block. The vacuum holds the cell firmly to the block through a small hole located directly under the cell under test. Figure 36 shows the test block.

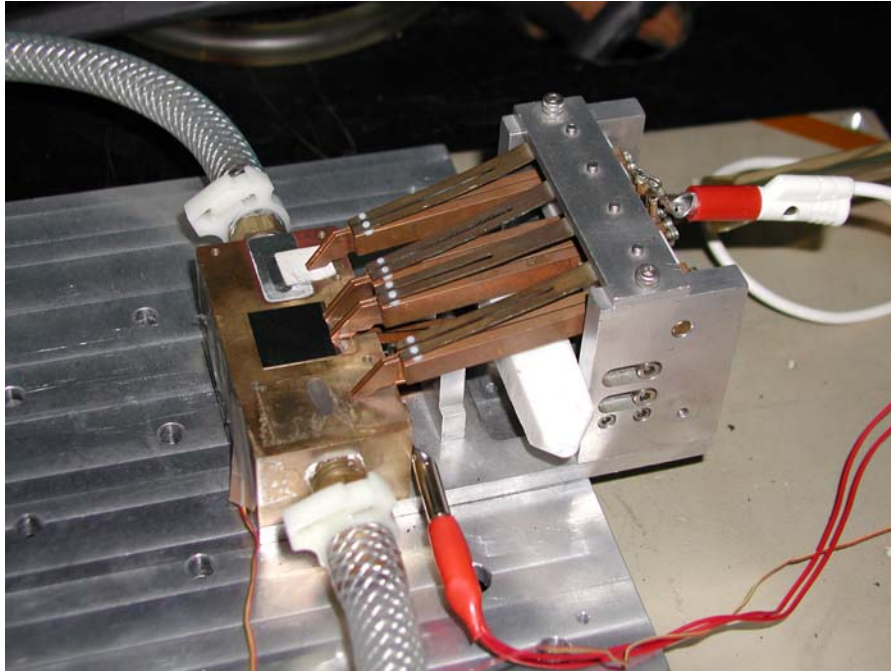


Figure 36. Test block showing electrical contacts, cooling connections and thermocouple attachment.

To obtain the I-V curve, a voltage source, current sink, and a means of sweeping the voltage is needed. This is accomplished using the HP 6626A programmable power supply and a computer running LABVIEW software. The HP 6626 power supply has four channels, two of which were used in this procedure. Channel one provides a constant 4V bias to drive current through the cell under test. The Labview software to sweep the voltage providing the I-V curve controls channel two. The sweep starts at 4 Volts to simulate short circuit current and increments at .05 V steps until open circuit conditions are met. This is determined by the user and is set at the bandgap energy of the device under test. The software then records the current from the power supply at each voltage increment and the data is recorded in text tab delimited form for import to a Microsoft Excel spreadsheet. Figure 37 shows the LABVIEW interface.

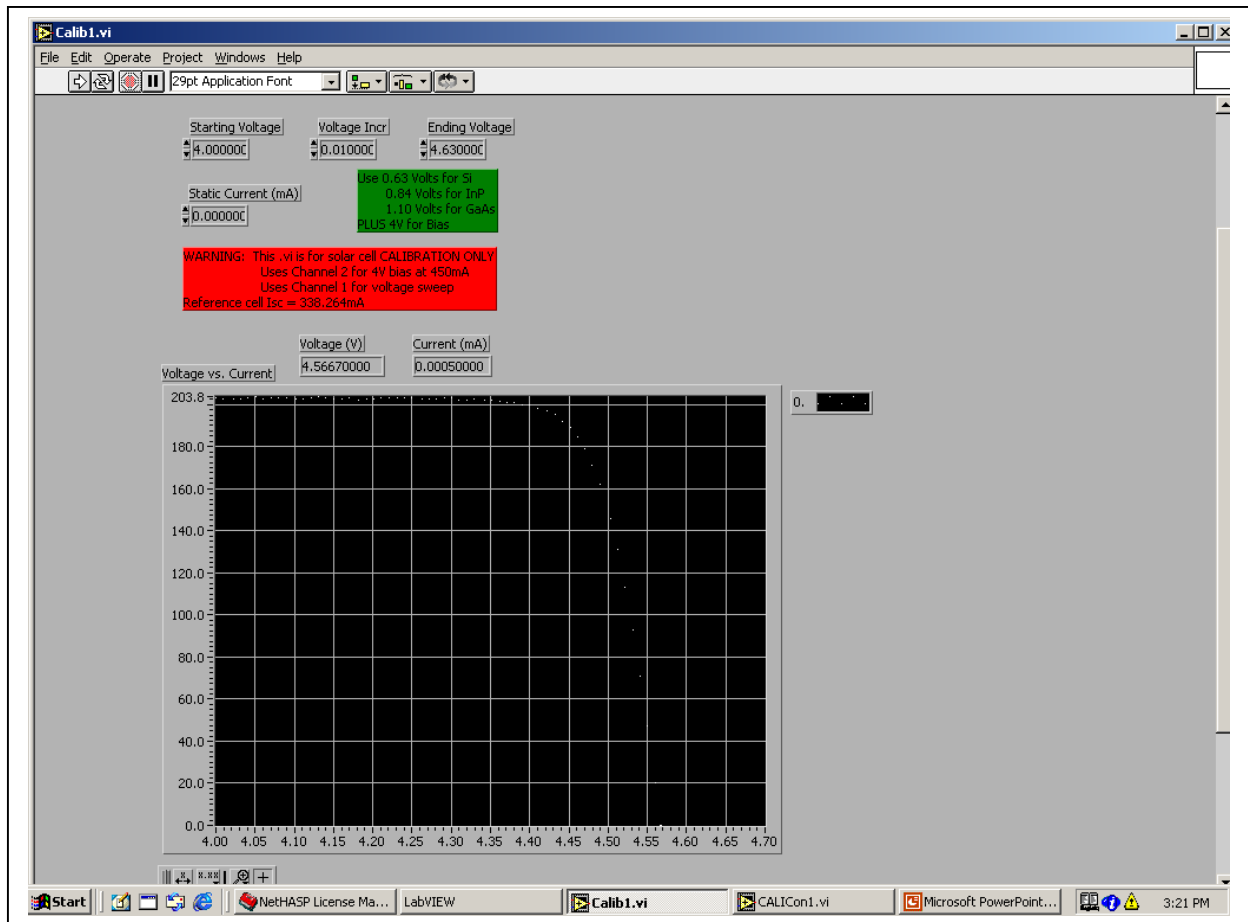


Figure 37. Capture of LABVIEW program used to obtain the I-V curves.

D. PROCEDURE

The solar cells for this experiment were chosen based upon I-V curves to ensure the cells under test would behave in a predictable manner and that there were no pre-existing flaws in the I-V curves which might skew the experiment. Five each of Si, GaAs, and triple-junction cells were selected as candidates for use. Although not all five were irradiated, it was necessary to have cells ready in case of breakage or other calamity that might delay the experiment. The BOL data for the test cells is listed in Table 4.

Cell	Voc	Isc	Pmax	FF	Efficiency
Si02	.5548	37.64	15.933	.7630	14%
GaAs22	.9974	27.22	20.883	.7727	17%
Mj08	2.5254	15.39	32.41	.8338	24%

Table 4. BOL data for test cells.

The original test plan called for irradiation of an expendable silicon cell to allow for time to gain proficiency in the process, providing a dry run so to speak. This proved valuable and prevented many errors that would have likely occurred in the actual experiment. Lessons learned in handling of the cells, placement of the beam, and reading the I-V curves were applied to subsequent runs and greatly improved the process. During this run, beam position was recorded by a frame grabber to show the gaussian distribution of the beam on target. This ensured that the beam was properly focused on the target and the distribution was uniform. Additionally, a video monitor imaged the beam and a marker was used to note the beam location on a phosphor target. This allowed ease of positioning the cell in the center of the beam without re-imaging the beam each run.

During the calibration runs conducted earlier, the electron fluence for each run was correlated to a voltage output from the SEM. Table 5 shows the voltage/fluence relationship.

Fluence	Associated SEM voltage
1 x 10¹¹	7 mV
1 x 10¹²	70 mV
1 x 10¹³	700 mV
1 x 10¹⁴	7 V
1 x 10¹⁵	70 V
1 x 10¹⁶	700 V

Table 5. Target Fluence / Voltage conversion.

The general procedure was straightforward. First, irradiate a candidate cell with the LINAC energy set at 30 MeV to a dose of 1×10^{11} electrons. Once achieved, the LINAC RF power would be removed to stop the injection of electrons, allowing the machine to remain in standby. After observing proper radiological safety precautions, the cell was removed and transported to the solar simulator. The cell would then be placed on the test block, illuminated and allowed to reach thermal equilibrium. Once equilibrium was established, the I-V curve was run three times. (The three runs were used to establish if there were any annealing effects occurring from the I-V curves.) Once the curves were recorded and saved, the cell was removed from the simulator and the process was repeated for the next desired fluence level. A slight modification to the procedure was made after analyzing the results of Si02. It was decided that the starting fluence should be raised to 1×10^{12} vice 1×10^{11} electrons. The reason for this was to save time and to minimize the risk of damage to the cells due to handling.

E. TEST RESULTS

Three cells were successfully irradiated and tested. The silicon test cell Si02 was irradiated from 1×10^{11} to 1×10^{15} electrons. Cells GaAs22 (Gallium Arsenide test cell) and Mj08 (multi-junction test cell) were irradiated from a fluence of 1×10^{12} to 1×10^{16} electrons. All tests were conducted at 30 MeV electron energy. The I-V curves taken of the test cells are indicative of those taken after irradiation with a 1 MeV source, however the extent of the damage seems greater. This is attributed to the higher energy electrons used in this experiment.

The silicon cell showed a small annealing effect after running multiple I-V curves at each fluence level, but that effect seemed to diminish after 1×10^{14} electrons. The GaAs cell did show some annealing as well, but the effects were not as prominent. The annealing effects from the tests were not evident in the multi-junction cell. It is believed that the reason for this is that the multi-junction cells seemed better hardened to the radiation. Since the damage was so minimal at doses below 1×10^{15} electrons, there was

no annealing to be seen, and the mechanism affected by the current annealing was masked by other damage not repairable by current annealing at higher doses.

A comparison of the three cells shows that the Si cell was most vulnerable to the radiation damage, followed by the GaAs and multi-junction cell respectively. The data for the three cells is located in Appendix A.

THIS PAGE INTENTIONALLY LEFT BLANK

VII. CONCLUSIONS

In this experiment, three solar cells of different construction were irradiated with 30 MeV electrons to incremental fluence levels up to 1×10^{16} electrons. The purpose of this was to analyze their performance characteristics and conduct a comparative analysis. Additionally, the I-V curves were run several times on each cell after each exposure to determine if any annealing effects were observable.

Figure 39 is a composite plot of the three test cell efficiencies as a function of electron fluence. In general, the silicon cell displayed the greatest sensitivity to the effects of radiation damage. This was expected since GaAs and multi-junction cells are naturally more radiation hardened due to their absorption cross-sections and lattice structure properties. Unlike the GaAs and multi-junction cells, cell efficiency dropped earlier in the radiation process. This is evident in the I-V curve composite diagrams for the three cells also. Efficiencies in the GaAs and multi-junction cells appear unchanged until nearly 1×10^{13} electrons. However it appears that after that point, the multi-junction cell drops faster in efficiency than does the GaAs. Perhaps it is attributable to the Germanium substrate of the multi-junction cell. This may be a point worthy of further research.

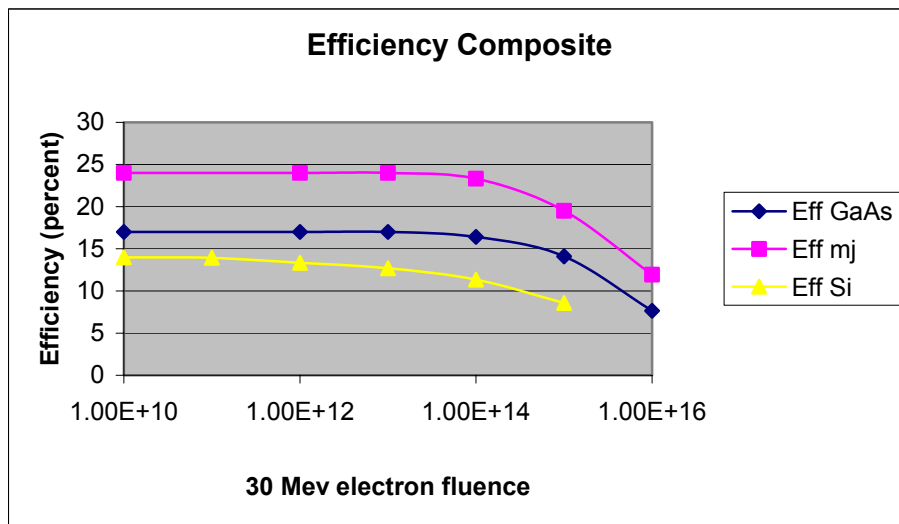


Figure 38. Cell efficiency plot versus 30 MeV electron fluence for all three test cells.

The Fill Factor (FF) of the curves provides an indication of the performance of the cells at each stage of irradiation. As discussed in chapter three, FF compares the performance of the cell by measuring the ratio of actual area under the I-V curve with that of one made curve with a rectangle made from the Voc and Isc parameters. Comparison of the fill factor degradation with respect to irradiation showed that the silicon cell Si02 was less affected than the Gallium Arsenide and multi-junction cells. The multi-junction cell FF suffered most. The results show that the cells were affected by different damage mechanisms or combination of mechanisms. The fact that the silicon cell was least affected is partly due to the fact that the FF of silicon is not as good as that of GaAs and the triple junction cell to begin with. The interesting thing that the data provides is that there is a noticeable degradation in the other cells. This is an important design consideration and has a significant impact on the mean mission duration of spacecraft utilizing these solar cells. Further research is recommended to investigate the actual damage mechanisms involved and ways to mitigate them.

Comparison of the short circuit current (Isc) of the three cells yielded an interesting result (see Figure 39). The GaAs and triple-junction cells had relatively constant Isc until about 1×10^{14} electrons. However, the Isc in silicon dropped nearly linearly throughout the exposures. This comparison effectively shows the utility of the GaAs and triple junction cell from the power budget standpoint. Due to the rapid and nearly continuous failure of the silicon cell current, a significantly larger silicon cell must be used to ensure power requirements are met at the mid life point of the spacecraft, let alone EOL requirements. The near constant Isc of the GaAs and triple-junction cells help to even out the cell efficiency for the life of the spacecraft out to 1×10^{14} electrons.

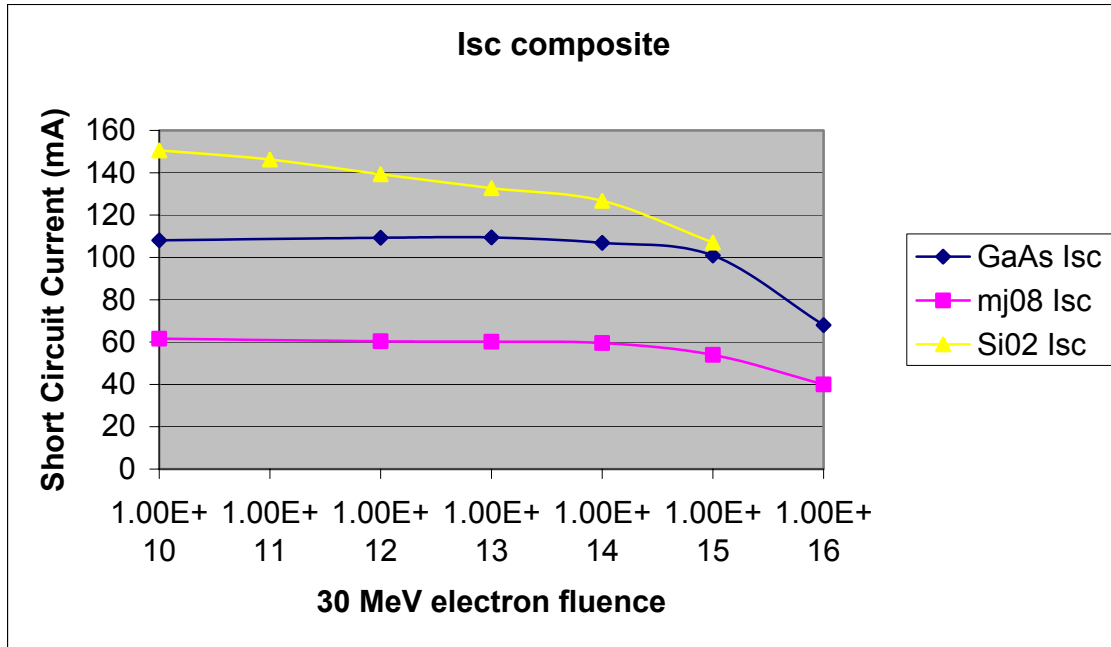


Figure 39. Short circuit current (Isc) plot versus 30 MeV electron fluence for all three test cells.

The radiation effect on open circuit voltage (Figure 40) followed a predictable behavior and yielded little meaningful information. However, it is worthy of note that unlike the case of Isc where the GaAs cell had the larger degradation, the triple junction cell had the greatest change in Voc. This again touches on the fact that the damage mechanism is different for each cell.

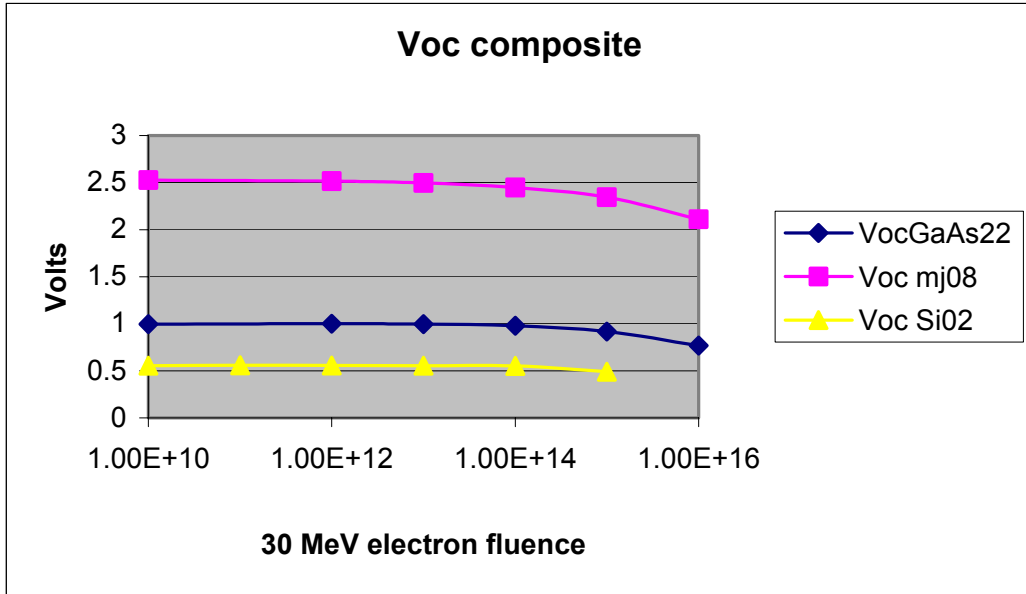


Figure 40. Open circuit voltage (Voc) plot versus 30 MeV electron fluence for all three test cells.

Comparison of the maximum power point (P_{max}) shows that the triple junction cell had the greatest change in performance due to irradiation closely followed by the GaAs cell. This was counter-intuitive after looking at the I_{sc} values, which showed the GaAs cell having the greater current degradation, and the Voc data did not seem to provide much insight or predictive value. The key to the P_{max} value is in the V_{max} value. The comparison of V_{max} across the three cells shows that the triple junction cell V_{max} falls faster than does the GaAs cell as evidenced by the convergent curves. Additionally, the triple junction V_{max} has twice the magnitude of the GaAs voltage, thus it dominates the behavior greatly. Figure 41 contains the composite plots of P_{max} , I_{max} , and V_{max} as a function of electron fluence.

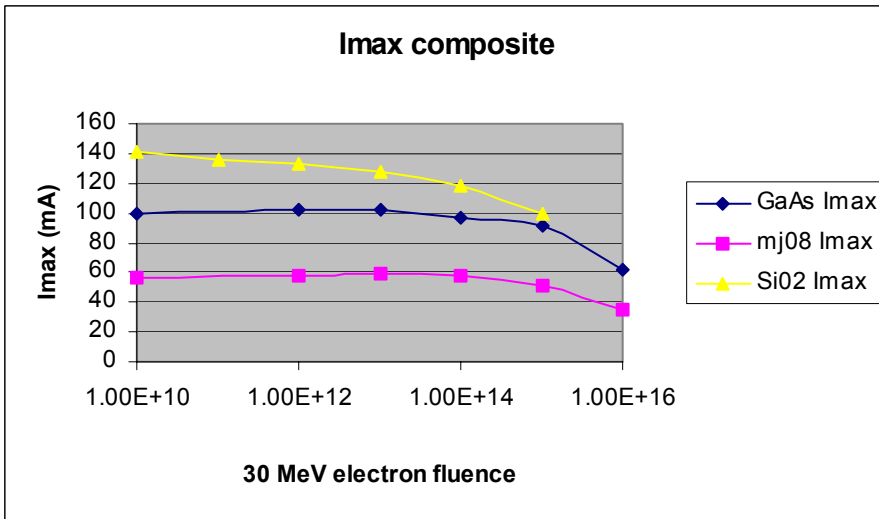
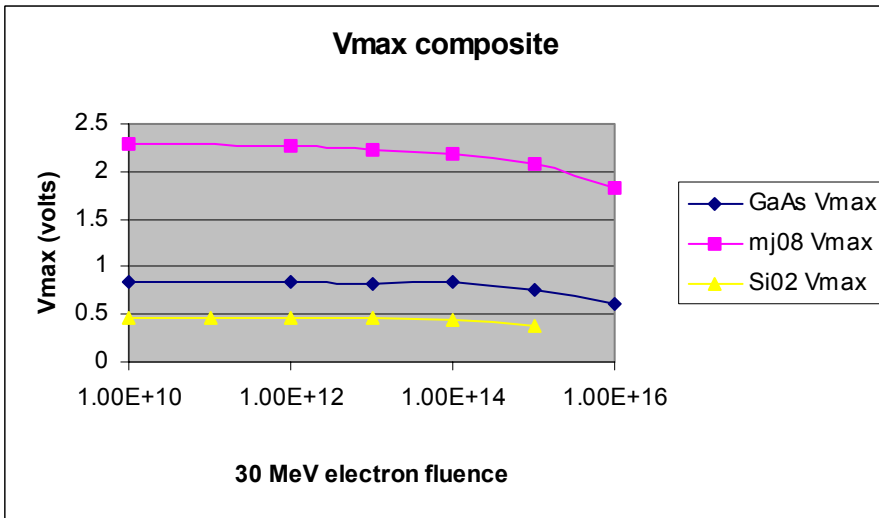
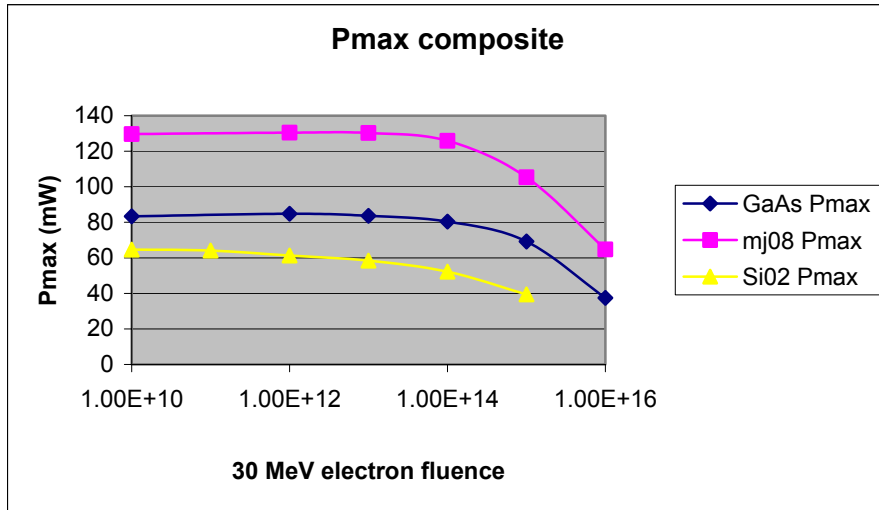


Figure 41. Composite diagrams of Pmax, Vmax and Imax for all three test cells.

The I-V curves for each cell were run three times at each fluence increment to determine if any current annealing effects were noticed. A parameter called the current performance ratio ($1 - [I_{sc1}/I_{sc2}]$) was defined in order to measure the increase in current from the annealing effect. The current annealing in the silicon cell was most noticeable. At a fluence of 1×10^{11} electrons, annealing from running the I-V curve yielded an increase of 3.1 percent in I_{sc} . At 1×10^{12} electrons, the gain in I_{sc} due to annealing was 5.4 percent. A further gain of 6.7 percent was noticed at a fluence of 1×10^{13} electrons. After this amount of irradiation, the annealing gain in I_{sc} degraded and was less than 1% at 1×10^{15} electrons. These results are promising. The actual gain in I_{sc} was not as significant as the ease in which it was done. If solar cells can be run at I_{sc} for short periods on orbit, a small but ongoing annealing process may in fact increase the life of current spacecraft utilizing silicon solar cells. Plots of the Current Performance Ratios as a function of cell voltage are contained in Figure 42.

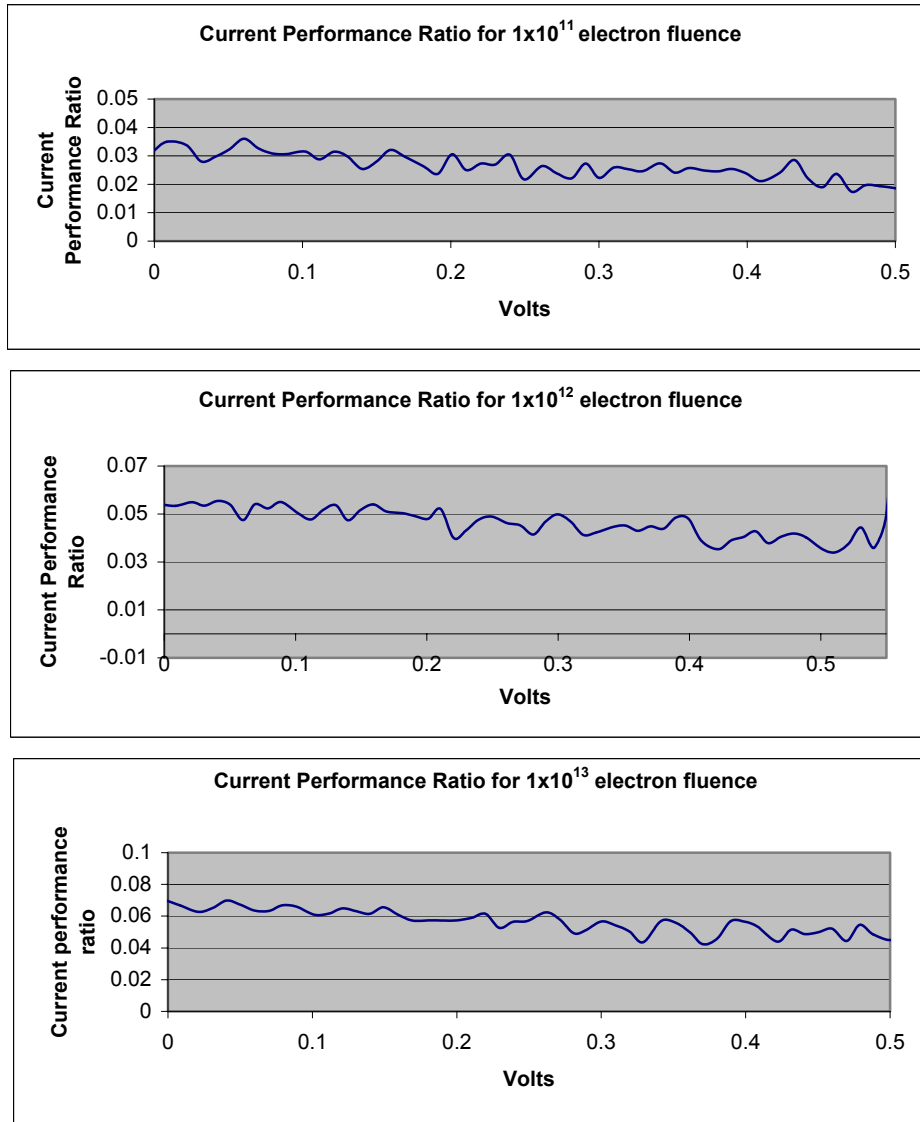


Figure 42. Current Performance Ratios of cell Si02

The scope of this thesis was to conduct a surface level comparison of the effects of radiation on three different types of solar cells. The data and analysis has provided motivation for further research in several areas brought to light by this study. It is highly recommended that further research be conducted in the areas mentioned previously. Particular attention should be given to the benefits of current annealing as seen in this study.

THIS PAGE INTENTIONALLY LEFT BLANK

LIST OF REFERENCES

1. Tada H.Y., Carter J.R, Anspaugh B.E, & Downing R.G, "Solar Cell Radiation Handbook", 3rd Edition, JPL Publ. 82-69 (1982).
2. O. Heinz, R.C. Olsen, "Introduction to the Space Environment", Naval Postgraduate School Course Notes for PH 2514, Monterey, CA, (2000).
3. S. Michael, "Space Power and Radiation Effects", Naval Postgraduate School course notes for EC 3230, Monterey, CA (2002).
4. Tipler, P.A, "Modern Physics", Worth Publishers Inc., New York, NY, 1978.
5. McKelvey, J.P., "Solid State and Semiconductor Physics", Harper & Row, New York, N.Y., (1966).
6. Sears, F.W., "University Physics", Addison-Wesley Publishing Co., Menlo Park, CA, (1982).
7. B.E.Anspaugh, "GaAs Solar Cell Radiation Handbook", JPL Publ. 96-9 (1996).
8. Pinzon D., "Analysis of Radiation Damaged and Annealed Gallium Arsenide and Indium Phosphide Solar Cells Using Deep Level Transient Spectroscopy Techniques", Master's Thesis, Naval Postgraduate School, Monterey, CA (March 1991).
9. Larin, F. "Radiation Effects in Semiconductor Devices", John Wiley & Sons Inc. New York, NY, (1968).
10. Pierret R.F., "Semiconductor Device Fundamentals", Addison-Wesley Publishing Company Inc., New York, NY, 1996.
11. Giancoli D., "General Physics", Prentice Hall, Englewood Cliffs, New Jersey, 1984.
12. Chase C., "Annealing of Defect Sites in Radiation Damaged Indium Phosphide Solar Cells Through Laser Illumination", Master's Thesis, Naval Postgraduate School, Monterey, CA, Dec 1995.
13. Streetman, B., "Solid State Electronic Devices", 2nd Ed., Prentice-Hall Inc., Englewood Cliffs, NJ, 1980.
14. Till, W.C., "Integrated Circuits: Materials, Devices, and Fabrication", Prentice-Hall, Englewood Cliffs, NJ, 1982.

15. Rudie, N.J., "Principles and Techniques of Radiation Hardening", Vol. 3 & 4, Western Periodicals Co., North Hollywood, CA, 1986.
16. Lewis, B., "Dark Current Analysis and Computer Simulation of Triple-Junction Solar Cells", Master's Thesis, Naval Postgraduate School, Monterey, CA, December 1999.
17. Fahrenbruch, A.L., Bube, R.H., "Fundamentals of Solar Cells: Photovoltaic Solar Energy Conversion", Academic Press, Newyork, NY, 1983.
18. Kramer, R.D., "Annealing of Radiation Damaged Gallium Arsenide Solar Cells by Laser Illumination", Master's Thesis, Naval Postgraduate School, Monterey, CA, September 1994.
19. Sze, S.M., "Physics of Semiconductor Devices", 2nd Ed., New York, NY, 1981.
20. Agui, T., Takamoto, T. Ikeda, E., Kurita, H., "High Efficiency Dual-Junction InGaP/GaAs Solar Cells with Improved Tunnel Junction Interconnect," Proceedings of the 10th International Conference on Indium Phosphide and Related Materials, May 1998.
21. Chiang Mi University, "LINAC Basics,"
[<http://www.fnrf.science.cmu.ac.th/theory/linac%20%Basic%20Concepts.html>]
May 2001.
22. Barnet, M.T. and Cunneen, W.J., "Design and Performance of the Electron Linear Accelerator at the U.S. Naval Postgraduate School," Master's Thesis, Naval Postgraduate School, Monterey, CA, May 1966.
23. Foley, J.K., "30 MeV Electron Beam Irradiation Effects on GaAs LED's," Master's Thesis, Naval Postgraduate School, Monterey, CA, June 1985.
24. Wertz, J., Larson, W. "Space Mission Analysis and Design" 3rd Ed. Microcosm Press; El Segundo Ca, Kluwer Academic Publishers; Dordecht, Boston, London, 1999.
25. Rasmussen, R.D., "Spacecraft Electronics Desognfor Radiation Tolerance," Proc. IEEE vol. 76, pp. 1423-1442, Nov. 1998.
26. Brittain, D.R., "Total dose radiation effects on hardened SOI bipolar transistors using the NPS LINAC," Master's Thesis, Naval Postgraduate School, Monterey, Ca, March, 1995.
27. Fifer, Tommy, L., "Radiation effects on multi-junction solar cells," Master's Thesis, Naval Postgraduate School, Monterey, CA, December 2001.

28. Philips, C.S.G., Williams, R.J.P., "Inorganic Chemistry: Principles and Non-Metals," Oxford University Press, New York, 1965.

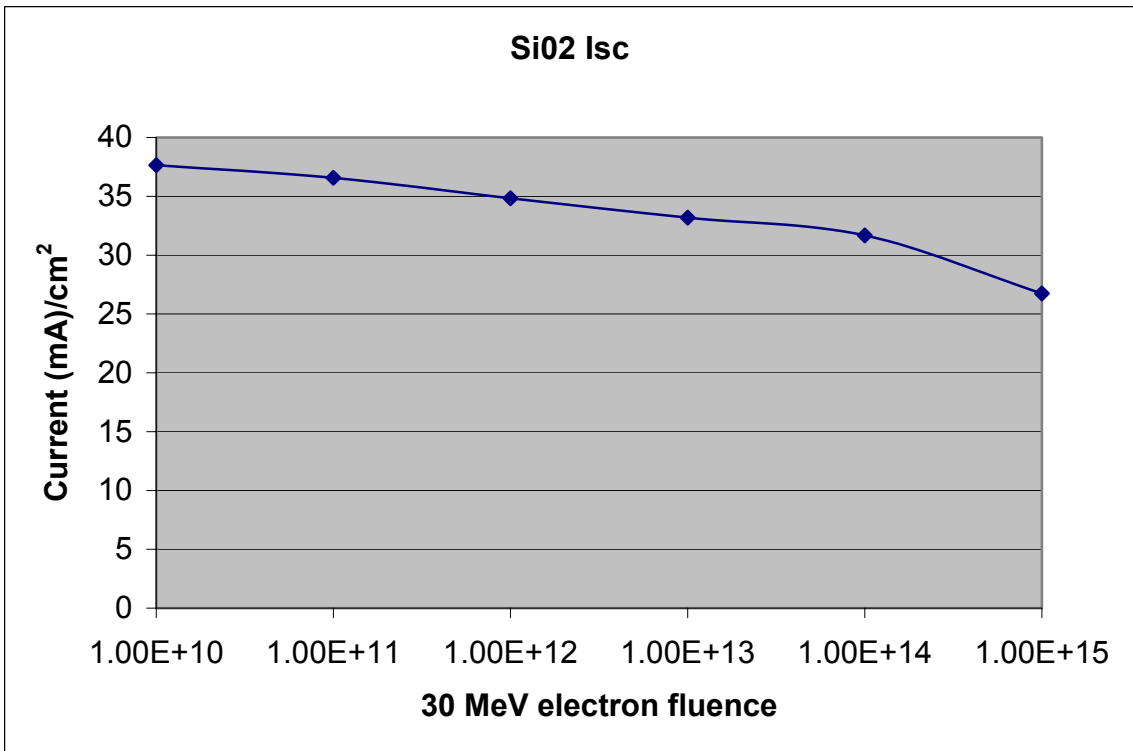
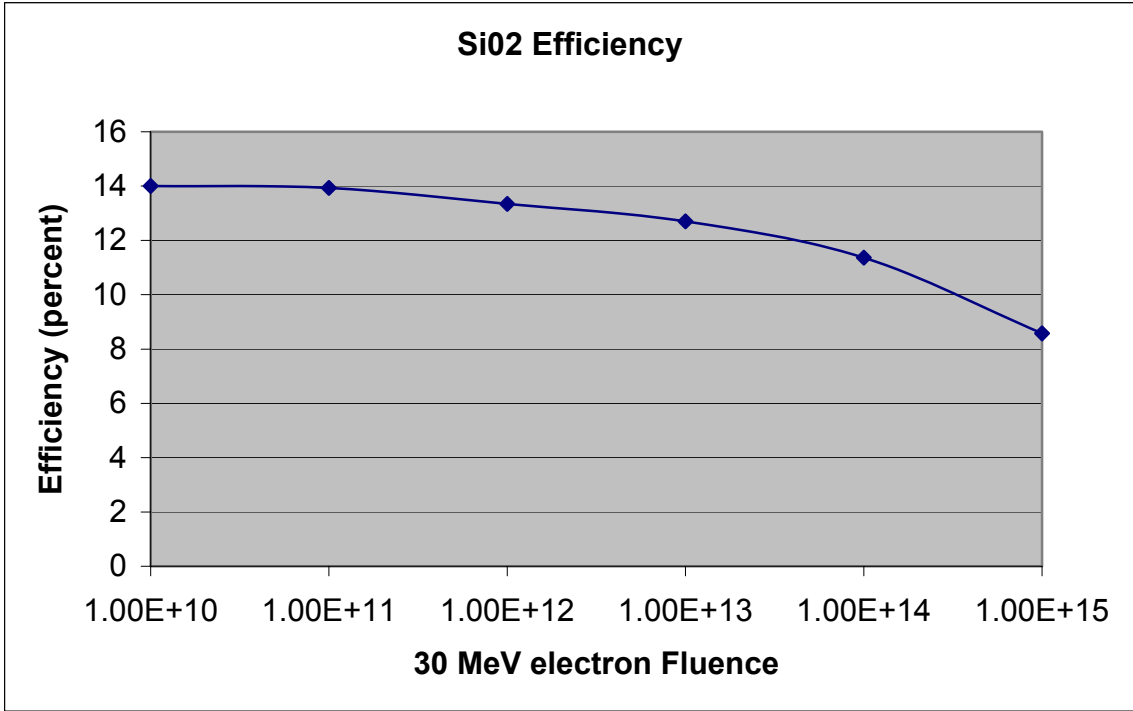
29. Guochang Li, Guohua Li, J. F. Neumark, "Investigation on ZnSe for ZnSe/GaAs/Ge High Efficiency Solar Cells," IEEE Trans 11th QUANTSOL March 14-19, 1999, Wildhaus, Switzerland.

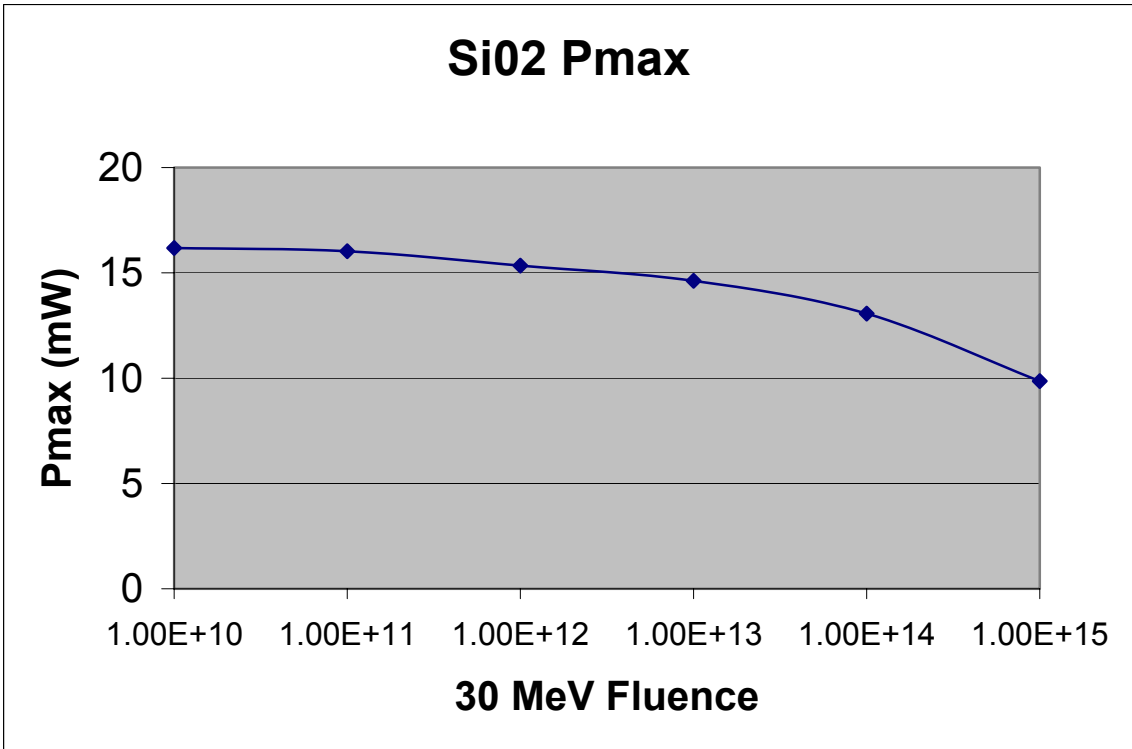
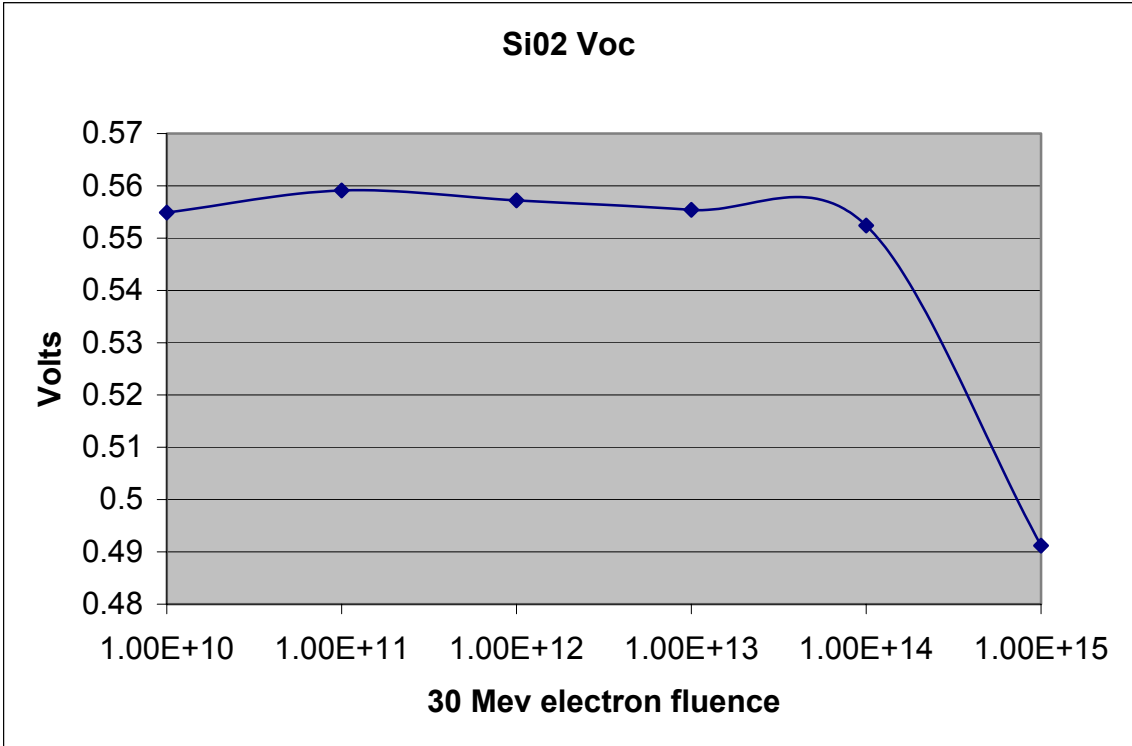
30. G. Wolfbauer, "The Electrochemistry of Dye Sensitized Solar Cells, their Sensitizers and their Redox Shuttle," PhD Thesis, Monash University 1999.

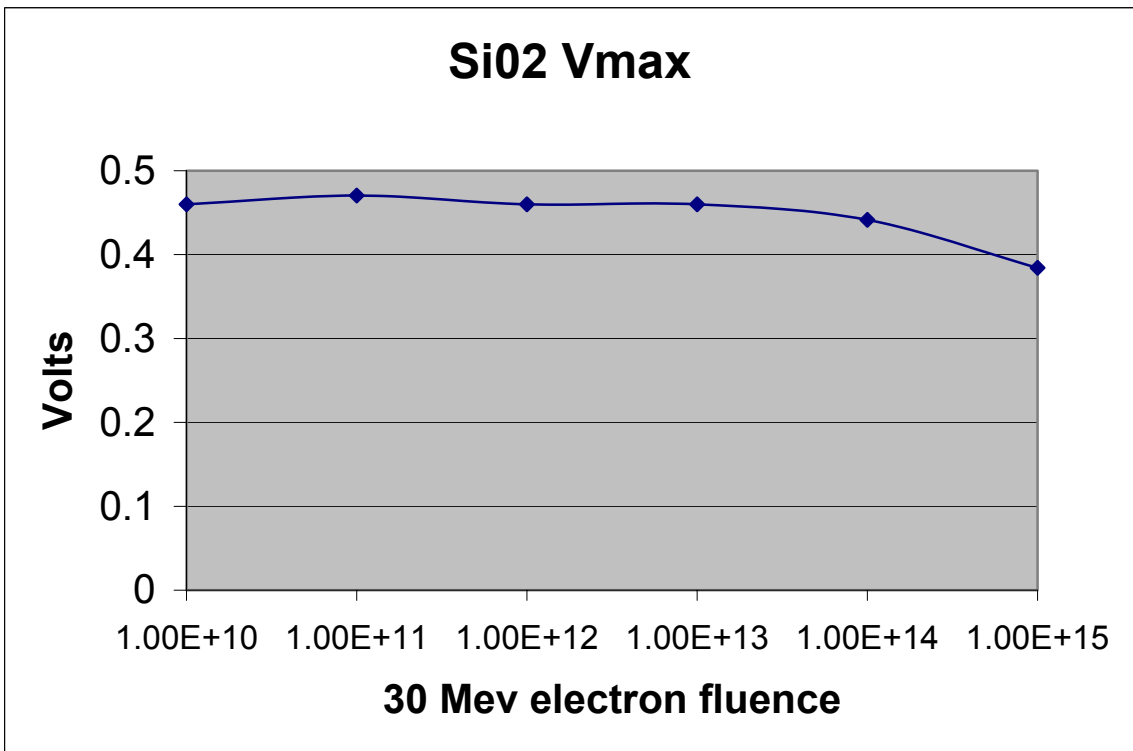
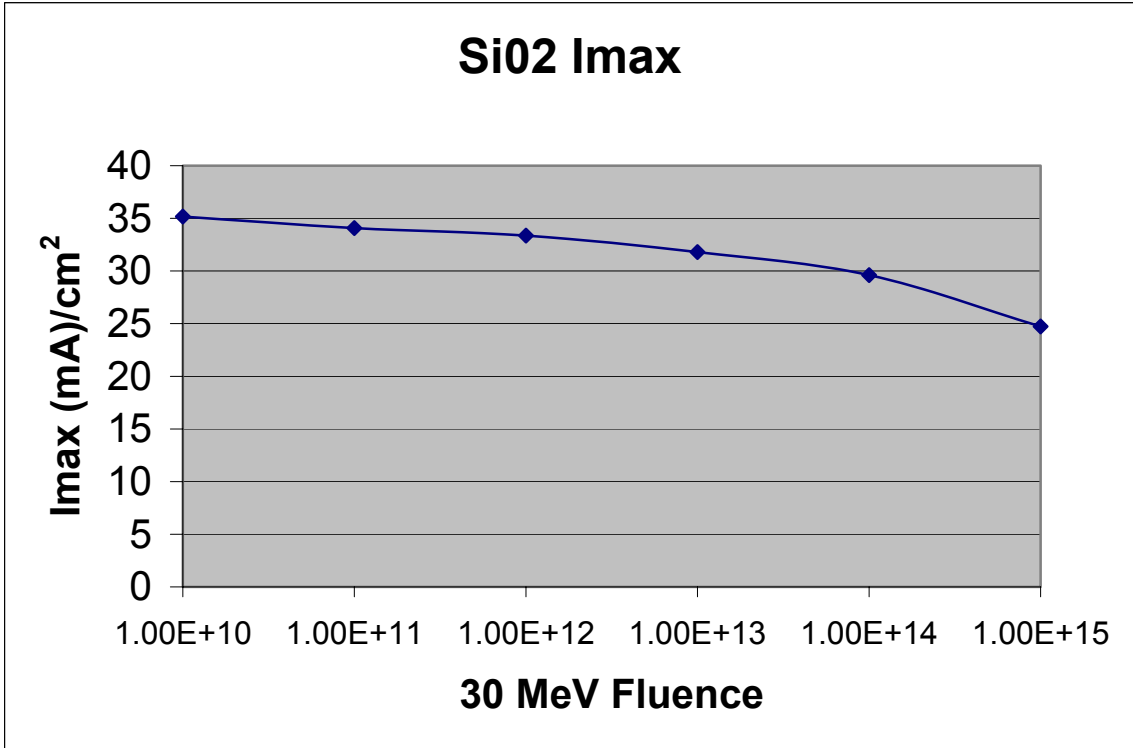
THIS PAGE INTENTIONALLY LEFT BLANK

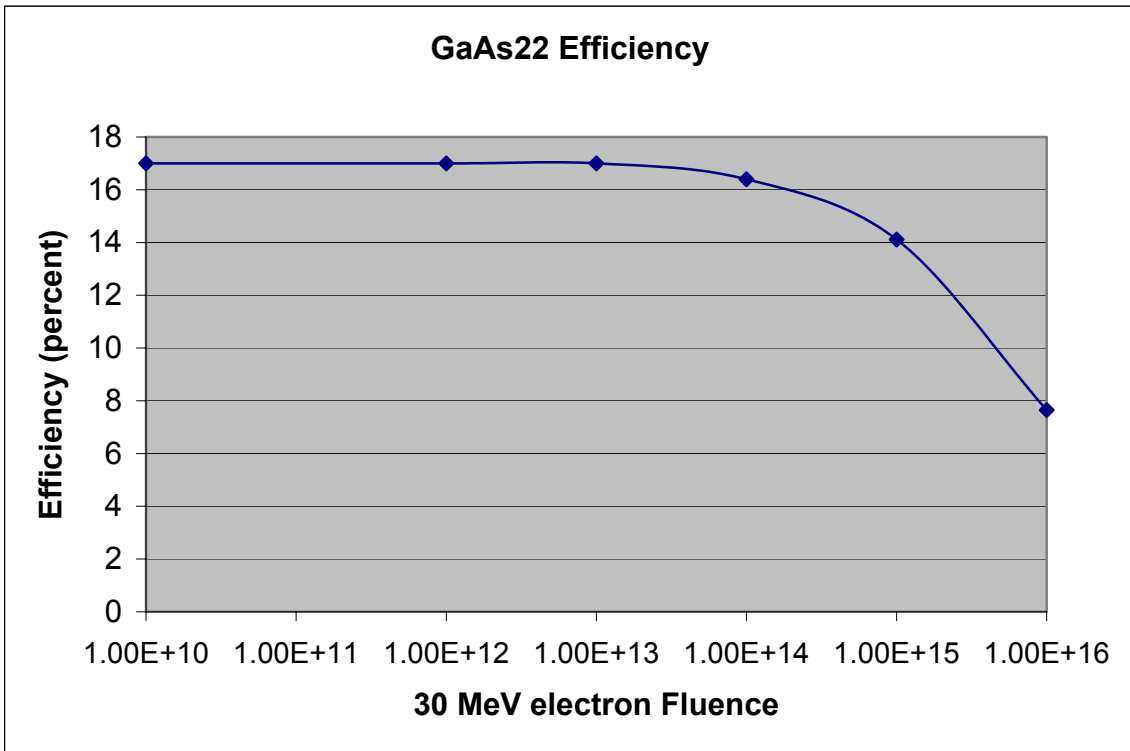
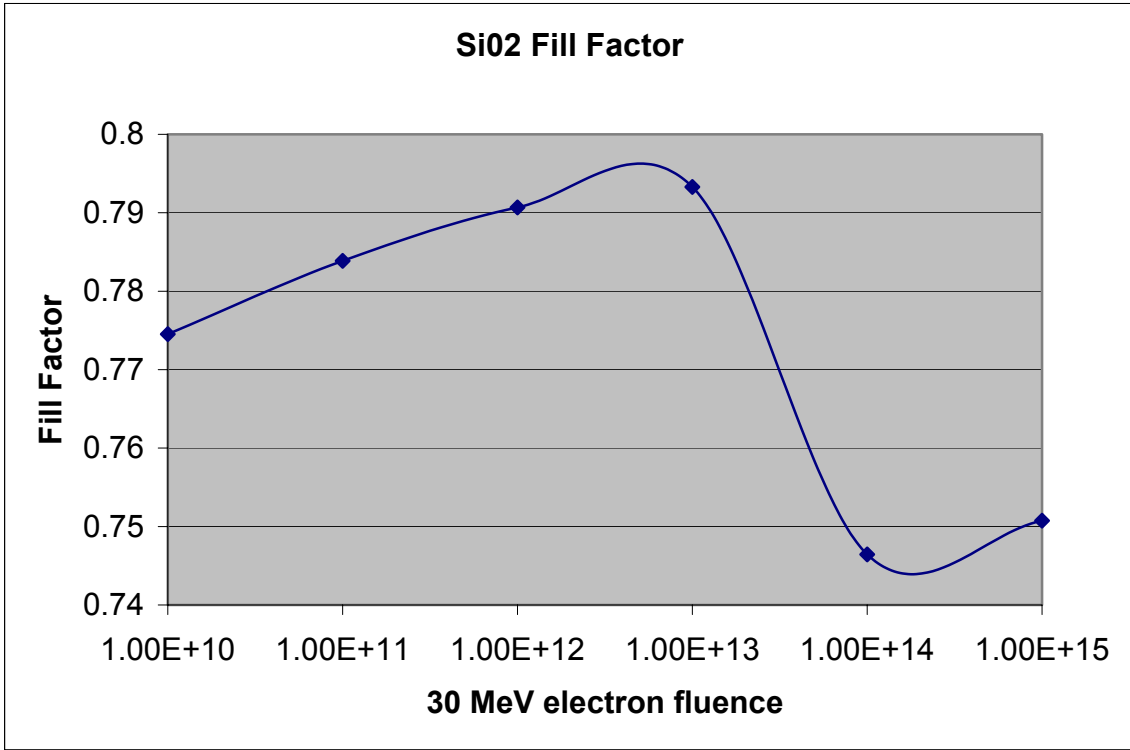
APPENDIX A

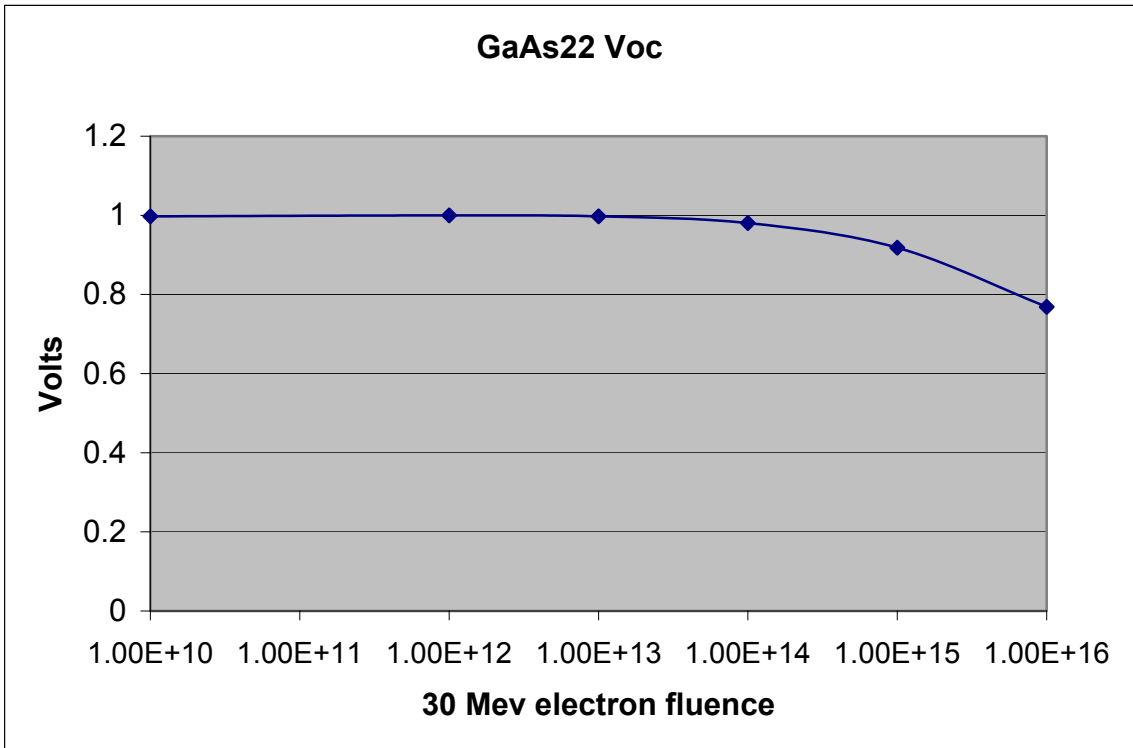
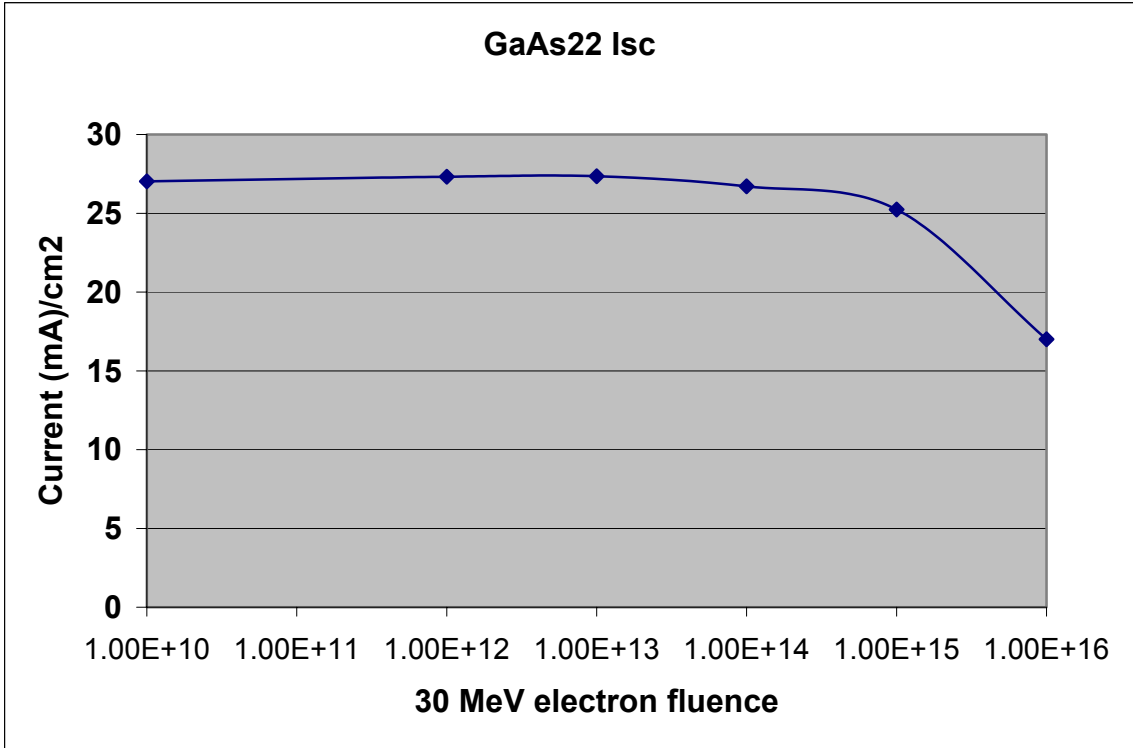
PLOTS OF SI02, GaAs22, AND MJ08 CELL PARAMETERS

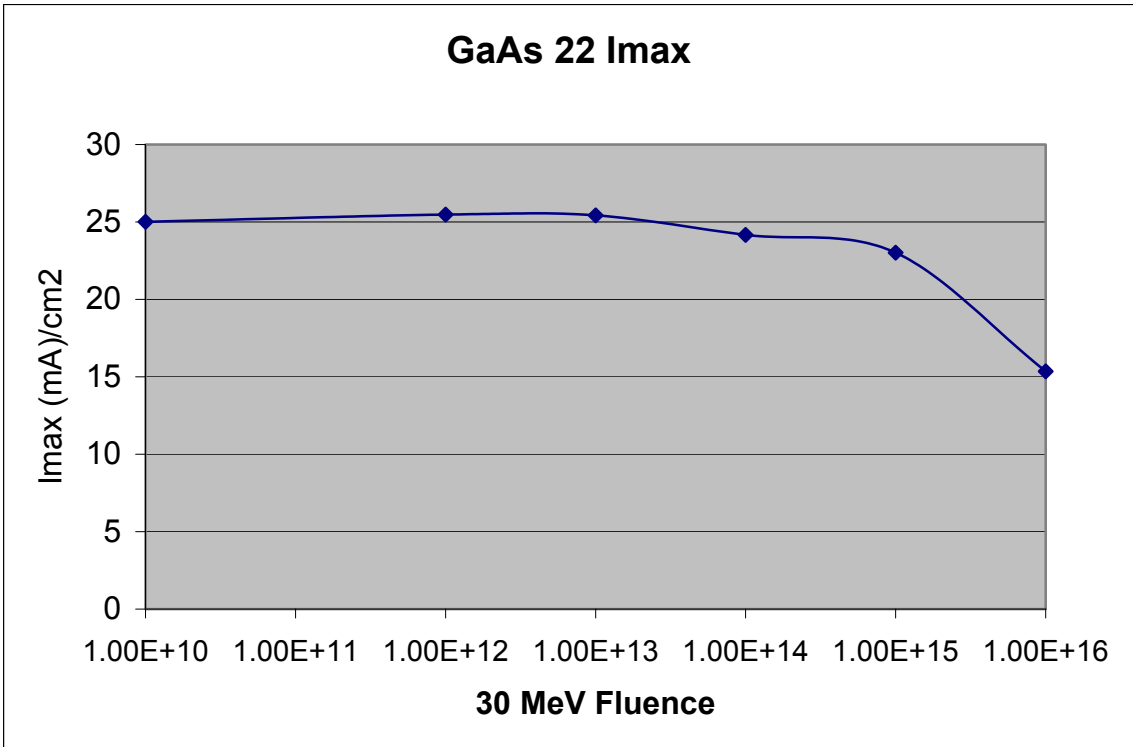
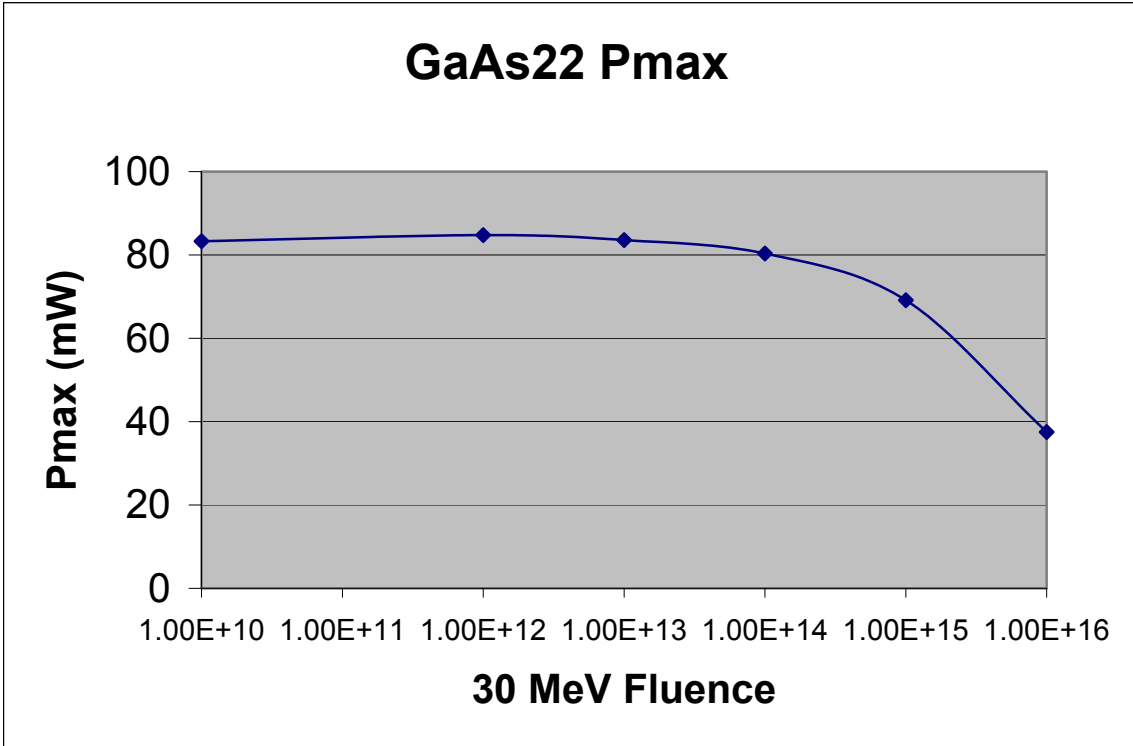


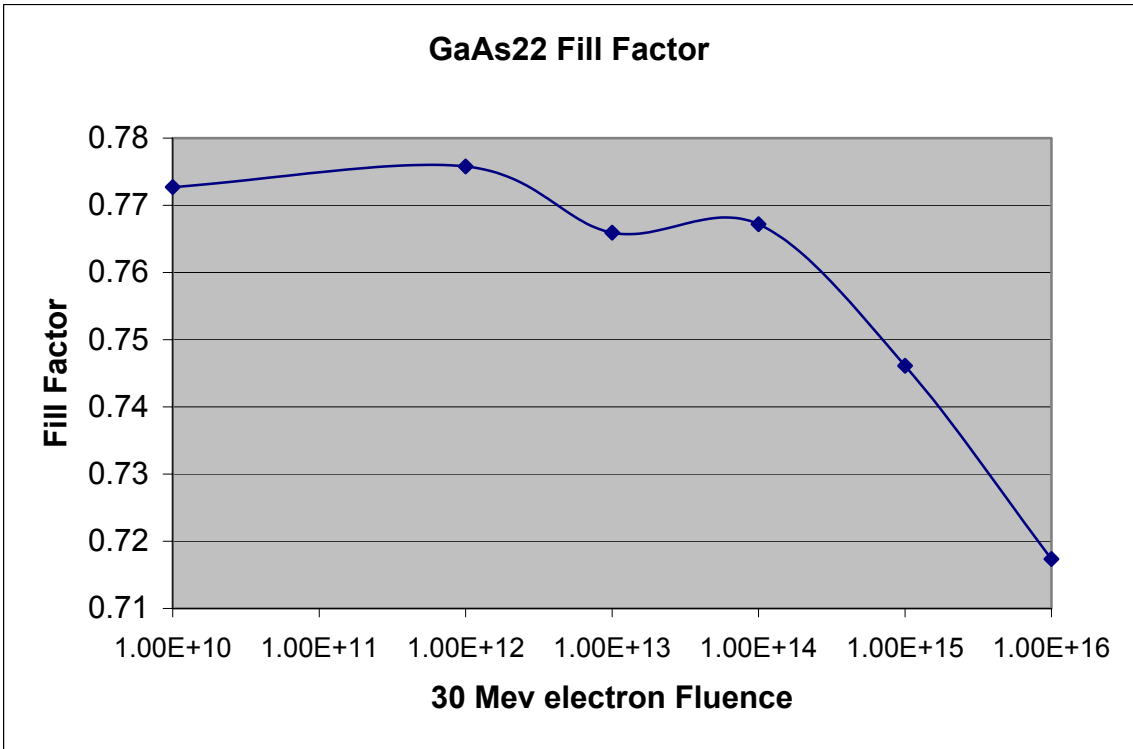
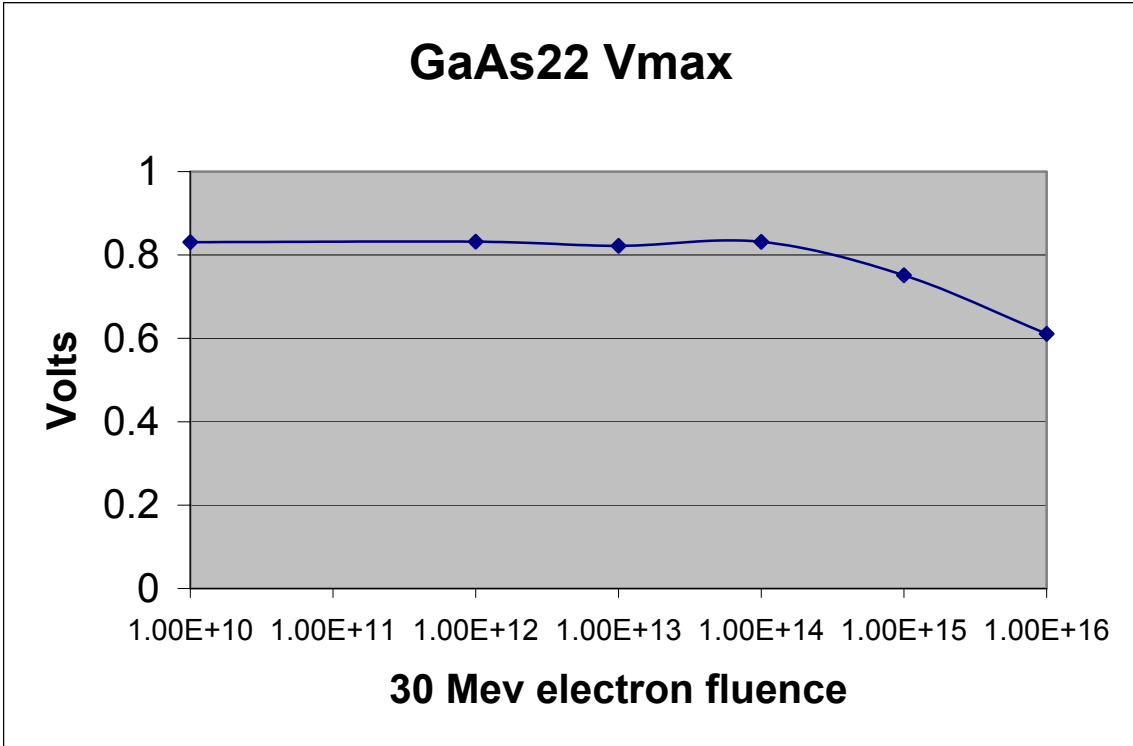


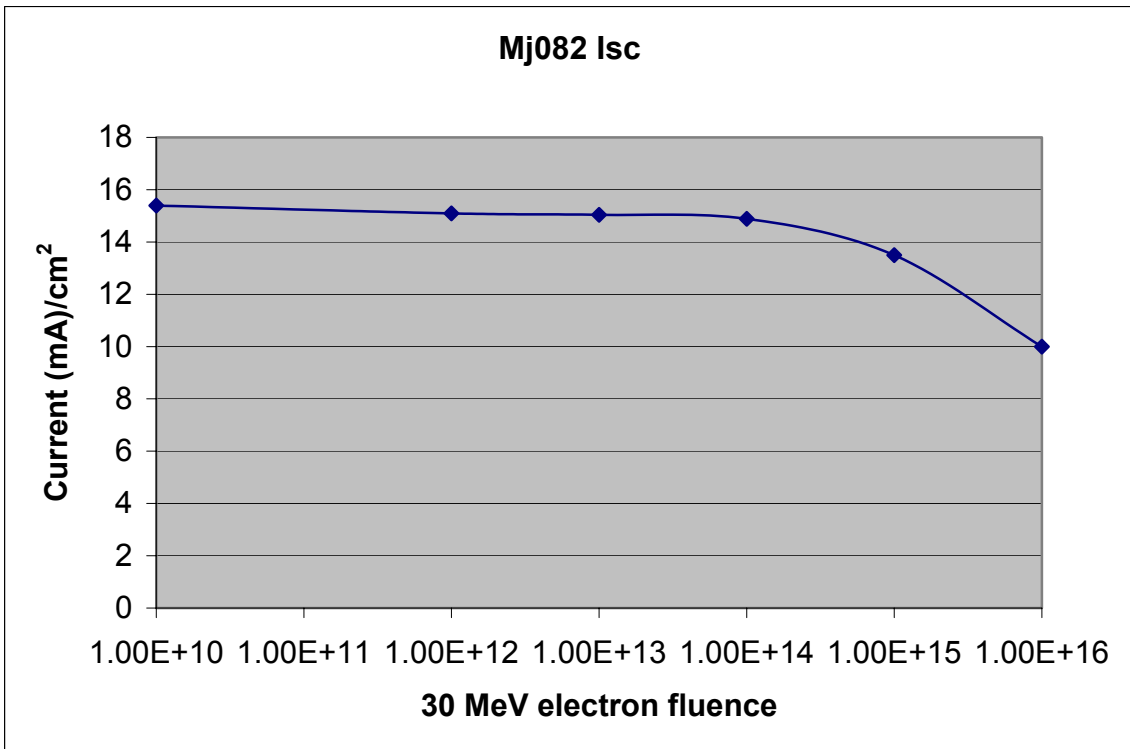
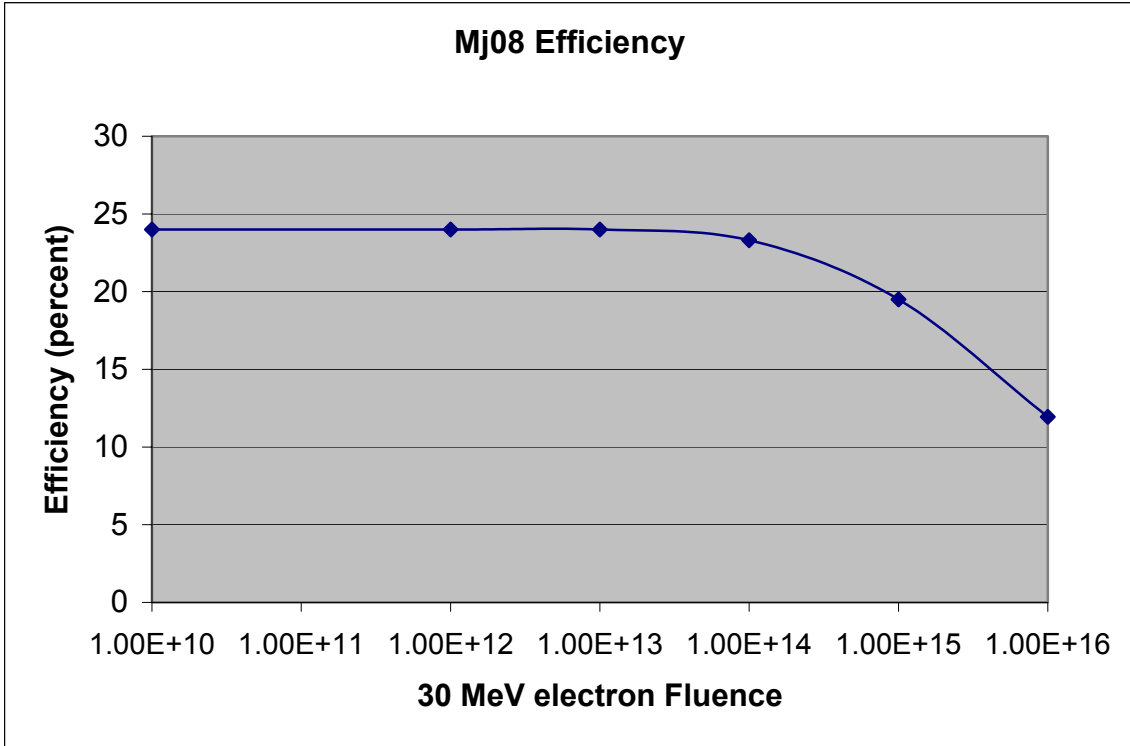


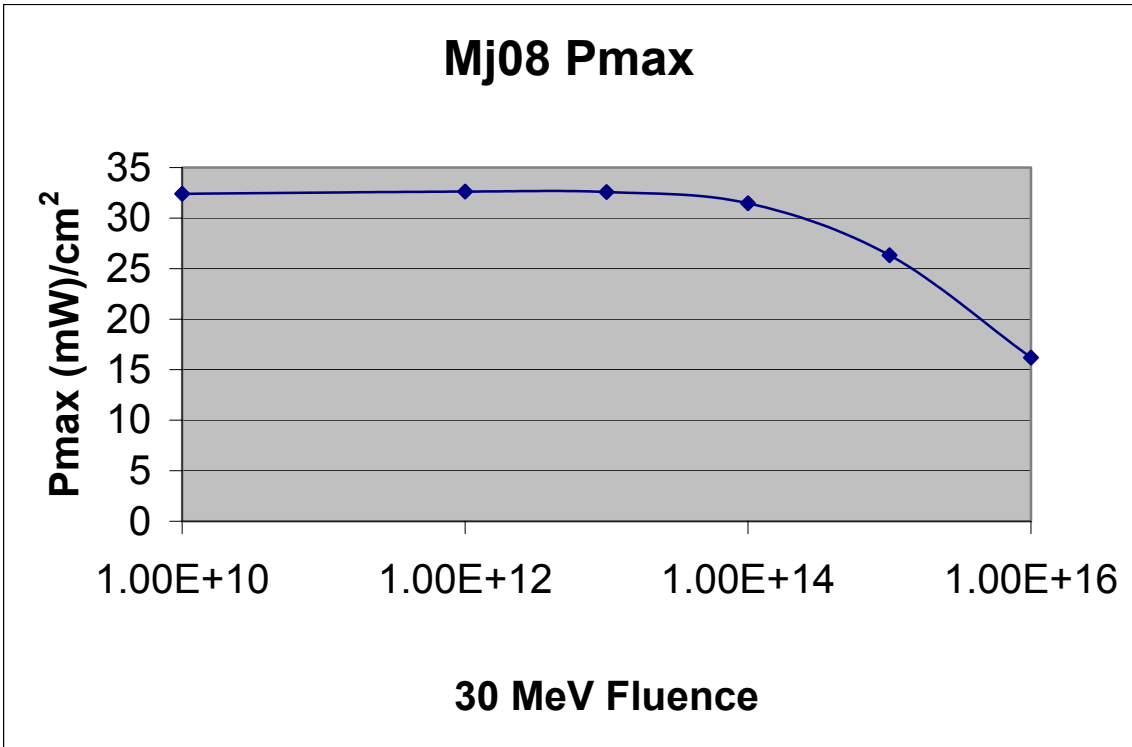
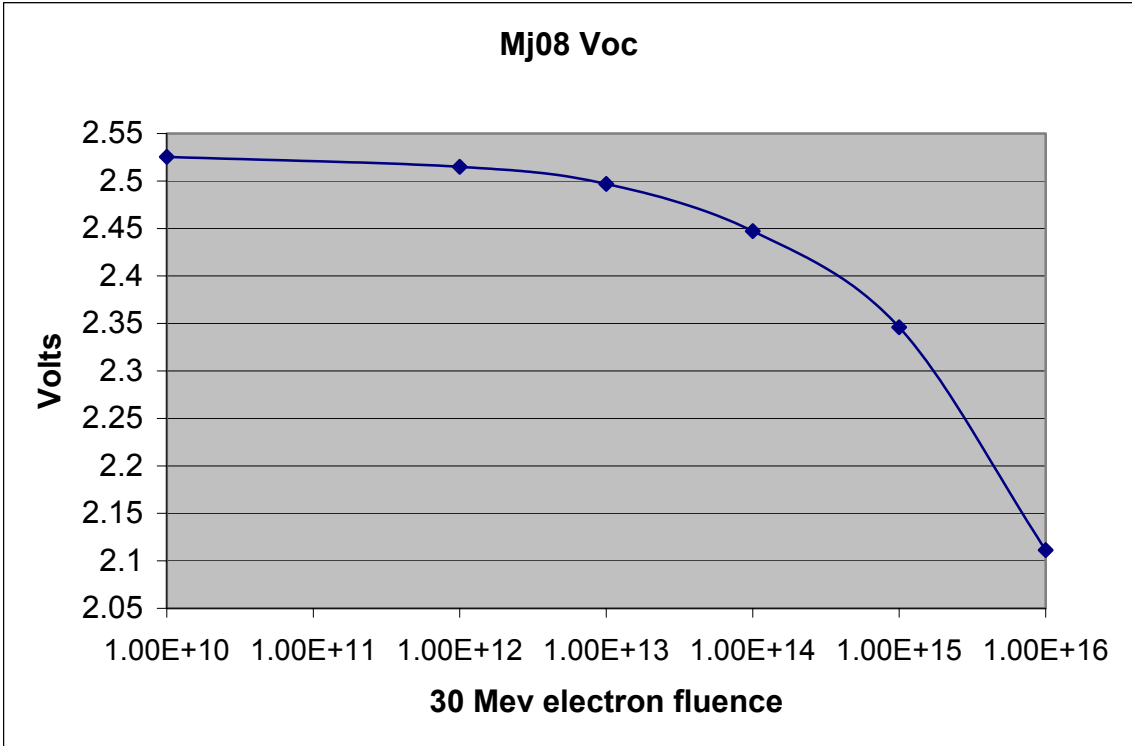


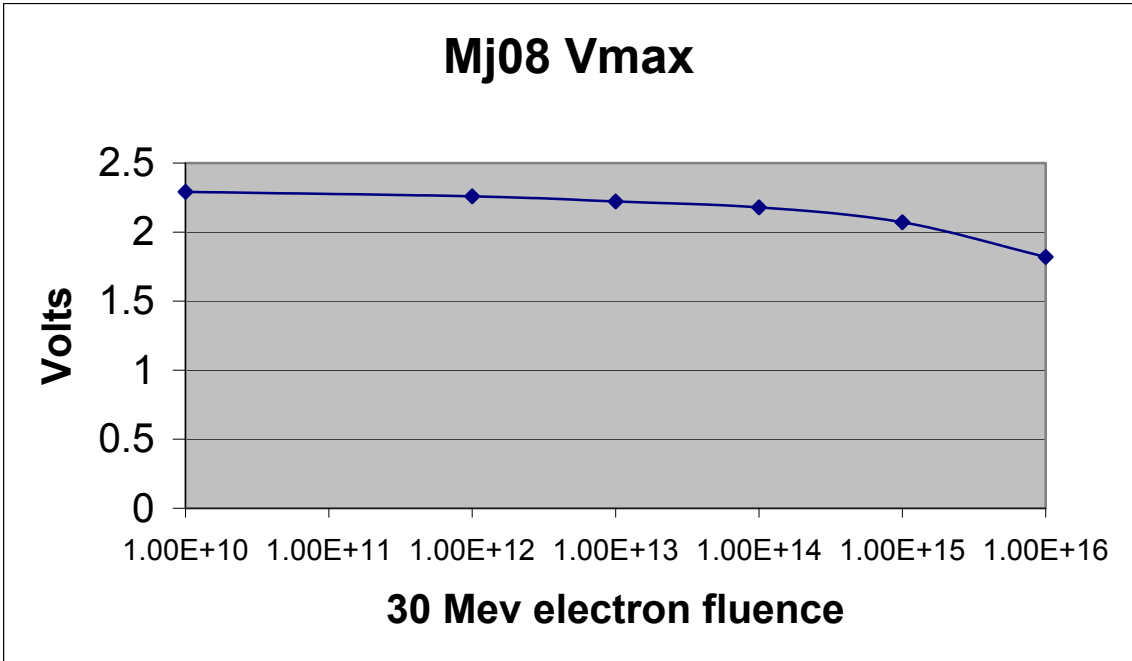
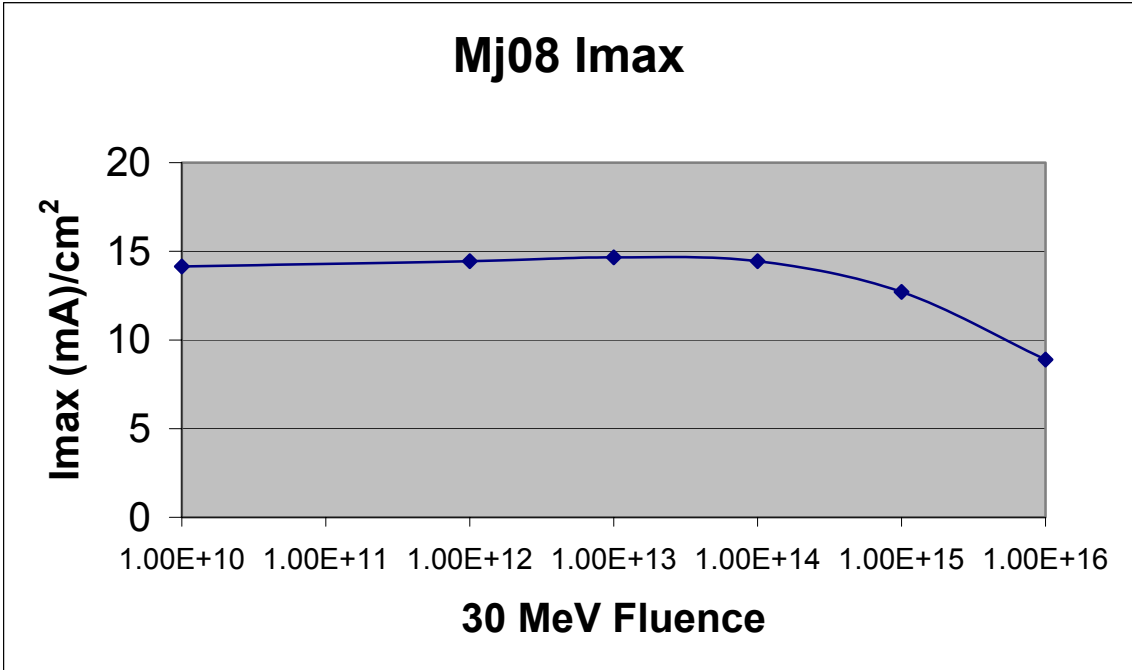


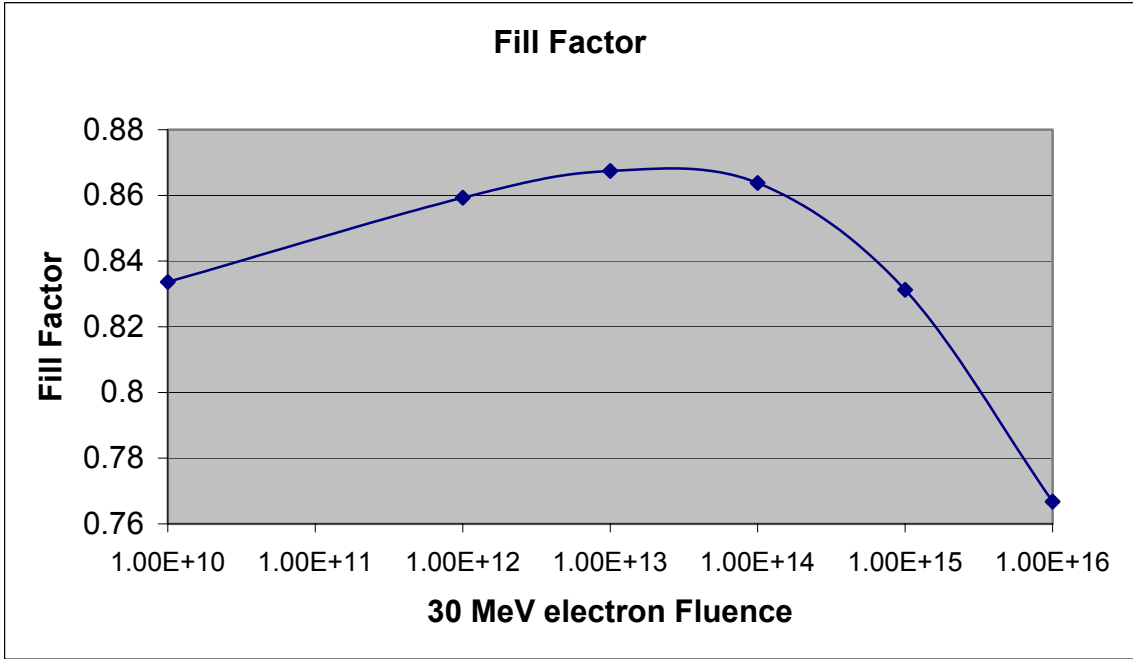


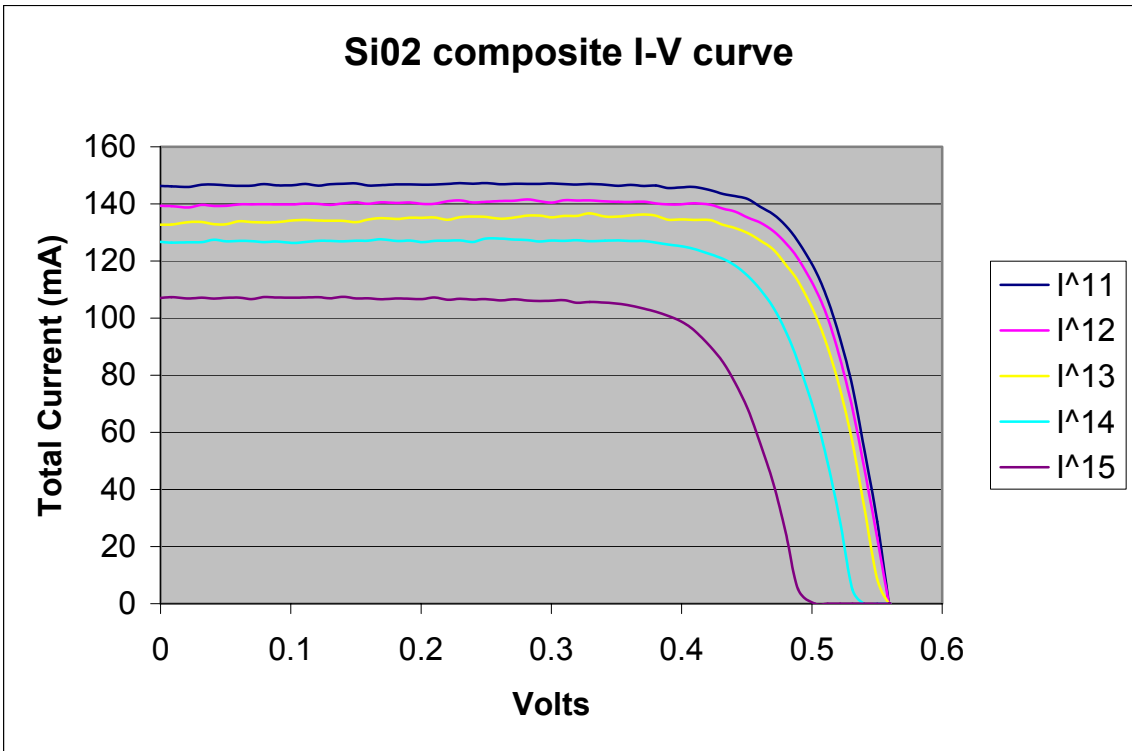
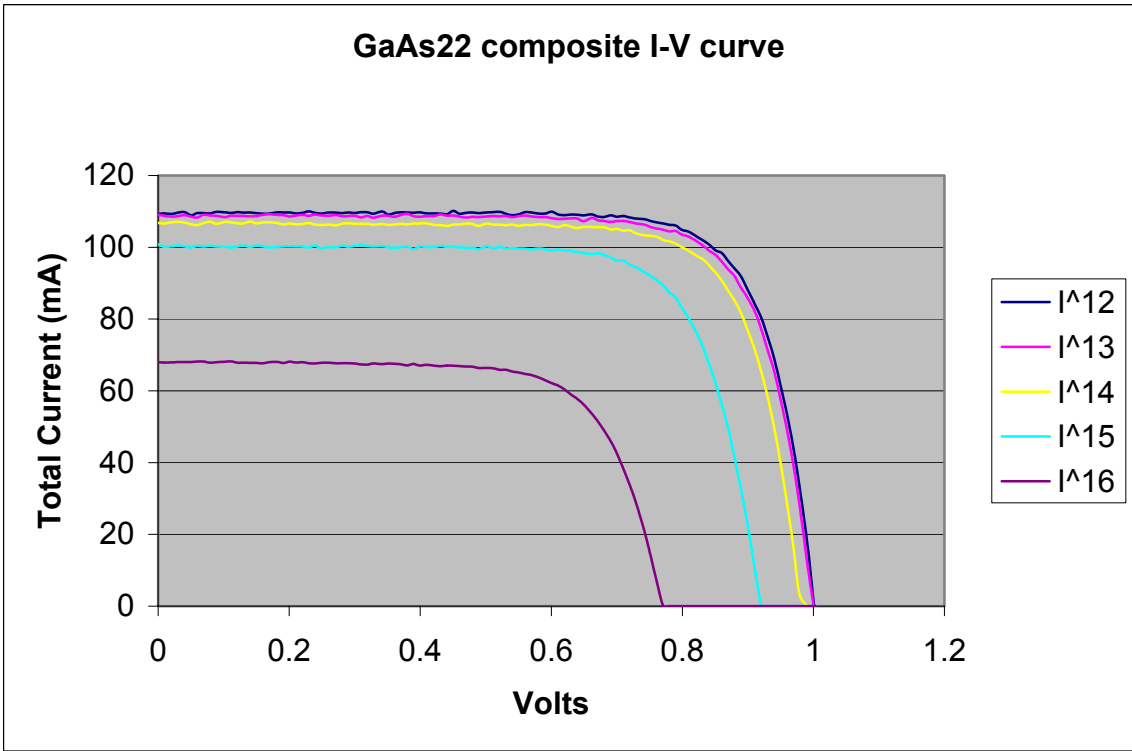


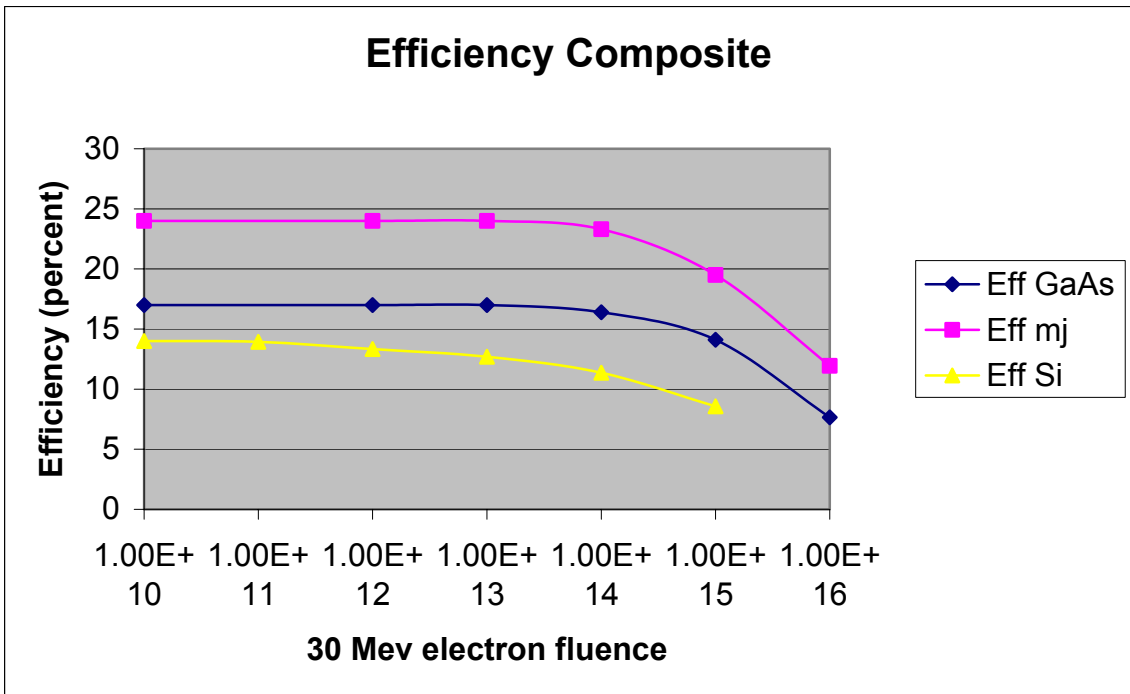
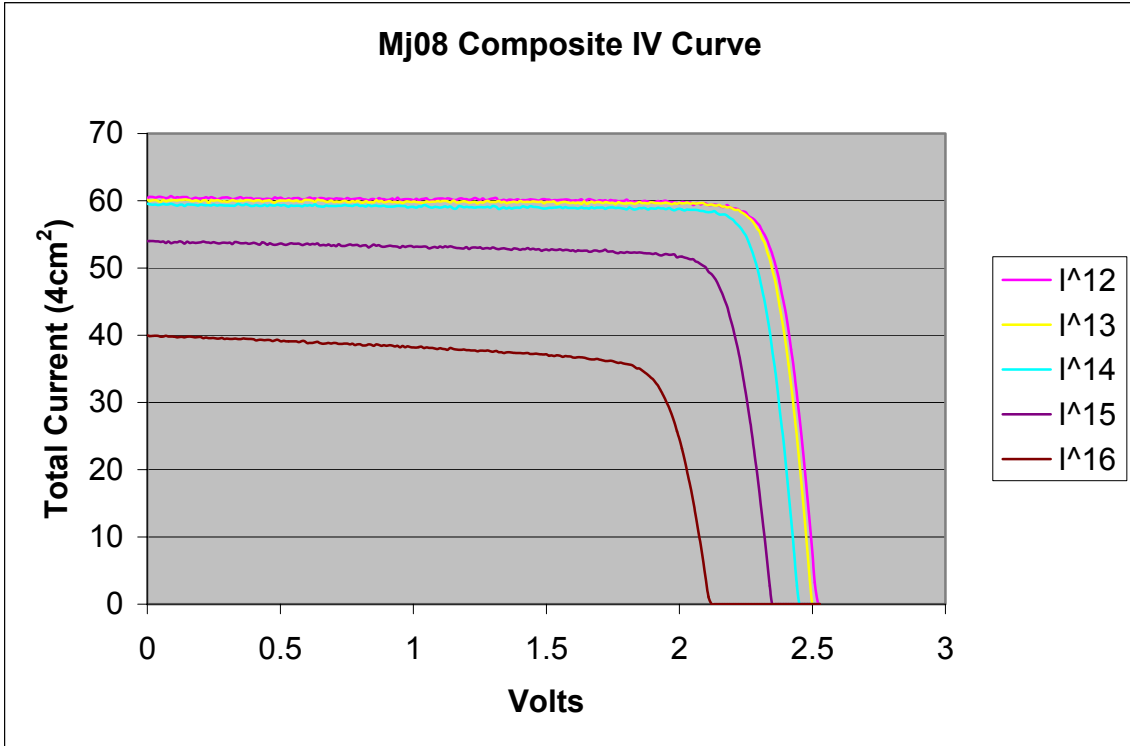


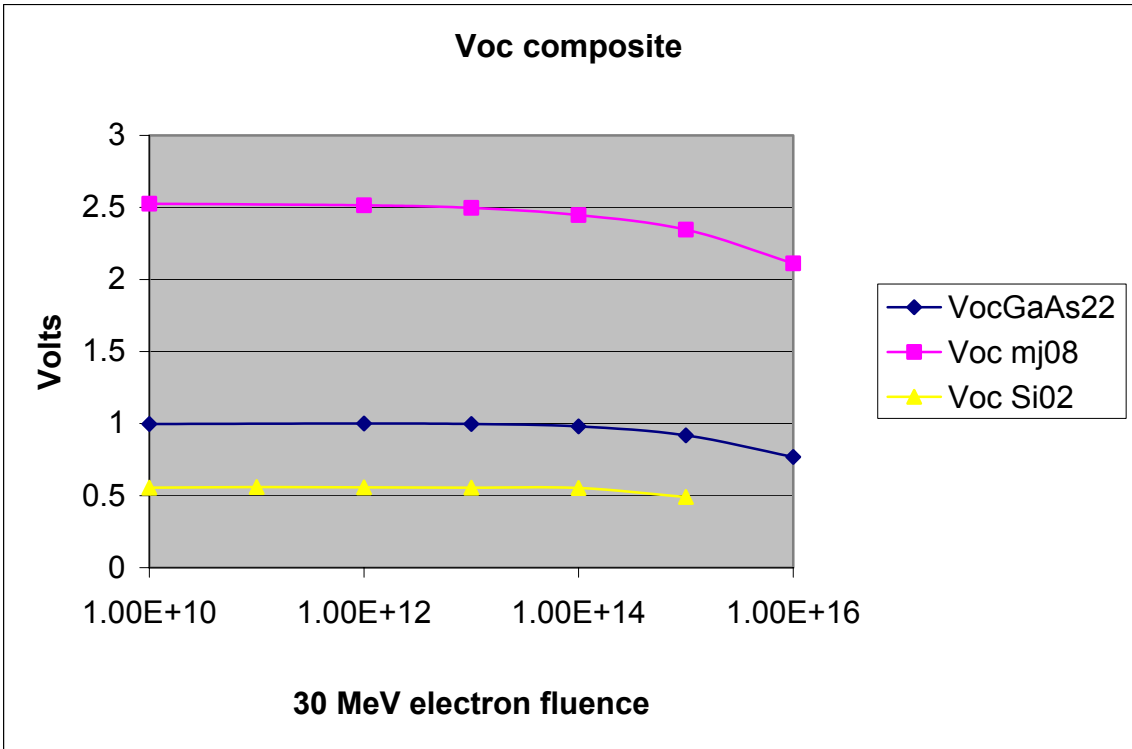
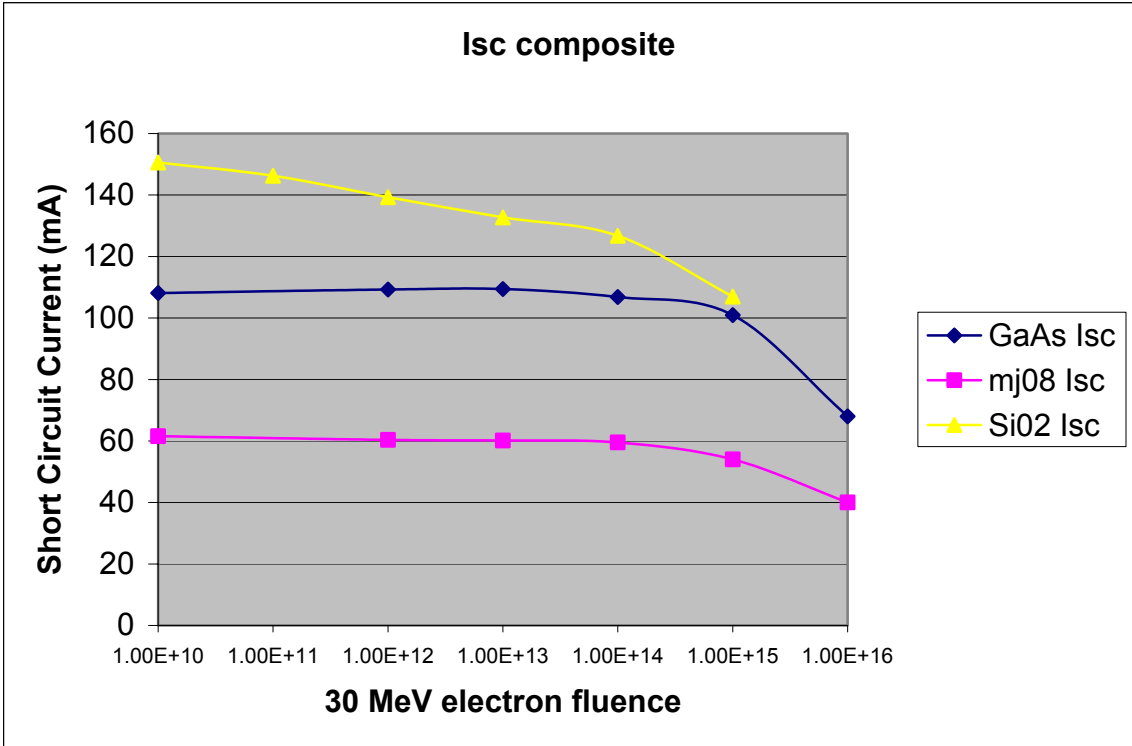


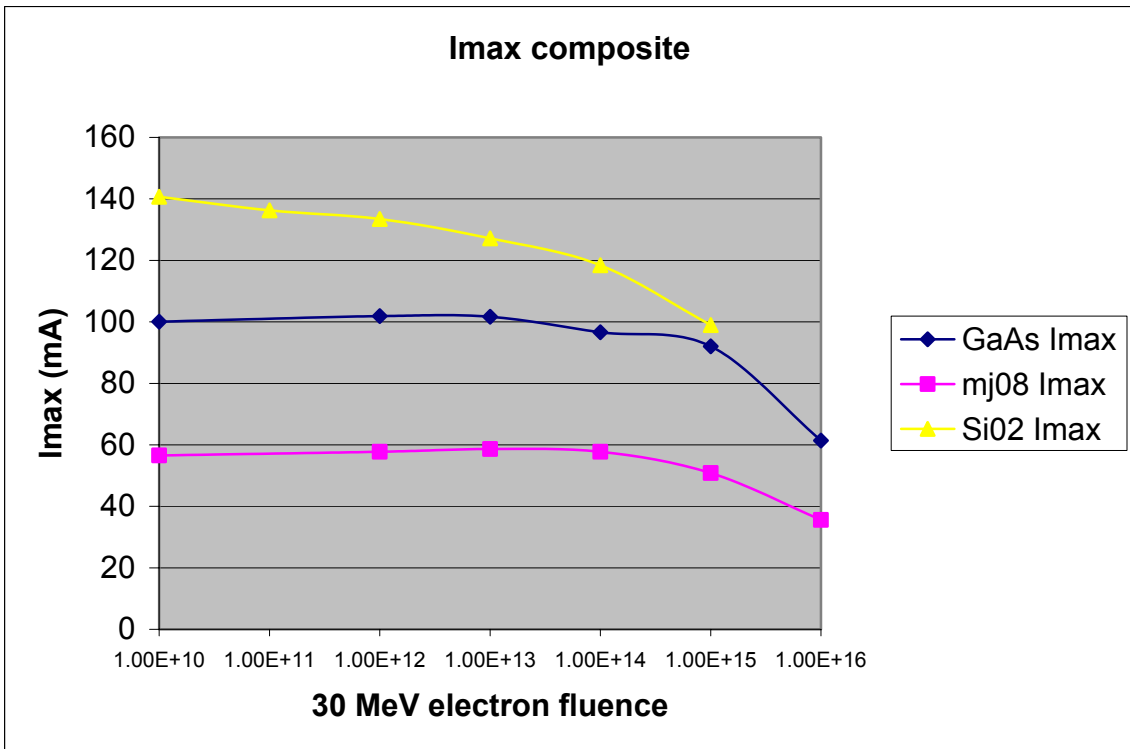
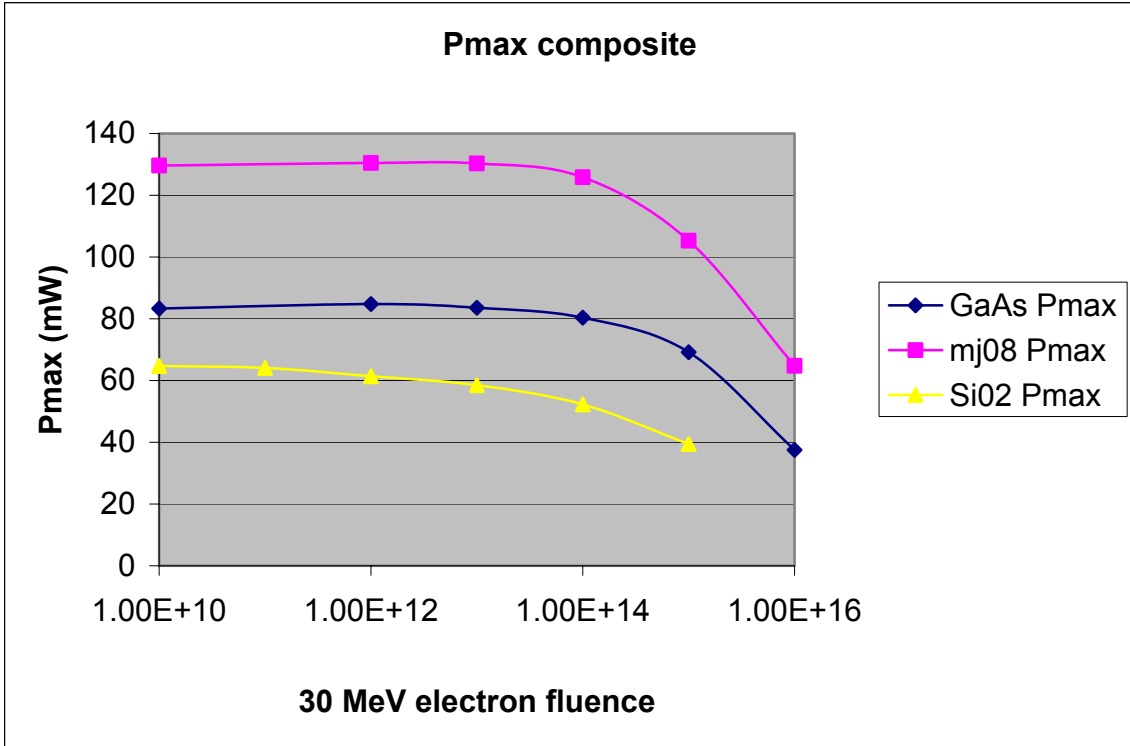


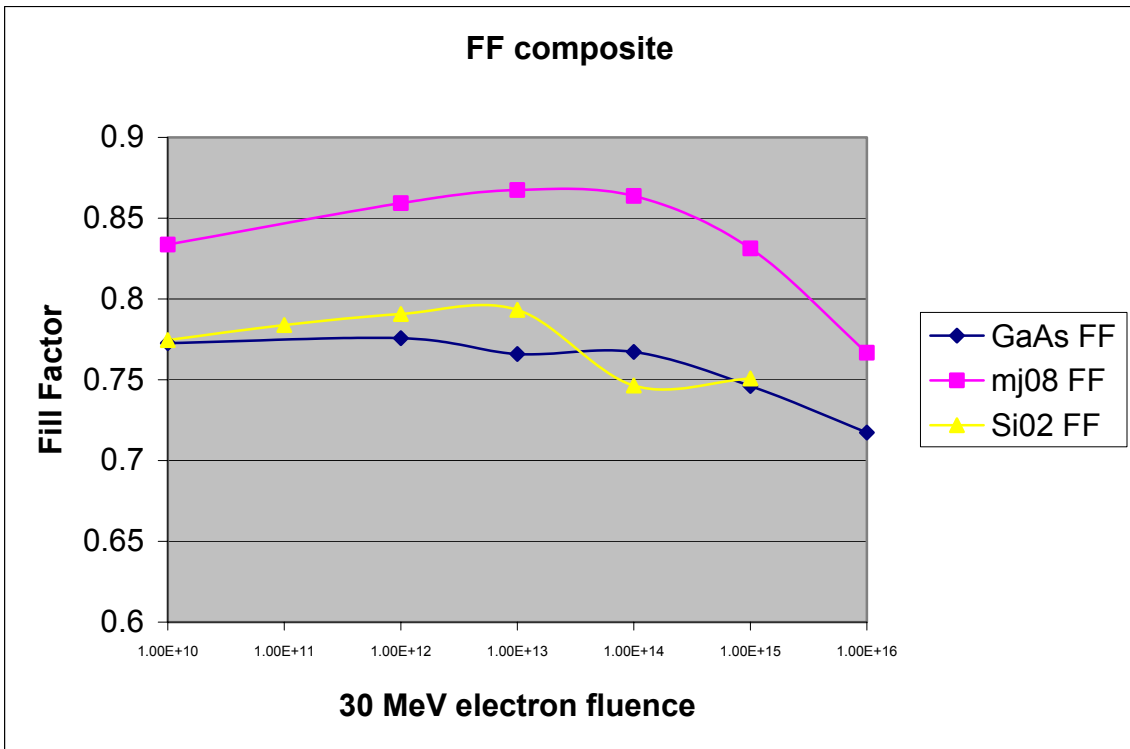
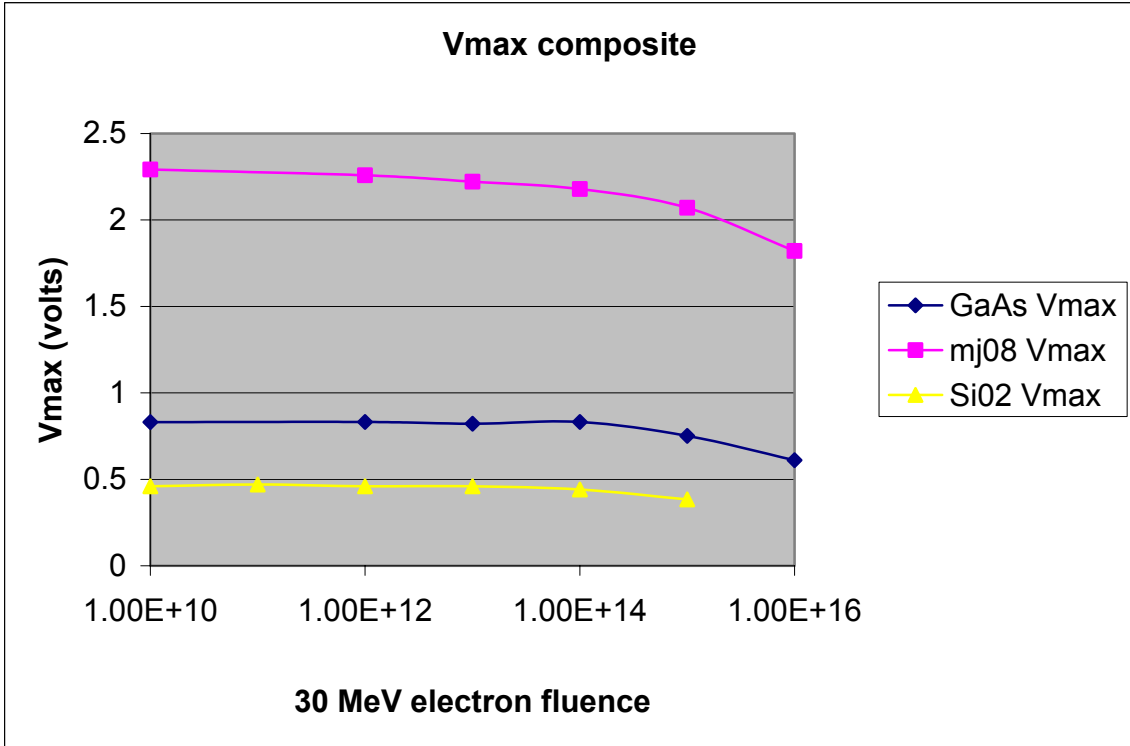




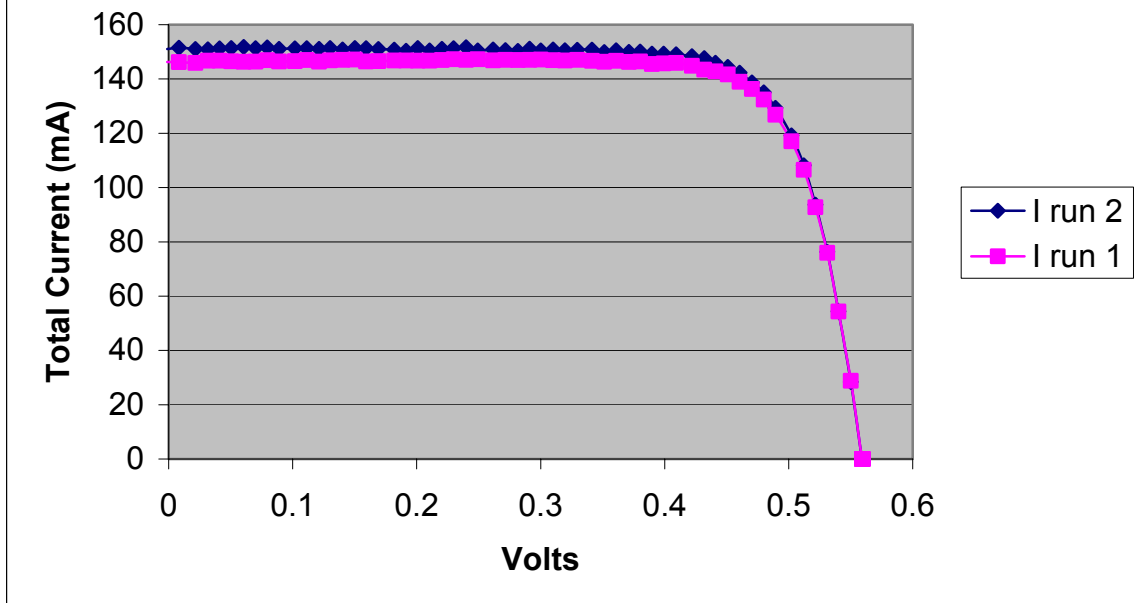




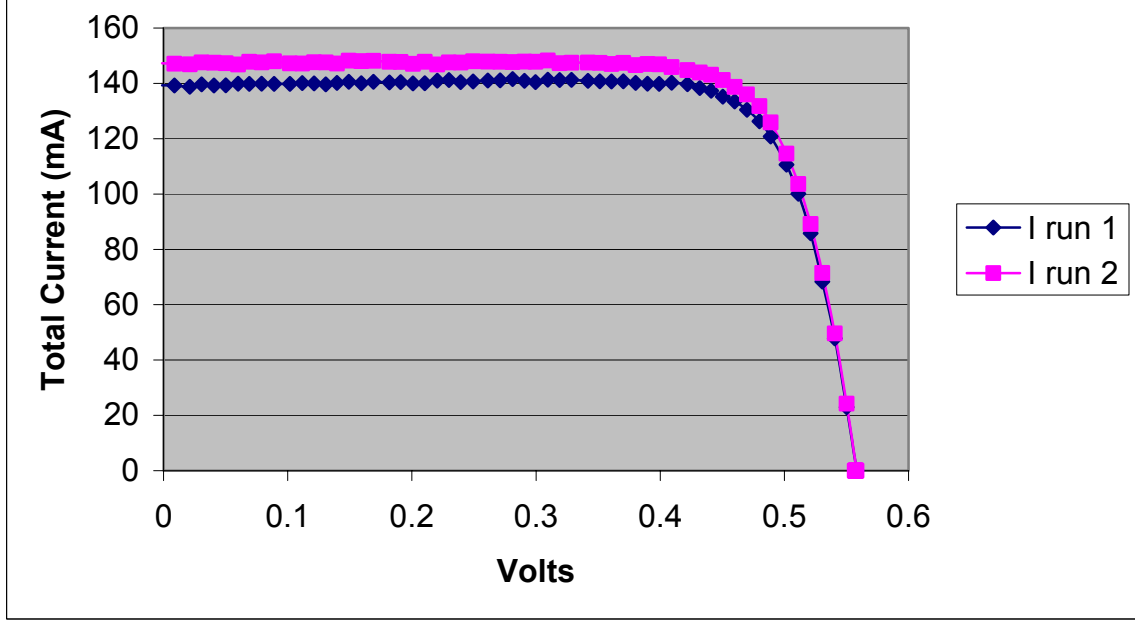


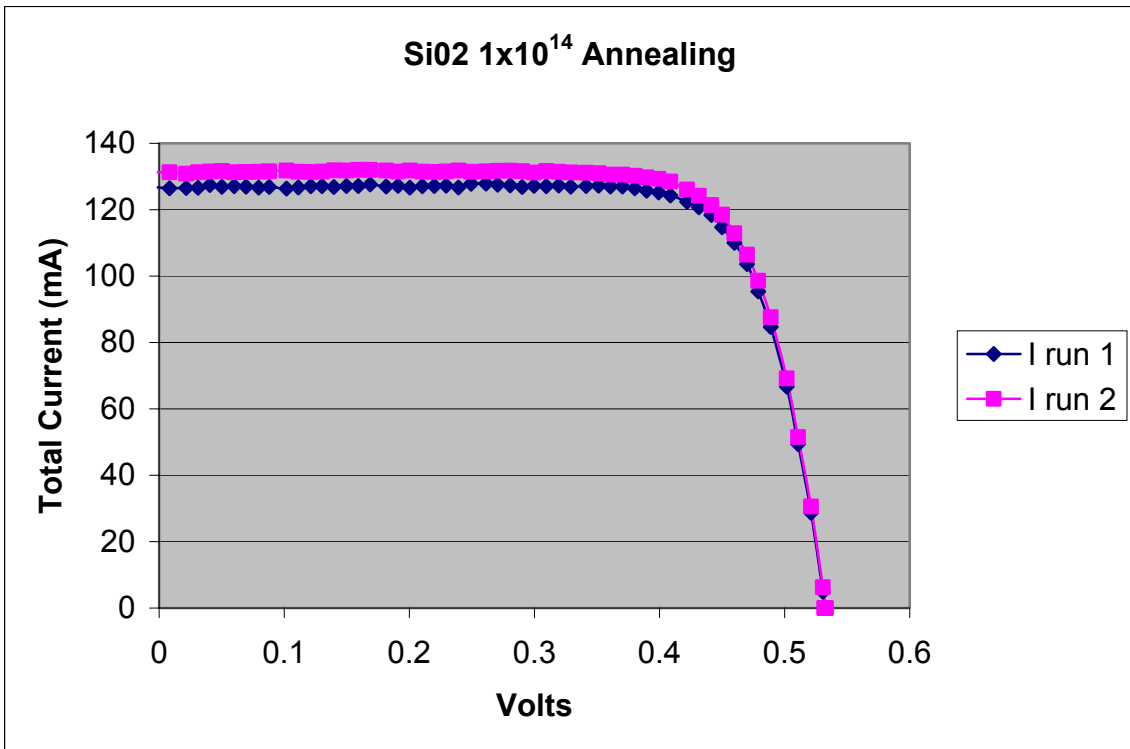
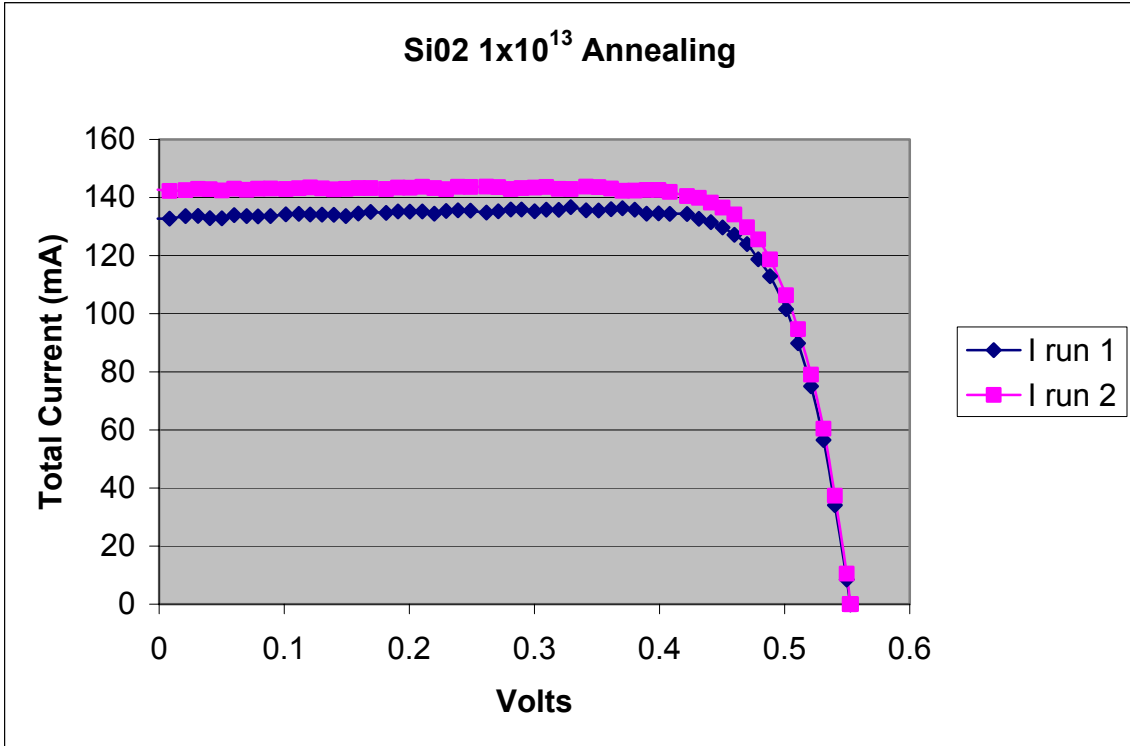


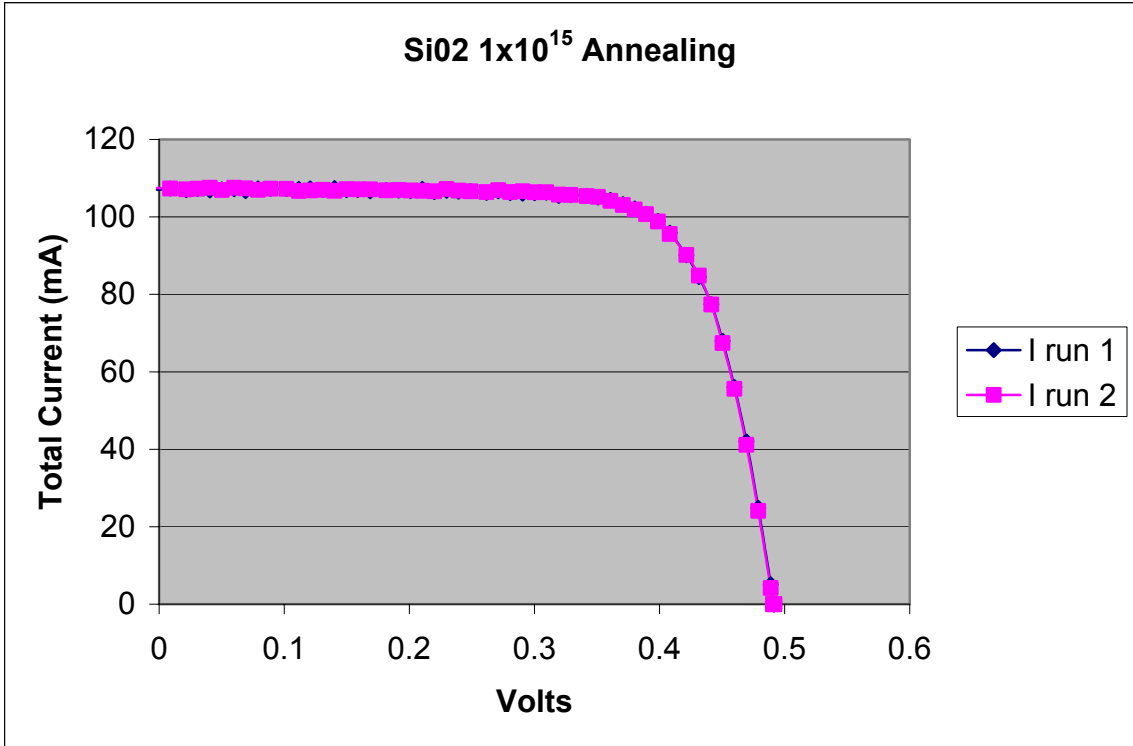
SiO₂ 1x10¹¹ annealing



SiO₂ 1x10¹² Annealing







INITIAL DISTRIBUTION LIST

1. Defense Technical Information Center
8725 John Kingman Rd. Suite 0944
Ft. Belvoir, Va, 22060-6218
2. Dudley Knox Library
Naval Postgraduate School
Monterey, Ca, 93943-5121
3. Chairman, Code 31
Space Systems Academic Group
Naval Postgraduate School
Monterey, Ca 93943-5121
4. Chairman, Code EC
Department of Electrical and Computer Engineering
Naval Postgraduate School
Monterey, Ca 93943-5121
5. Professor Sherif Michael
Department of Electrical and Computer Engineering
Naval Postgraduate School
Monterey, Ca 93943-5121